Università degli Studi di Ferrara

DOTTORATO DI RICERCA IN
"SCIENZE BIOMEDICHE E BIOTECNOLOGICHE"

CICLO XXX

COORDINATORE Prof. Paolo Pinton

Two different points of view on signal transduction: defective autophagy as a key feature of Cerebral Cavernous Malformations and c-Src as modulator of intracellular Ca^{2+} homeostasis

Settore Scientifico Disciplinare MED/04

Dottoranda   **Tutore**

Dott.ssa Mariangela Corricelli   *Prof. Paolo Pinton*

Anni 2015/2017

Table of Contents

Aims

In this thesis I present the projects I worked on during my PhD in "Biomedical and Biotechnological Science" attended in the Signal Transduction Lab of Prof. Paolo Pinton. My PhD was focused on the study of two different aspects of the signal transduction controlling the cell homeostasis in two independent physio/pathological contexts.

The aim of the first project was to study the role of autophagy in the pathogenesis of the Cerebral Cavernous Malformation (CCM). CCM is a genetic cerebrovascular disease characterized by abnormally enlarged and leaky capillaries, which can lead to severe clinical symptoms, including unpredictable and fatal intracerebral hemorrhages. CCM disease shares various molecular features with tumors, and human cancer has been associated to a dysregulation of the autophagic process, which is responsible of the quality control within the cell. Despite the significant advances in the understanding of CCM disease pathogenesis over the last decade, no direct therapies exist so far. We planned to investigate the relationship between the impaired autophagic process and the typical phenotypic signatures of CCM disorder, with the purpose to identify new targets for the development of new therapeutic strategy for treating CCM disease and improve the long-term prognosis of CCM patients. In addition, in another paper (Attachment A), we point out autophagy as a pivotal player in the pathogenesis of Cerebral Cavernous Malformation and discuss the new perspectives for disease prevention and treatment.

The second project was focused on the investigation of a potential role for the proto-oncogene c-Src in the modulation of intracellular Ca^{2+} signalling. c-Src is a non-receptor tyrosine kinase involved in the regulation of critical cellular events, as cell proliferation, cell death, migration, and invasion. c-Src deregulation plays a causative role in the pathogenesis of several human diseases, including cancer. The typical hallmarks of carcinogenesis and tumour progression, such as uncontrolled proliferation and evasion of cell death, are driven by an intense and precise modulation of intracellular Ca^{2+} signals. Based on the multiple functions shared by c-Src and Ca^{2+} signalling, the aim of this work was to understand if c-Src controls the Ca^{2+} dynamics in the various intracellular compartments and to identify the molecular mechanism that underlies this event. A detailed comprehension of c-Src functions in both physiological events and in pathological conditions might provide new options for c-Src activity modulation at multiple levels and further possible targets for the inhibition of the pathological c-Src outcomes.

(1) Defective autophagy is a key feature of Cerebral Cavernous Malformations

Introduction

1. Cerebral Cavernous Malformations

Cerebral cavernous malformations (CCMs; OMIM 116860), which are also known as cavernous angiomas or cavernomas (Fig. 1), are major vascular malformations consisting of densely packed, abnormally dilated, and leaky capillary-like sinusoids (caverns). These mulberry-shaped lesions, which can be single or multiple (up to hundreds), are mostly located in brain and spinal tissues and, more rarely, in other regions as skin and retina. The diameter of cavernous angiomas ranges from a few millimeters to several centimeters. These capillary channels are lined by a single layer of endothelium incorporated in a dense collagen matrix and lack of constitutive vessel structural components, which are essential for the normal vascular function and integrity, as smooth muscle, basal lamina of the endothelial cells, pericytes, astrocytic foot processes and tight junctions at endothelial cell interfaces [1]; [2]; [3]; [4]. Therefore, these aberrant vascular sinusoids result extremely fragile and frequently lead to unpredictable hemorrhages.

Cerebral cavernous malformation lesions are estimated to occur in 0.3-0.5% of the general population, if gender and age distinctions are not considered [4]. Generally, only approximately 20-30% of people with CCM lesions will eventually develop clinical symptoms, and the variability of the clinical symptoms is mainly depending on the size, location, and bleeding propension of the cavernomas. The clinical symptoms range from recurrent headaches, visual and auditive defects, severe neurological deficits, convulsions and epileptic seizures, strokes, and intracerebral hemorrhages (ICH) [2]; [3]. The epileptic events may lead to loss of consciousness and dramatic generalized crises. Neurological deficits can elicit limb weakness, visual and balance disturbances, attention and memories problems. Nevertheless, frequently the lesions remain completely asymptomatic during most of the host's lifetime, otherwise they remain clinically and biologically quiescent except rare angiogenic activity and hemorrhage. Although the clinical symptoms arise most frequently during the second to fourth decade of life, the angiomas can arise throughout the all life and are found also in children.

Cerebral cavernous malformation is a genetic disease arising sporadically or being inherited as autosomal dominant condition (familial form) [5] with incomplete penetrance and highly variable expressivity, even among members of the same family, suggesting that multiple factors can contribute to CCM disease pathogenesis. Indeed, it is thought that the heritable CCM requires a second-hit mutation [6], or specific additional factors

within the neurovascular environment. Notably, the hereditary form is often associated with multiple cavernous angiomas, with the lesions size and number increasing as the patient ages, whereas the sporadic form, which accounts for approximately 80% of CCM, typically presents as a solitary lesion [5].

The diagnosis mainly occurs as the lesions become symptomatic. Although the initial description of the disease occurred in 1930, a reliable diagnosis was impossible until the advent of magnetic resonance imaging (MRI) in 1980, because the cavernous angiomas, in which the blood flows very slowly, are not visible through angiography, but it is necessary a TAC (computerized axial tomography). Gradient echo MR sequences may reveal a larger number of smaller occult lesions. Furthermore, in familial CCM specific genetics screens represent an additional diagnosis method.
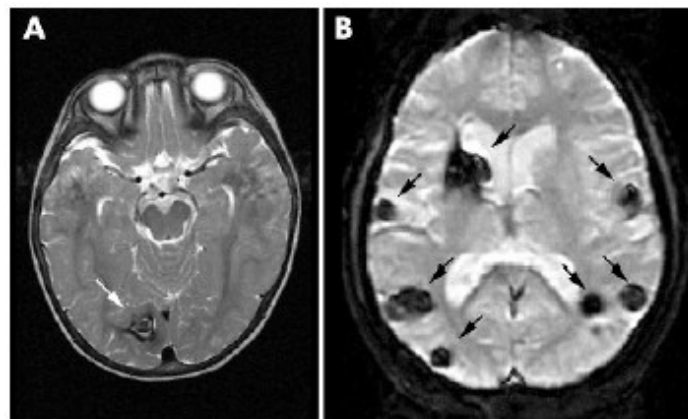
Figure 1 | (A) Axial T2 weighted magnetic resonance imaging sequence; solitary lesion (white arrow) in the right occipital lobe in a 3 year old boy. (B) Axial T2 weighted gradient echo sequence; multiple supratentorial cerebral cavernous malformations (black arrows) in a young adult. From "Cerebral cavernous malformation: new molecular and clinical insights" Revencu and Vikkula, Journal of Medical Genetics; 43(9): 716–721 (2006).

Despite the significant progress and breakthroughs in the understanding of CCM disease pathogenesis over the last decade, with the potential for great advancing in the development of both prevention and treatment strategies, no direct therapeutic approaches exist so far. Treatments with anti-epileptic drugs are only available for patients with seizures, besides the surgical removal of accessible lesions in patients with recurrent hemorrhage or intractable seizures. However, despite the modern technology allows to reduce the damage of the surrounding healthy tissue, the surgical approach is invasive and presents substantial risks, including paralysis, stroke, coma and death. Thus, novel pharmacological strategies are required for preventing the de novo formation of CCM lesions in susceptible individuals and the most severe disease phenotype, including the development of numerous and large symptomatic lesions and ICH.

1.1 CCM proteins

Genetic studies identified three genes whose loss-of-function mutations cause CCM: CCM1/KRIT1 (Krev interaction trapped protein 1), CCM2/MGC4607/OSM/Malcavernin, and CCM3/PDCD10/TFAR15, which account for approximately 50%, 20%, and 10% of CCM cases, respectively. The remaining 20% of cases have been attributed to mutations in a fourth unidentified CCM gene [5]. Genetic analysis of familial CCM patients revealed that CCM1 is located at 7q21-22, CCM2 at 7p13-15, and CCM3 at 3q25.2-27 [7]; [8].

CCM1 encodes for KRIT1, a 84 kDa molecular weight protein. Without a specific catalytic activity, KRIT1 contains several protein-protein interaction domains, suggesting a role as a versatile scaffold for the assembly of multiprotein complexes involved in different signaling pathways. *KRIT1* gene was identified in 1997 and cloned through yeast two-hybrid screen by using Krev1/Rap1, which encodes for a small Ras-family GTPase [7].

Within the N-terminal region there are three NPXY/F motifs that are involved in protein-protein interactions and probably in the regulation of intra-molecular conformational changes. At the C-terminus resides a FERM (band Four.1 Ezrin Radixin Moesin) domain containing three different subdomains F1-F3 that are arranged in clover-shaped fashion. FERM is a modular domain generally involved in the intermolecular interactions, is usually found in membrane binding proteins and mediates the protein localization at the plasma membrane, allowing the interaction with other proteins and phosphoinositides. A phospho-Tyrosine binding (PTB) domain is located within the F3 subdomain and mediates the interaction with canonical NPXY/F motifs, typically found within the cytoplasmic tail of transmembrane receptors. Therefore, it may interact with the third NPXY/F motif within KRIT1 N-terminus. KRIT1, owing to either intramolecular folding or dimerization, can assume both an open and a closed conformation, and the binding with interactors, which prevents its conformational rearrangement, can direct its subcellular localization. Between the NPXY/F motifs and the FERM domain there are four ankyrin repeats, which commonly mediate protein-protein interactions. At the N-terminal region preceding the first NPXY/F motif sit a nuclear localization sequence, a putative nuclear export sequence, and a tubulin binding sequence. This region has been identified as a nucleotide diphosphate linked to an X moiety (Nudix) domain [9], whose specific function has not been yet established.

It has been identified a further KRIT1 isoform lacking the 15th coding exon, KRIT1B, which has a highly restricted expression in humans. KRIT1B is devoid of a functional PTB binding pocket, indispensible for the binding with Rap1, displays a restricted cytoplasmic localization, and cannot adopt the closed conformation [10].

CCM2 or OSM (osmosensing scaffold for MEKK3) is a 51 kDa scaffold protein that has been identified through a yeast two-hybrid screen using MEKK3 as bait upon hyperosmotic shock [11]; [12]. Similarly to KRIT1, CCM2 contains a phosphotyrosine-

binding domain (PTB) at its N-terminus, which binds with both the second and third NPXY/F motifs of KRIT1 [13]. Recently, it has been discovered a harmonin-homology domain (HHD) within the C-terminus, a folded region displaying structural homology with a domain found in the harmonin protein, where it functions as a scaffold for protein interactions [14].

CCM3 or PDCD10 (Programmed Cell Death 10) has been identified later [15], as a 25 kDa protein containing a dimerization domain at N-terminus and focal adhesion targeting (FAT)-homology domain at C-terminus. Through its FAT-homology domain CCM3 can associate with CCM2.

Consistently with their involvement in the pathogenesis of the same disease, KRIT1, CCM2 and CCM3 interact between each other and form *in vivo* a ternary complex. In particular, the interaction between KRIT1 and CCM2 involves the PTB domain and the N-terminus of CCM2 and the counterpart on KRIT1 are the second and third NPXY/F motifs [13]. CCM2 interacts also with CCM3, but the CCM2 site interacting with the CCM3 FAT-homology domain has not yet been clearly identified. It has been suggested that the two CCM2 binding sites are not redundant and that CCM2 acts as a linker that brings together KRIT1 and CCM3, which otherwise have no affinity for each other.

1.2 KRIT1 functions

The physiological role of KRIT1 and how its mutation causes the cavernous malformations is not yet completely understood, although the histology of the angiomas strongly suggests that KRIT1 may exert a critical role in normal vascular development or in maintenance of vascular integrity. KRIT1 expression in the endothelium is not high nor specific, since it is extensively expressed also in other tissues. Thus, an intriguing explanation about the etiology of the cavernous malformations, which affect exclusively the endothelium, might be related to the specific functions and interactions occurring in endothelial cells. CCM proteins bind with numerous other proteins (Fig. 2). Therefore, the association of the three CCM proteins in a ternary complex and their localization within the cell are regulated by the interaction with other complexes displaying different intracellular localizations. Furthermore, since each CCM protein directly operates in multiple signalling networks, KRIT1 function is necessarily influenced by the CCM2 and CCM3 pathways.

KRIT1 has been observed to colocalize with microtubules and two microtubule-binding sites have been identified [16]. Since their interaction with α- and β-tubulins, it has been suggested that CCM proteins move within the cell through microtubules. Besides the association with microtubles, KRIT1 translocates to the plasma membrane mostly because of the Rap1 or heart-of-glass 1 (HEG1) binding, whereas the binding with integrin cytoplasmic-associated protein 1 (ICAP-1) promotes KRIT1 relocalization to the nucleus. Similarly, CCM2 and CCM3 anchor to the plasma membrane by interacting with

membrane-located proteins, as GTPases and paxillin. CCM proteins can also directly bind to membrane phosphoinositides, KRIT1 and CCM2 via their FERM and PTB domain, respectively, whereas the CCM3 lipid binding region has not yet been identified.
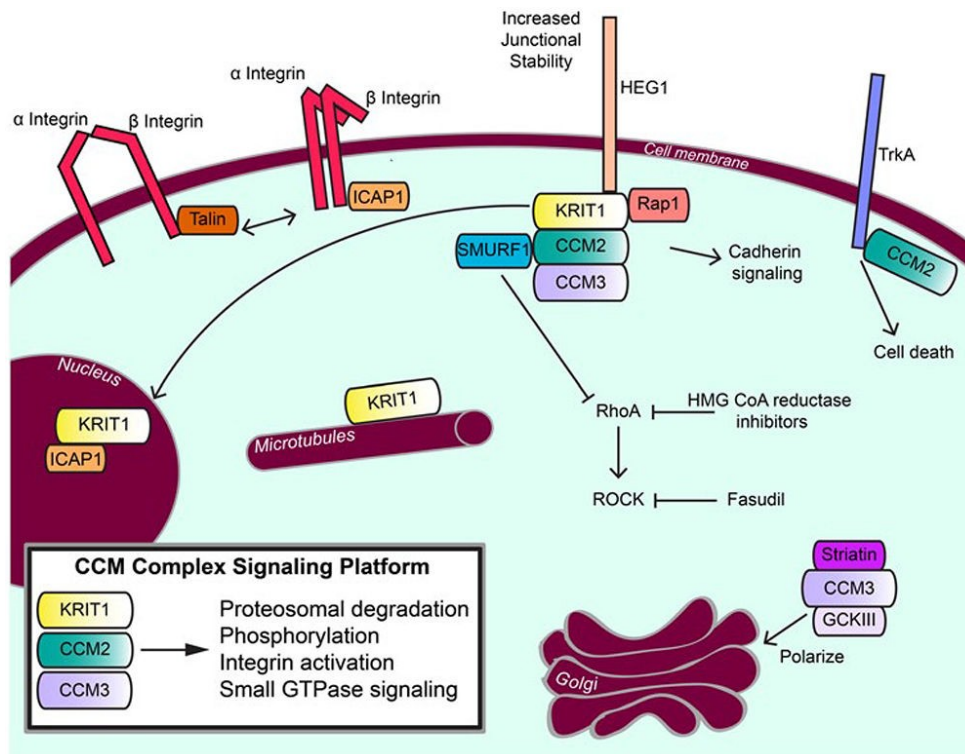
Figure 2 | CCM proteins in signal transduction. Signal transduction from the CCM complex signaling platform is shown and the roles of CCM proteins outside of the CCM complex signaling platform are also indicated. The CCM proteins play roles in cell adhesion complexes and integrin signaling, in kinase signaling cascades, and in degradation/regulation of the Rho family of small GTPases. From "Signaling pathways and the cerebral cavernous malformations proteins: lessons from structural biology" Fisher et al., Cellular and Molecular Life Sciences; 71(10):1881-92 (2014).

Consistently with the CCM phenotype, increasing evidences indicate that at the plasma membrane KRIT1, as the other CCM proteins, is involved in the control of cell-cell adhesion, cell adhesion to extracellular matrix, cell shape and polarity, and correct lumen formation.

Rap1, a Ras-related small GTPase, was the first identified KRIT1 interacting protein [7]. Rap1 is involved in the regulation of cell-cell adhesion by acting on adherens junctions, in integrin-mediated cell adhesion to extracellular matrix, and in cell polarity. In particular, KRIT1 and Rap1 form a complex in which KRIT1 acts as Rap1 effector in the regulation of endothelial cell junctions [17]. Indeed, at cell-cell junctions KRIT1 interacts with other partners, including β-catenin and VE-cadherin, thus contributing to the stabilization of the junctions.

KRIT1 forms a complex with ICAP-1, the β1 integrin suppressor. ICAP-1 downregulates the cell adhesion to extracellular matrix by disrupting the β1 integrin focal adhesions, thus

enhancing the cell migration. KRIT1 competes with β1 integrin for the binding with ICAP-1 and, by sequestering ICAP-1, induces the integrin activation [18]. Interestingly, integrins are involved in the organization of the actin cytoskeleton, in the remodeling of extracellular matrix, regulate cell proliferation and vascular morphogenesis. Additionally, KRIT1 sequesters ICAP-1 at nucleus, thus affecting the proliferation pathway stimulated by ICAP-1 [19]. Otherwise, CCM2 interaction with KRIT1 leads to the sequestration of the KRIT1/ICAP-1 complex in the cytosol and prevents its nuclear translocation.

KRIT1, CCM2 and the endothelial cell adhesion receptor HEG1, the mammalian homolog of the zebrafish heart of glass, are part of a ternary complex, which has been suggested to be a critical regulator of vessel and heart formation and integrity [20].

Moreover, KRIT1 and CCM3 control vascular development, prevent endothelial proliferation and sprouting angiogenesis by activating DELTA-NOTCH cascade [21].

However, CCM2 and CCM3 control angiogenesis and vascular integrity also by acting in separate pathways. CCM3 modulates the cardiovascular development via its association with the germinal center kinases III (GCKIII) STK24, STK25 (Serine/threonine Kinase 24, 25) and MST4 (Mammalian sterile twenty-like 4). CCM3 binding with GCKIII kinases leads to an enhanced cell migration and proliferation [22]. Additionally, CCM3 is also a component of the STRIPAK (striatin-interacting phosphatase and kinase) complex, implicated in the regulation of Golgi polarization [23]. CCM3 further contributes to stabilize the endothelial cell junctions and the vascular lumen formation by suppressing the exocytosis of angiopoietin 2 (ANGPT2) mediated by UNC13B and vesicle-associated membrane protein 3 (VAMP3) [24]. Instead CCM2, by acting as a scaffold between RAC1 and MEKK3 (mitogen-activated protein kinase kinase kinase 3) in the p38 MAPK signalling [12], is involved in the regulation of actin remodeling and angiogenesis. CCM2 regulates physiological vascular integrity, cell-cell interactions, and cytoskeleton architecture also through the downregulation of RhoA activation via proteosomal degradation mediated by Smurf1 [25]. Moreover, at plasma membrane CCM2 acts as key mediator of death signalling by interacting with TrkA receptor tyrosine kinase [26].

In endothelium KRIT1 negatively modulates the bone morphogenetic protein (BMP) and the transforming growth factor-β (TGF-β) signalling, thus preventing the endothelial-to-mesenchymal transition (EndMT) and the CCM lesions onset [27].

Among the additional stress factors occurring locally at the blood-brain microenvironment and contributing to CCM pathogenesis, a crucial role may be exerted by the redox state. Indeed, it has been demonstrated that KRIT1 contributes to the prevention of the oxidative stress-related vascular dysfunctions by limiting the accumulation of intracellular oxidants through the enhancement of a ROS scavenging pathway involving FoxO1 and SOD2 [28]. In addition, KRIT1 exerts a protective role against oxidative stress by limiting the pro-oxidant JNK/c-Jun-dependent pathways [29].

2. Autophagy

Within the cells, the homeostasis is preserved by a fine equilibrium between macromolecules and organelles biosynthesis and turnover. In eukaryotic cells two different mechanisms are responsible for cellular components degradation, the ubiquitin proteasome system (UPS) and the autophagy. While the UPS mediates only protein degradation, predominantly short-lived proteins, which are previously tagged by ubiquitin for the recognition by the proteasome, autophagy is responsible for the degradation of cytosolic components and macromolecules, including long-lived proteins, and mediates the organelles turnover through a lysosomal pathway [30].

Autophagy is an evolutionarily conserved catabolic process that involves a subcellular membranes rearrangement with the purpose to sequester cytosol and organelles and to expose them to the lysosomal degradation [31]; [32]. Thus, autophagy ensures the intracellular components recycling, in order to compensate nutrients and energy starvation, but also controls the organelles quality and number via their selective elimination [33]. Autophagy is further involved in the remodeling during the physiological development and differentiation, in a caspase-independent programmed cell death (type II or autophagic cell death), and in the control of cell and tumoral growth [34]. It has also been proposed as mechanism for protecting against aging, since it participates in the elimination of organelles damaged by age-dependent peroxidation of several molecules.

There are three different classes of autophagy (Fig. 3): microautophagy, chaperone-mediated autophagy (CMA), and macroautophagy [33], which differ based on the inducing stimuli, mechanism of sequestration, and the nature of the cargo. Macroautophagy and microautophagy are evolutionary conserved ranging from yeasts to mammals, whereas CMA is specific for mammals.

During microautophagy, lysosome membrane invaginations directly incorporate cytoplasmic portions, which are subsequently degraded within the lysosomal lumen.

By contrast, CMA requires the cytosolic heat-shock cognate protein Hsc70 and its co-chaperone that, after the selective recognition of unfolded proteins containing the motif KFERQ, lead to their lysosomal delivery and binding with the lysosomal membrane protein LAMP-2A, and the following translocation through the lysosome membrane for the degradation [35]. CMA acts in both wide-ranging processes, including oxidized and misfolded proteins removal, thus providing amino acids during long starvation periods, and more specific events, as neuronal survival, kidney growth, and antigen presentation by major histocompatibility complex (MHC) class II molecules.
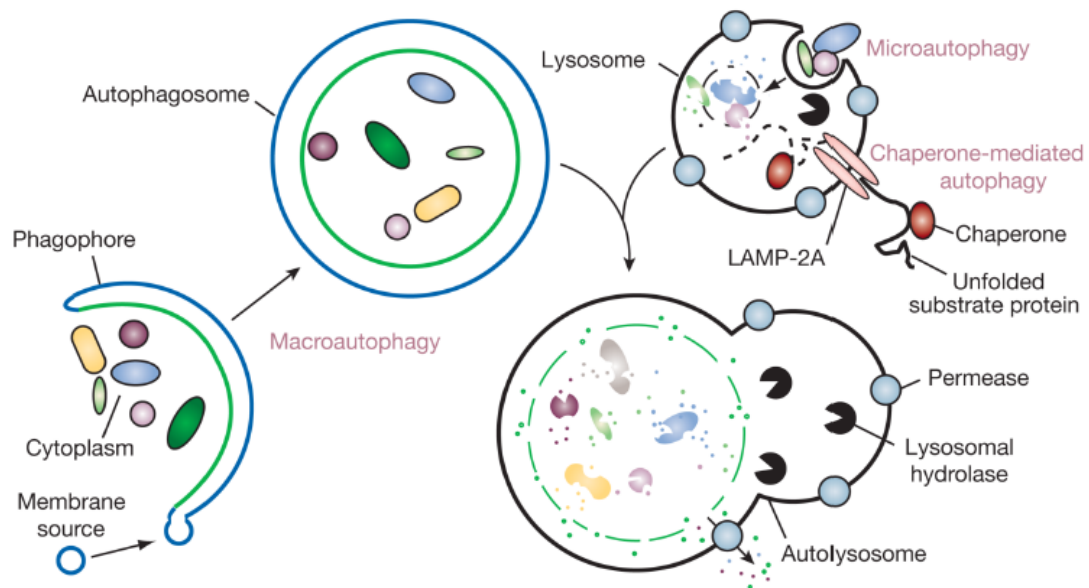
Figure 3 | Different types of autophagy. Microautophagy refers to the sequestration of cytosolic components directly by lysosomes through invaginations in their limiting membrane. The function of this process in higher eukaryotes is not known, whereas microautophagy-like processes in fungi are involved in selective organelle degradation. In the case of macroautophagy, the cargoes are sequestered within a unique double-membrane cytosolic vesicle, an autophagosome. Sequestration can be either nonspecific, involving the engulfment of bulk cytoplasm, or selective, targeting specific cargoes such as organelles or invasive microbes. The autophagosome is formed by expansion of the phagophore, but the origin of the membrane is unknown. Fusion of the autophagosome with an endosome (not shown) or a lysosome provides hydrolases. Lysis of the autophagosome inner membrane and breakdown of the contents occurs in the autolysosome, and the resulting macromolecules are released back into the cytosol through membrane permeases. CMA involves direct translocation of unfolded substrate proteins across the lysosome membrane through the action of a cytosolic and lysosomal chaperone hsc70, and the integral membrane receptor LAMP-2A (lysosome-associated membrane protein type 2A). From "Autophagy fights disease through cellular self-digestion" Mizushima et al., Nature; 451(7182):1069-75 (2008).

Macroautophagy (hereafter referred as autophagy) is the main type of autophagy. It requires the transient formation of a vacuole, known as autophagosome, for the cytoplasmic components sequestration [31]; [32]. As physiological event, a basal autophagy provides the constitutive turnover of cytoplasmic components, thus performing an homeostatic function. It is a selective process that occurs upon nutrients abundance and mediates the removal of damaged organelles and harmful protein aggregates that are unnecessary or dysfunctional, which could become toxic for the cell [33]. Autophagy is directed specifically to protein aggregates and organelles, including mitochondria and endoplasmic reticulum, explicating a crucial quality control mechanism. Cargo-specific autophagy, selective for peroxisome, ribosomes and intracellular pathogens, also exists. In physiological conditions, autophagy is involved in neurodegeneration and aging prevention, in tumor suppression, in the clearance of intracellular microbes, and in the regulation of innate and adaptive immunity. As a survival mechanism, a non-selective

autophagy functions as an adaptive response to stress conditions, as nutrient limitation, by a bulk recycling of macromolecules, including proteins, lipids and carbohydrates, for the synthesis of cellular components and energy supply.

2.1 The autophagy machinery

Autophagy can be divided in five steps (Fig. 4): formation of isolation membrane or nucleation, elongation, membrane enclosure and phagosome formation, autophagosome-lysosome fusion, and lysosomal degradation.
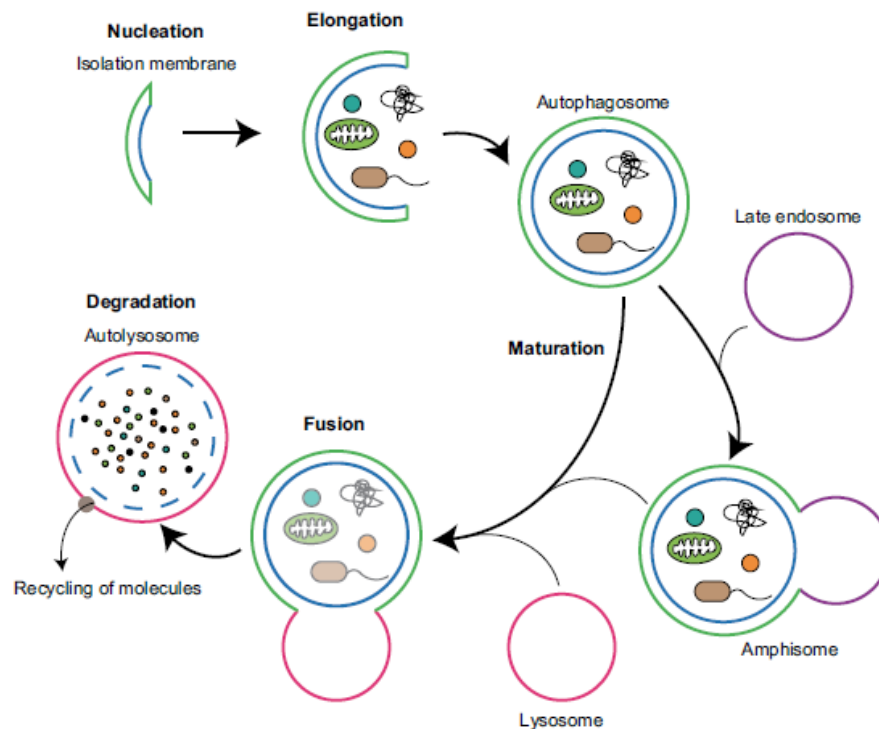
Figure 4 | Overview of autophagy. Upon induction of autophagy by stress, cytoplasmic materials are sequestered by a double-membraned structure, called autophagosome. These autophagosomes fuse with late endosomes (termed amphisomes) or lysosomes to become autolysosomes, in which the sequestered cargos are degraded and recycled for the maintenance of cellular homeostasis. Autophagy can be divided into several steps: formation of the isolation membrane (nucleation), elongation of the isolation membrane (elongation), completion and transport of the autophagosome (maturation), docking and fusion between autophagosome and lysosome (fusion), and degradation of the cargos inside the autolysosome (degradation). From "New insights into autophagosome-lysosome fusion" Nakamura et al., Journal of Cell Science; 130(7):1209-1216 (2017).

Autophagy events are mostly mediated by autophagy-related (Atg) proteins. Atg genes were initially discovered in yeast and later in multicellular organisms. Through genetic screens in Saccharomyces cerevisiae with defective autophagy almost 30 Atg proteins have been identified, and these proteins are highly conserved from yeast to mammals. However, in mammals some Atg proteins have several isoforms and paralogs.

The autophagosome biogenesis is a highly dynamic event that requires multiple protein complexes and the mobilization of membrane reserves. Upon the induction of autophagy, the nucleation process is started by the ULK1 complex, composed by ULK1 (unc-51 like autophagy activating kinase 1), the regulatory protein Atg13, FIP200, and the Atg13-binding protein Atg101. Its translocation to the pre-autophagosome represents an indispensable event for the recruitment of the other proteins at the phagophore assembly site and the formation of the mature autophagosome [36].

Beclin1-class III PI3K (phosphatidylinositol 3-kinase) complex, consisting of Beclin1, class III PI3K/Vps34, its regulatory protein kinase p150/Vps15, and Atg14, plays an essential role in the isolation membrane nucleation [37]. Vps34 is recruited to the pre-autophagosome where promotes the formation of phosphatidylinositol 3-phosphate (PI3P) [38]. To note, it has been suggested that this protein complex could recruit membranes from several intracellular structures, such as endoplasmic reticulum, Golgi apparatus and mitochondria. In addition, the Beclin1-Vps34-Vps15 complex, by interacting with UVRAG and Rubicon, controls the later events of the autophagic process: via interaction with UVRAG promotes the autophagosome maturation and the endocytic trafficking, while the Rubicon-UVRAG-Vps34-Vps15-Beclin1 complex downregulates these events.

Atg9-WIPI-1 complex, composed of Atg9, the PI3P binding protein WIPI-1, and likely Atg2, is then recruited to the autophagic membranes via PI3P. Indeed, both Atg9, which resides at trans-Golgi and endosomes, and WIPI-1, during starvation were found to localize to the autophagosomes. Although it has been established that Atg9 translocation occurs in ULK1-dependent manner, the WIPI-1 association mechanism has not been yet elucidated. However, in analogy to what happens in yeast, it may be mediated by the interaction with Atg2.

Isolation membrane elongation and closure are then mediated by two conjugation systems that are similar to that of the ubiquitylation system: the complex Atg12-Atg5-Atg16 and the complex LC3-phosphatidylethanolamine (PE), which function coordinately [39]; [40]. The enzymes Atg7 and Atg10 mediate the conjugation of the ubiquitin-like protein Atg12 with Atg5, which then is stabilized by the interaction with Atg16. This complex, conserved from yeast to mammals, is strictly required for the autophagic membrane development, creates a coating surrounding the vacuole in formation and controls its curvature. Furthermore, this complex is important for the stimulation of the following LC3 conjugation reaction.

LC3 (MAP1-LC3 or LC3B) is synthesized in the pro-LC3 form, which is cut by Atg4 leading to LC3-I generation, and then covalently conjugated to PE by Atg7 and Atg3 through an ubiquitin-like reaction, forming LC3-II [40]. LC3-PE acts as structural component in the vacuole growth, as it is incorporated within both the external and the inner surfaces of the newly forming autophagosome membranes. After the

autophagosome closure, Atg4 mediates the release of PE from the LC3 located on the external surface, in order to recycle LC3-I, whereas the LC3-PE fraction on the inner surface remains stable associated and is subjected to the lysosome degradation. LC3-II localization on the isolation membrane is necessary for its elongation and closure, and the final mature autophagosome formation.

Then, the phagophore expands until its edge fuses around the target in a double-membrane vesicle, named autophagosome. After the maturation stage, the autophagosome fuses with early and late endosomes or multivesicular bodies, leading to the formation of an amphisome [41]. Subsequently, the amphisome docks and fuses with the lysosomal compartment, thus generating the autophagolysosome or autolysosome. The lysosomal enzymes are responsible for the hydrolytic degradation of the cargo within the autophagosome and on the internal side of its membrane. Amino acids and other small molecules obtained from this degradation process can be reused or catabolized, thus are transported back in the cytosol for recycling or energy production.

2.2 Autophagy regulation

Increasing reports highlight the autophagy role as a crucial protein homeostasis regulator, widely interconnected with other numerous intracellular pathways, which is controlled by different signals in a cell context- and organism-specific manner [42]. Autophagy is highly regulated in order to avoid either its excessive or insufficient activation. It is rapidly upregulated when cells require intracellular nutrients and energy, as during high energetic demands, during starvation or growth factor withdrawal. Autophagy is also enhanced when cells are preparing to undergo structural remodelling during development, or in response to different stress stimuli, including cellular volume variations, hypoxia, oxidative stress, damaged proteins and organelles accumulation, hormonal factors, irradiation, and xenobiotics.

The serine/threonine protein kinase mTOR (mechanistic target of rapamycin) is the autophagy major regulator. mTOR is a component of two structurally and functionally distinct complexes, mTORC1 and mTORC2. mTORC1, whose other components are Raptor (regulatory-associated protein of mTOR), GβL/mLST8 (mammalian lethal with Sec13 protein 8), PRAS40 (proline-rich AKT substrate 40 kDa), and Deptor (DEP domain-containing mTOR-interacting protein), exerts a negative regulation on the autophagic process and is rapamycin sensitive. mTORC1 plays a key role in sensing and integrating growth factor and nutrient signals and controls metabolism, energy, cell growth, and oxygen levels. Mitogenic stimuli and amino acids induce the activation of the class I PI3K-Akt-mTORC1 pathway, which is responsible for autophagy inhibition by affecting the first events of the autophagosome formation [43]. The activated mTOR, which is associated with the ULK1-Atg13-FIP200 complex in a ULK1-dependent manner, through Atg13

phosphorylation prevents the association between ULK1 and Atg13, required for ULK1 stabilization and activation [44]. In addition, mTOR inactivates ULK1 by direct phosphorylation at Ser 757 and instead promotes cell growth via p70 S6 kinase and 4E-BP1. By contrast, upon starvation conditions, mTOR inactivation leads to its dissociation from the ULK1 complex, ULK1 and Atg13 dephosphorylation, thus enabling the ULK1 kinase complex function and autophagy initiation [44].

mTORC1 and AMP-activated protein kinase (AMPK) regulate autophagy in a coordinated manner. AMPK is a key cellular energy sensor that acts as a positive autophagy regulator. AMPK is stimulated by an increase in AMP/ATP ratio that can occur upon stress conditions, such as glucose depletion. In low energy conditions, AMPK both phosphorylates and activates the tuberous sclerosis 2 (TSC2) component of the TSC1/2 complex, a negative mTORC1 regulator, and directly inhibits mTORC1 via Raptor phosphorylation, leading to autophagy activation. In addition, AMPK directly activates ULK1 via phosphorylation of Ser 317 and Ser 777, although the phosphorylation mediated by mTOR at Ser 757, and the negative feedback phosphorylation of AMPK by ULK1, is able to overwhelm this activation [45].

In addition, in nutrient-rich conditions mTORC1 phosphorylates TFEB (transcription factor EB) at Ser 122 and thereby TFEB, which regulates the expression of several genes related to autophagy and lysosomal biogenesis, is retained in the cytoplasm. By contrast, upon starvation, TFEB dephosphorylation promotes its translocation to the nucleus [46].

Consistently to the autophagy critical role in the response to stress conditions, in the maintenance of intracellular homeostasis and quality control, several studies have linked dysregulated autophagy to different pathological conditions, including cancer, neurodegenerative and cardiovascular diseases, immune diseases, metabolic disorders, lysosomal storage diseases, and aging. The suppression of autophagy causes the accumulation of proteins and potentially hazardous intracellular structures, thereby inducing high levels of metabolic stress and limiting organelle functionality. Consequently, using a pharmacological approach to re-establish physiological levels of autophagy may be beneficial in treating certain diseases. Nevertheless, several clinical trials are currently based on the employment of agents acting on autophagy induction [47].

Results

1. KRIT1 deletion suppresses autophagy

To study the contribution of autophagy to CCM pathogenesis, we investigated whether KRIT1 down-regulation would lead to the impairment of autophagy in endothelial cell lines. Endothelial-specific KRIT1 knockout (KO) in mice produced lesions that were identical to the CCM malformations observed in humans [48]; [27]. We used KRIT1-KO lung endothelial cells derived from *KRIT1$^{fl/fl}$* mice treated with Tat-Cre recombinase [27].

p62/SQSTM1 acts as a receptor for ubiquitinated cargoes and delivers them to the autophagosome, and p62 itself is incorporated into the autophagosome and subsequently degraded by autophagy [49]. The autophagy protein microtubule-associated protein 1 light chain 3 (LC3) is present in the cytosol in the LC3-I form, until it is modified to a cleaved and lipidated membrane-bound form (LC3-II), which is localized to autophagosomes. Thus, in addition to p62 accumulation, another typical trait of autophagy inhibition consists of increased amounts of the cytosolic non-lipidated form of LC3 (LC3-I) and of total LC3 [50]; [51]. As shown in Figure 5A, KRIT1 deficiency was associated with defective autophagy, displaying increased levels of p62 and total LC3.

Upon autophagy inhibition, p62 has been reported to be present in several types of cytoplasmic inclusions and to display a typical punctate pattern [52]. Importantly, analysis of p62 distribution through immunofluorescence staining revealed a nuclear-enriched pattern with rare cytoplasmic dots in ~60% of KRIT1 wild-type (wt) cells. Conversely, in KO endothelial cells, the protein is primarily cytoplasmatic, forming intense perinuclear bodies with weak staining in the nucleus (Fig. 5B).

To investigate whether defective autophagy in CCM is a cell-autonomous process, we took advantage of *KRIT1* KO (KRIT1-KO) mouse embryonic fibroblasts (MEFs), a previously established and characterized cellular model that allowed the identification of new molecules and mechanisms involved in CCM pathogenesis [28]; [29], providing novel therapeutic perspectives [53]. Compared with KRIT1-KO MEFs re-expressing KRIT1 (Fig. 5C; KO+KRIT1), KRIT1-KO MEFs (Fig. 5C; KO) displayed increased levels of p62 as well as significantly increased levels of total LC3 protein (Fig. 5C). Moreover, immunostaining analysis revealed that KRIT1 depletion led to increases in the number of p62-containing bodies (Fig. 5D), with diameters of approximately 1.5 μm.

Next, we examined whether KRIT1 ablation also inhibits autophagy in human cells. The silencing of KRIT1 suppressed autophagy in both the human cerebral microvascular endothelial cell line hBMEC (Fig. 5E) and the human umbilical vein cell line EA.hy926 (Fig. 5F), as evidenced by increased p62 and LC3 accumulation.

p62 protein expression is highly regulated at the transcriptional level via the JNK pathway [54] or the NRF2 transcription factor, particularly under oxidative stress [55]; [56].

Considering that KRIT1 is involved in reactive oxygen species (ROS) homeostasis [28]; [29], we tested whether p62 accumulation in KRIT1-KO cells was associated with autophagy inhibition rather than with ROS-dependent transcriptional effects. As expected, treatment with the antioxidant N-acetylcysteine (NAC) decreased p62 levels, but the disruption of *KRIT1* still induced p62 accumulation (Appendix Fig. S1A). Moreover, similar results were obtained using the protein synthesis inhibitor cycloheximide (CHX) (Appendix Fig. S1B), further supporting the notion that the inhibition of autophagy-dependent protein turnover upon KRIT1 loss contributes to p62 accumulation. Consistently, no differences in *p62* mRNA levels between wt and KRIT1-KO endothelial cells have been detected (Appendix Fig. S1C). Importantly, when autophagy-mediated degradation is inhibited, p62 appears to be partially detergent insoluble [57]; therefore, the lysates were divided between Triton X-100 (TX-100)-soluble and TX-100-insoluble fractions and subsequently analyzed for their protein content. The loss of KRIT1 in both endothelial cells (Appendix Fig. S1D) and MEFs (Appendix Fig. S1E) promoted increased levels of p62 in both the soluble and insoluble fractions.

Autophagy is responsible for the degradation of large structures such as organelles and protein aggregates [58]; [59]. Consequently, we analyzed whether the defective autophagy observed upon *KRIT1* loss might induce the accumulation of aggresome-like structures. As shown in Fig. 5G, we observed greater colocalization between p62 and aggresomes in endothelial KRIT1-KO cells, as well as extremely high fluorescence intensity of aggresome-like inclusion bodies. The same results have been obtained in different cellular systems, such as MEFs (Fig. 5H) or *KRIT1*-silenced hBMECs and EA.hy926 cells (Appendix Fig. S1F and G), indicating that the loss of KRIT1 promotes the accumulation of aberrant proteins that could be reasonably ascribed to defective autophagy.

These findings suggest that KRIT1 ablation is sufficient to suppress autophagy in a cell-autonomous manner. Indeed, KRIT1 silencing or disruption in four different cellular contexts has been shown to result in the expression of typical markers of defective autophagy, such as increased accumulation of p62 and increased amounts of LC3-I and of total LC3.
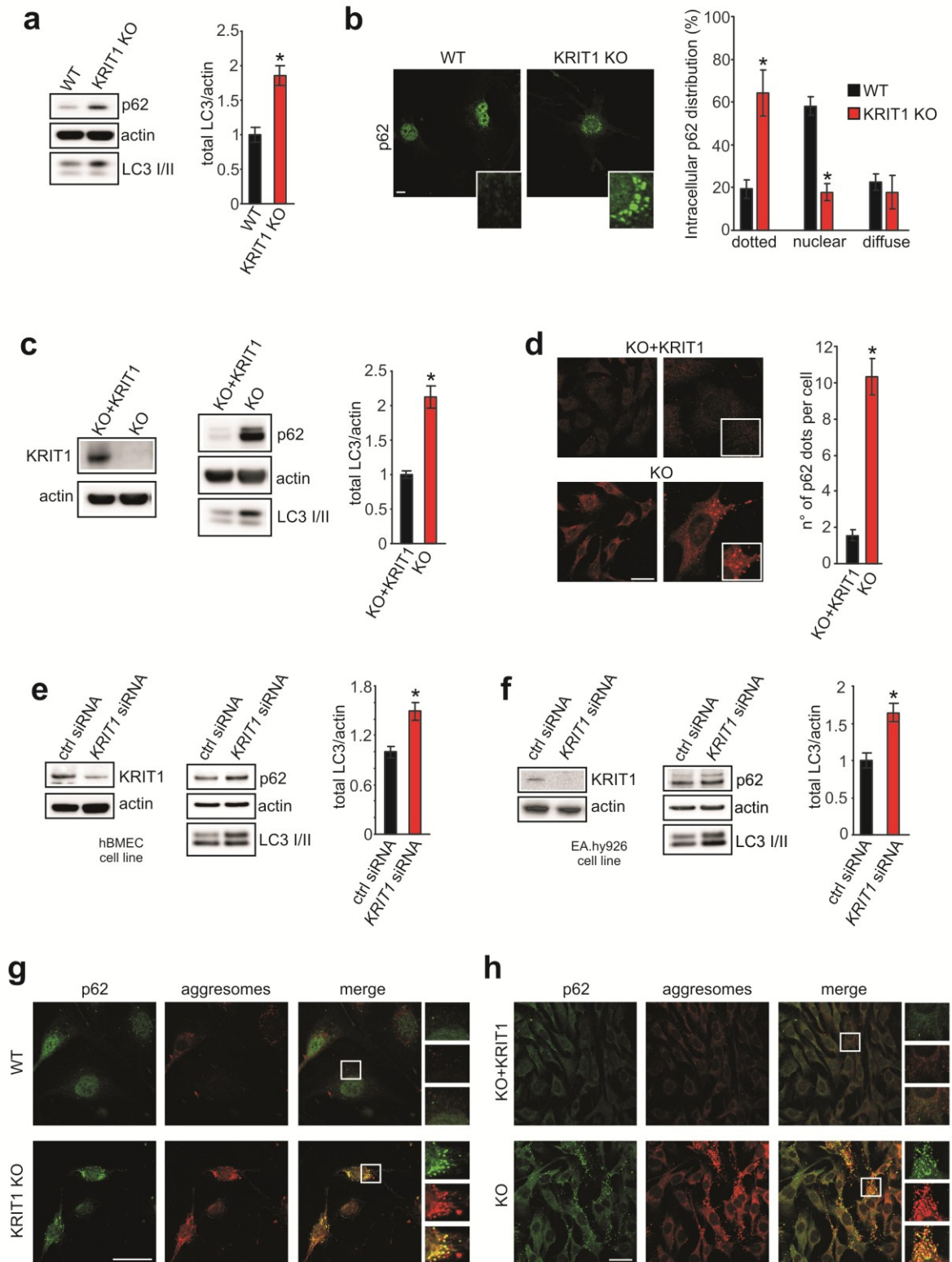
Figure 5. KRIT1-ablated cells display autophagy suppression.

(A) Immunoblot analysis of p62 and LC3 I/II in KRIT1 wt and KRIT1-KO endothelial cells. Actin was used as a loading control. Quantification of total LC3 on actin is reported (*P = 0.02712). The results are representative of three independent experiments. **(B)** Representative images of p62 dots in KRIT1 wt and KRIT1-KO endothelial cells. Scale bar, 20 μm. Magnifications in insets. Right, quantitative analysis of p62 distribution of dots is reported (four independent experiments; n = 35 cells per group). *P = 0.00542 (dotted); *P = 0.00014 (nuclear). **(C)** Immunoblot analysis of p62 and LC3 I/II in KRIT1-KO and KRIT1-KO re-expressing KRIT1 (KO+KRIT1) MEFs. Left, immunoblot showing KRIT1 levels in KRIT1-KO and KO+KRIT1 cells. Right, immunoblots for p62 and LC3 I/II. Actin was used as a loading marker. Quantification of total LC3 on actin is

reported (*P = 0.01248). The results are representative of three independent experiments. **(D)** Representative images of p62 dots in KO+KRIT1 (top) and KRIT1-KO cells (bottom). Scale bar, 50 μm. Magnifications in insets. Right, quantitative analysis of the number of p62 dots per cell is shown (four independent experiments; n = 50 cells per group). *P = 7.18e^{-14}. **(E)** Immunoblot analysis of hBMECs transiently transfected with control siRNA or KRIT1 siRNA. Left, evaluation of siRNA efficiency with antibody directed against KRIT1. Right, immunoblots for p62 and LC3 I/II. Actin was used as a loading marker. Quantification of total LC3 on actin is reported (*P = 0.03071). The results are representative of three independent experiments. **(F)** Immunoblot analysis of EA.hy926 cells transiently transfected with control siRNA or KRIT1 siRNA. Left, evaluation of siRNA efficiency with antibody directed against KRIT1. Right, immunoblot for p62 and LC3 I/II. Actin was used as a loading marker. Quantification of total LC3 on actin is reported (*P = 0.02527). The results are representative of three independent experiments. **(G)** Immunofluorescence analysis of p62 (green) and ProteoStat Aggresome staining detection reagent (red) in KRIT1 wt and KRIT1-KO lung endothelial cells. The yellow signal in the merged images represents an overlapping spatial relationship between green and red fluorescence. Magnification in insets. Scale bar, 50 μm. The images are representative of four independent experiments. **(H)** Immunofluorescence analysis of p62 (green) and ProteoStat Aggresome staining detection reagent (red) in KRIT1-KO re-expressing KRIT1 (KO+KRIT1) and KRIT1-KO MEFs. The yellow signal in the merged images represents an overlapping spatial relationship between green and red fluorescence. Magnification in insets. Scale bar, 50 μm. The images are representative of four independent experiments.
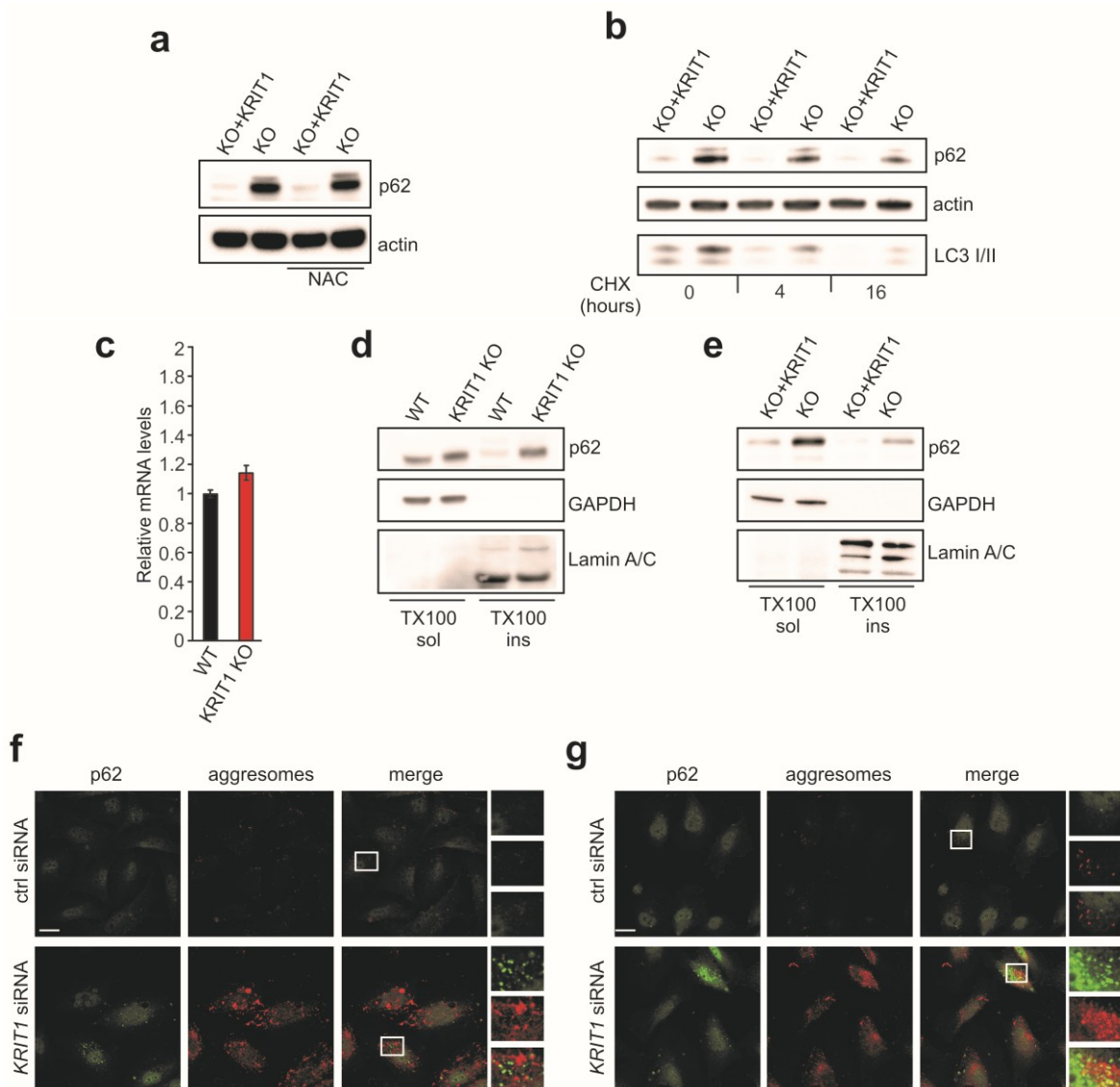
Appendix Figure S1.

◄ **Appendix Figure S1.**

(a) Immunoblot analysis with specific antibody to p62 and actin. Where indicated, KO+KRIT1 and KRIT1 KO MEFs were treated with 20 mM NAC for 24 hours. Results are representative of three independent experiments. **(b)** Immunoblot analysis of p62 and LC3-I/II in CCM1 KO re-expressing KRIT1 (KO+KRIT1) and KRIT1 KO MEFs, treated or not with cycloheximide (CHX) for 4 or 16 hours. Actin was used as loading marker. Results are representative of three independent experiments. **(c)** Gene expression levels of *p62* in WT and KRIT1 KO endothelial cells. Data are mean ± s.e.m of three independent experiments. **(d)** Immunoblot analysis of p62 in detergent-soluble (TX-100 sol) and -insoluble (TX-100 ins) fractions from WT and KRIT1 KO endothelial cells. GAPDH and LAMIN A/C were used as loading markers for soluble and insoluble fractions, respectively. Results are representative of three independent experiments. **(e)** Immunoblot analysis of p62 in detergent-soluble (TX-100 sol) and -insoluble (TX-100 ins) fractions from KO+KRIT1 and KRIT1 KO MEFs. GAPDH and LAMIN A/C were used as loading markers for soluble and insoluble fractions, respectively. Results are representative of three independent experiments. **(f)** Immunofluorescence analysis of p62 (green) and ProteoStat Aggresome staining detection reagent (red) in hBMEC cells, transfected with negative siRNA (ctrl siRNA) or *KRIT1* siRNA. The yellow signal in the merged images represents an overlapping spatial relationship between green and red fluorescence. Magnification in insets. Scale bar, 20 μm. The images are representative of three independent experiments. **(g)** Immunofluorescence analysis of p62 (green) and ProteoStat Aggresome staining detection reagent (red) in EA.hy926 cells, transfected with negative siRNA (ctrl siRNA) or *KRIT1* siRNA. The yellow signal in the merged images represents an overlapping spatial relationship between green and red fluorescence. Magnification in insets. Scale bar, 20 μm. The images are representative of three independent experiments.

2. KRIT1 deletion induces up-regulation of the mTOR-ULK1 pathway

The mTOR signaling network is recognized as the most important regulator of autophagy, and its implication in a wide range of diseases has been largely documented [60]. Direct selective inhibition of mTOR, through the allosteric inhibitor rapamycin or the small molecule ATP-competitive inhibitor Torin1, induces autophagy in many cell types [61]. Consequently, we tested whether the defective autophagy observed upon *KRIT1* deletion resulted from dysregulation of the mTOR pathway. Immunoblot analysis revealed marked up-regulation of mTOR signaling in KRIT1-KO endothelial cells, as evidenced by the increased phosphorylation of both mTOR and its downstream targets p70S6k and 4E-BP1 (Fig. 6A). Importantly, treatment with Torin1 suppressed mTOR activation even in KO cells, suggesting that a pharmacological approach based on mTOR inhibition might re-activate autophagy in these cells.

Among the different targets of mTOR, ULK1, the mammalian homolog of yeast ATG1, is deeply involved in the regulation of autophagy through its interactions with several autophagy-related proteins [36]. For example, ULK1-deficient mice display suppressed autophagy [62]; [63]. mTOR phosphorylates ULK1 at Ser 757 to inhibit autophagy [45]. Notably, mTOR exerts a further restriction on autophagy by indirectly inhibiting ULK1 activity and stability [64]. In our study, endothelial KRIT1 ablation significantly decreased the baseline levels of ULK1 and inhibition of mTOR by Torin1 treatment increased the total amounts of ULK1 protein (Fig. 6B), indicating that reduced ULK1 levels in KRIT1-KO

endothelial cells might be dependent on higher mTOR activity. Indeed, impaired ULK1 stabilization and activity occur when the autophagy regulator AMBRA1 is highly phosphorylated by mTOR kinase at position 52 [64]. As shown in Appendix Fig. S2A, AMBRA1 phosphorylation at Serine 52 is more abundant upon KRIT1 deletion compared to wt endothelial cells.

Then, we tested the efficacy of mTOR inhibition for reinstating autophagy under KRIT1 depletion. As evidenced by the increased LC3-II/I ratios and reduced p62 levels, both rapamycin and Torin1 effectively activated autophagy (Fig. 6C).

Next, we investigated mTOR activity in KRIT1-depleted MEFs. The autophagy defects observed in KRIT1-KO cells could be attributed to alterations of the mTOR-ULK1 pathway (Fig. 6D and E). In this case, we observed only a slight decrease in ULK1 expression in KRIT1-KO MEFs; however, mTOR-dependent phosphorylation of endogenous ULK1 at Ser 757 was increased (Fig. 6E and Appendix Fig. S2B), indicating that mTOR might control ULK1 activity primarily by direct phosphorylation in this cellular context. Interestingly, we observed a significant increase in the total amount of mTOR in both KRIT1-KO endothelial cells and fibroblasts (Fig. 6A and E and Appendix Fig. S2B), which might reasonably affect the totality of active mTOR. The use of rapamycin and mTOR kinase inhibitors significantly re-established autophagy (Fig. 6F). Importantly, the induction of autophagy was more robust in Torin1-treated cells, as evidenced by the greater inhibition of the mTOR pathway by Torin1 (Appendix Fig. S2B). Consistently, Torin1, which is known to inhibit equally the two mTOR functional complexes (mTORC1 and mTORC2), has been reported to be more effective than rapamycin in inhibiting mTORC1, as well as to activate autophagy to a greater extent than rapamycin independently of its putative action on mTORC2 [65]. Therefore, the efficacy of Torin1 treatment to drive autophagy even in KRIT1-KO cells might be likely attributable to its greater effect on autophagy, as compared with rapamycin.

One of the most useful methods for measuring autophagy is based on the mRFP-GFP-LC3 tandem construct assay [50]. In cells expressing mRFP-GFP-LC3, the association of LC3 with autophagosomes can be visualized as yellow puncta due to the merge of green and red, whereas autolysosomes are detected as red puncta because the green fluorescence is quenched by the acidic pH of the lysosomal environment. Thus, if autophagic flux increases (i.e., upon pro-autophagic stimuli), the number of LC3 puncta increases, with a higher number of red puncta than the number of yellow puncta; conversely, when autophagic flux is impaired, only yellow puncta increase without a concomitant increase in red puncta. Both Torin1 and xestospongin B, a mTOR-independent stimulus that induces autophagy by disrupting the molecular complex between inositol 1,4,5-trisphosphate receptor (IP3R) and Beclin-1 [66], activated autophagic flux in wt endothelial cells, whereas only Torin1 re-activated autophagy in KO

cells (Fig. 6G). Similar results were obtained in KRIT1-KO MEFs (Fig. 6H). Notably, KRIT1-KO MEFs also displayed autophagy inhibition at the later stages of the process. This result might be related to the dual suppressive role played by mTOR, which inhibits autophagy not only at the initiation stage via suppression of the ULK1 complex but also at the degradation stage via inhibition of lysosomal function [67]; [68]. Furthermore, the analysis of the lysosomal compartment through the transfection of GFP-tagged lysosomal-associated membrane protein (LAMP1-GFP) revealed the accumulation of clustered lysosomes in KO cells, displaying a morphological pattern similar to that of KRIT1-expressing cells that had been treated with the lysosomal inhibitor bafilomycin A1 (Appendix Fig. S2C).

KRIT1 loss-of-function leads to enhanced levels of intracellular ROS [28] and cell proliferation [27]. Thus, we verified whether autophagy induction counteracts those KRIT1-dependent pathological processes. Measurements of hydrogen peroxide production using the ratiometric mitochondria-targeted HyPer probe (mt-HyPer) showed that Torin1 treatment of KO cells markedly reduced baseline ROS levels (Appendix Fig. S3A). Importantly, the use of antioxidants such as NAC or Tempol did not affect the mTOR signaling over-activation observed in KRIT1-KO cells (Appendix Fig. S3B); accordingly, ROS scavengers failed to trigger autophagy in KO cells (Appendix Fig. S3C), suggesting that ROS accumulation is a consequence of mTOR activity and not *vice versa*. Furthermore, mTOR inhibitors strongly attenuated the proliferative rate of both KRIT1-KO endothelial cells and MEFs (Appendix Fig. S3D and E).

Overall, these data suggest that KRIT1 loss inhibits autophagy through the up-regulation of the mTOR pathway and that the restoration of autophagy by mTOR inhibitors could significantly mitigate the metabolic disorders resulting from KRIT1 loss-of-function.
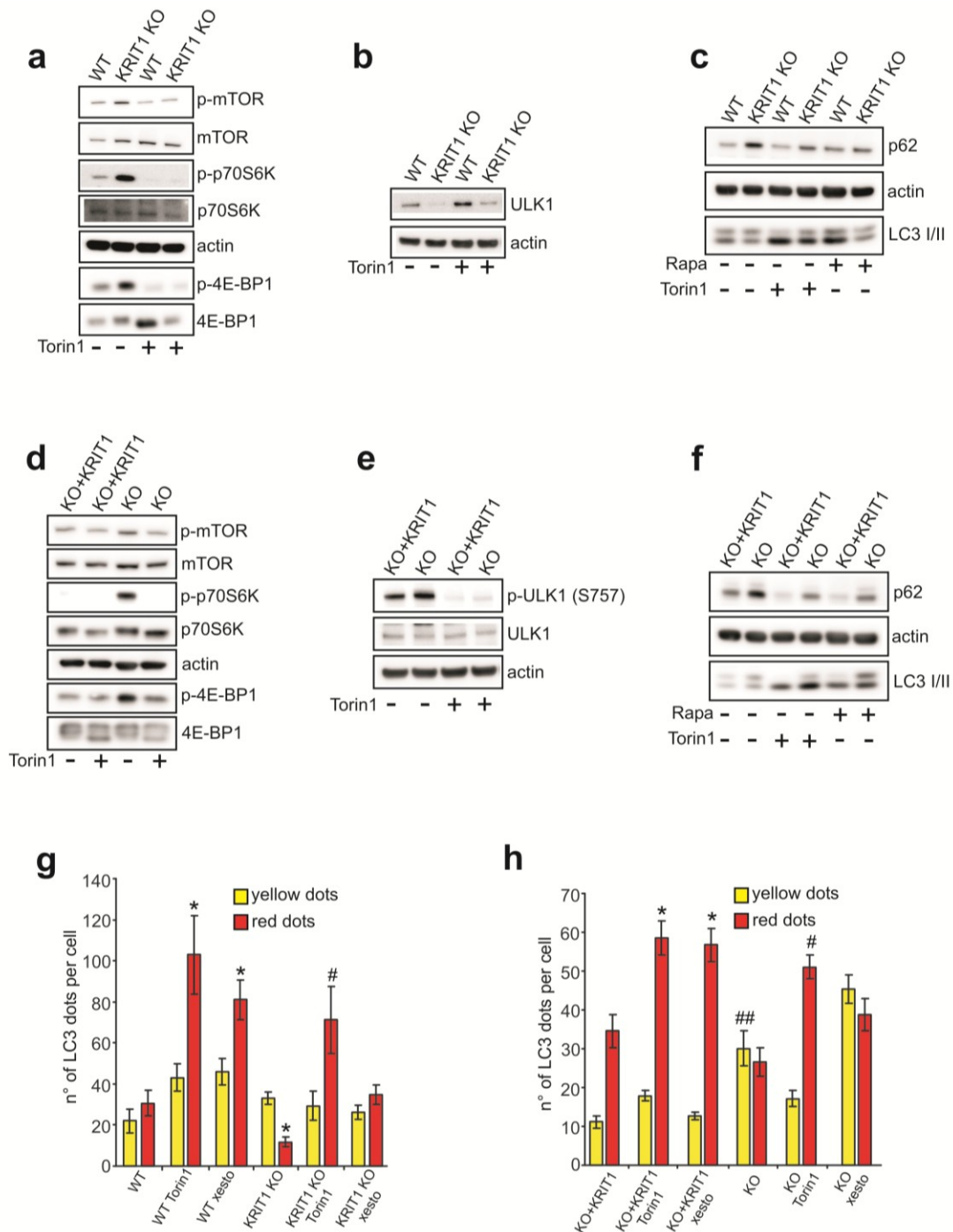
Figure 6. KRIT1 loss-of-function activates the mTOR-ULK1 pathway.

(A) Immunoblot analysis with antibodies directed against phosphorylated mTOR (Ser 2448), total mTOR, phosphorylated p70 S6 Kinase (Ser 371), total p70 S6 Kinase, phosphorylated 4E-BP1 (Thr 37/46), and total 4E-BP1; actin was used as a loading marker. Where indicated, KRIT1 wt and KRIT1-KO endothelial cells were treated with 100 nM Torin1 for 4 h. The results are representative of three independent experiments. **(B)** Immunoblot analysis of total ULK1 and actin in KRIT1 wt and KRIT1-KO endothelial cells. Where indicated, cells were treated with 100 nM Torin1 for 4 h. The results are representative of three independent experiments. **(C)** Immunoblot analysis of p62, LC3 I/II, and actin in KRIT1 wt and KRIT1-KO endothelial cells treated with 100 nM Torin1 or 500 nM rapamycin for 4 h. The results are representative of three independent experiments. **(D)** Immunoblot analysis with antibodies directed against phosphorylated mTOR (Ser 2448), total mTOR, phosphorylated p70 S6 Kinase (Ser 371), total p70 S6 Kinase, phosphorylated 4E-BP1 (Thr 37/46), and total 4E-BP1; actin was used as a loading marker. Where indicated, KRIT1-KO re-expressing KRIT1

24

(KO+KRIT1) and KRIT1-KO MEFs were treated with 100 nM Torin1 for 4 h. The results are representative of three independent experiments. **(E)** Immunoblot analysis of phosphorylated ULK1 (Ser 757), total ULK1, and actin in KRIT1 KO+KRIT1, and KRIT1 KO MEFs. Where indicated, cells were treated with 100 nM Torin1 for 4 h. The results are representative of three independent experiments. **(F)** Immunoblot analysis of p62, actin, LC3 I/II in KO+KRIT1 and KRIT1-KO cells. Where indicated, cells were treated with 100 nM Torin1 for 4 h or 500 nM rapamycin for 4 h. The results are representative of three independent experiments. **(G)** KRIT1 wt and KRIT1-KO endothelial cells were transiently transfected with mRFP-GFP-LC3. Where indicated, the cells were treated with 100 nM Torin1 for 4 h or 2 µM xestospongin B for 4 h. The differences in the autophagic flux were evaluated by counting the yellow LC3 I/II dots/cell (RFP$^+$GFP$^+$) and red LC3 dots/cell (RFP$^+$GFP$^-$) for each condition. Yellow dots: autophagosomes; red dots: autophagolysosomes. *P = 5.74e^{-5} (red dots, WT ctrl vs. WT Tor1); *P = 9.62e^{-5} (red dots, WT ctrl vs. WT xesto); *P = 0.00727 (red dots, WT ctrl vs. KO ctrl); $^\#$P = 0.00046 (red dots, KO ctrl vs. KO Tor1). The data are expressed as the mean ± s.e.m. **(H)** KO+KRIT1 and KRIT1-KO MEFs were transiently transfected with the mRFP-GFP-LC3 tandem construct. Where indicated, the cells were treated with 100 nM Torin1 for 4 h or 2 µM xestospongin B for 4 h. The differences in the autophagic flux were evaluated by counting the yellow LC3 I/II dots/cell (RFP$^+$GFP$^+$) and red LC3 dots/cell (RFP$^+$GFP$^-$) for each condition. Yellow dots: autophagosomes; red dots: autophagolysosomes. *P = 0.00023 (red dots, KO+KRIT1 ctrl vs. KO+KRIT1 Tor1); *P = 0.00045 (red dots, KO+KRIT1 ctrl vs. KO+KRIT1 xesto); $^\#$P = 3.08e^{-6} (red dots, KO ctrl vs. KO Tor1); $^{\#\#}$P = 6.73e^{-5} (yellow dots, KO+KRIT1 ctrl vs. KO ctrl). The data are expressed as the mean ± s.e.m. of four independent experiments.
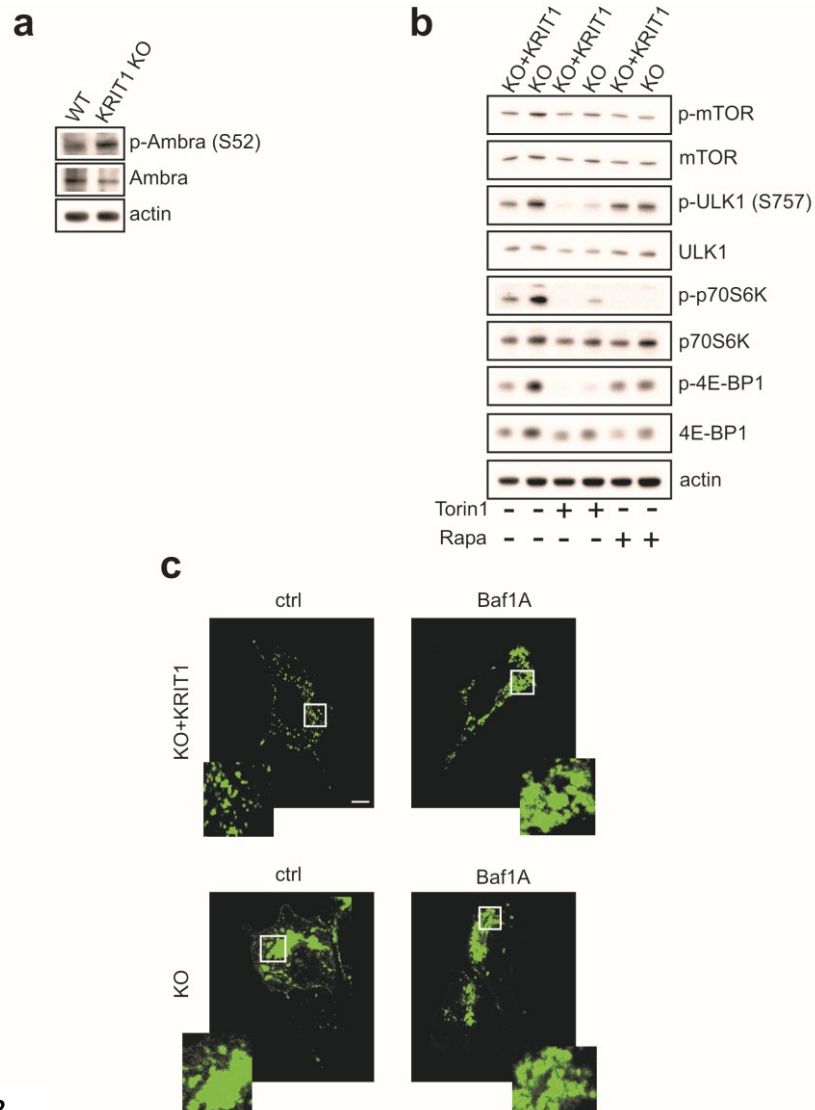
Appendix Figure S2.

(a) Immunoblot analysis of phospho-AMBRA1 (Serine 52), AMBRA1 and actin in WT and KRIT1 KO endothelial cells. Results are representative of three independent experiments. **(b)** Immunoblot analysis of phosphorylated mTOR (Ser 2448), total mTOR, phosphorylated p70 S6 Kinase (Ser 371), total p70 S6 Kinase, phosphorylated 4E-BP1 (Thr 37/46), total 4E-BP1 and actin (loading marker). KRIT1 KO re-expressing KRIT1 (KO+KRIT1) and KRIT1 KO cells were treated or not with 100 nM Torin1 or 500 nM Rapamycin for 4 hours. Results are representative of three independent experiments. **(c)** Confocal microscopy of KRIT1 KO re-expressing KRIT1 (KO+KRIT1) and KRIT1 KO MEFs, transiently transfected with the lysosomal marker LAMP1-GFP. Where indicated, cells were treated with 1 nM Bafilomycin A1 for 4 hours. Scale bar, 10 μm.
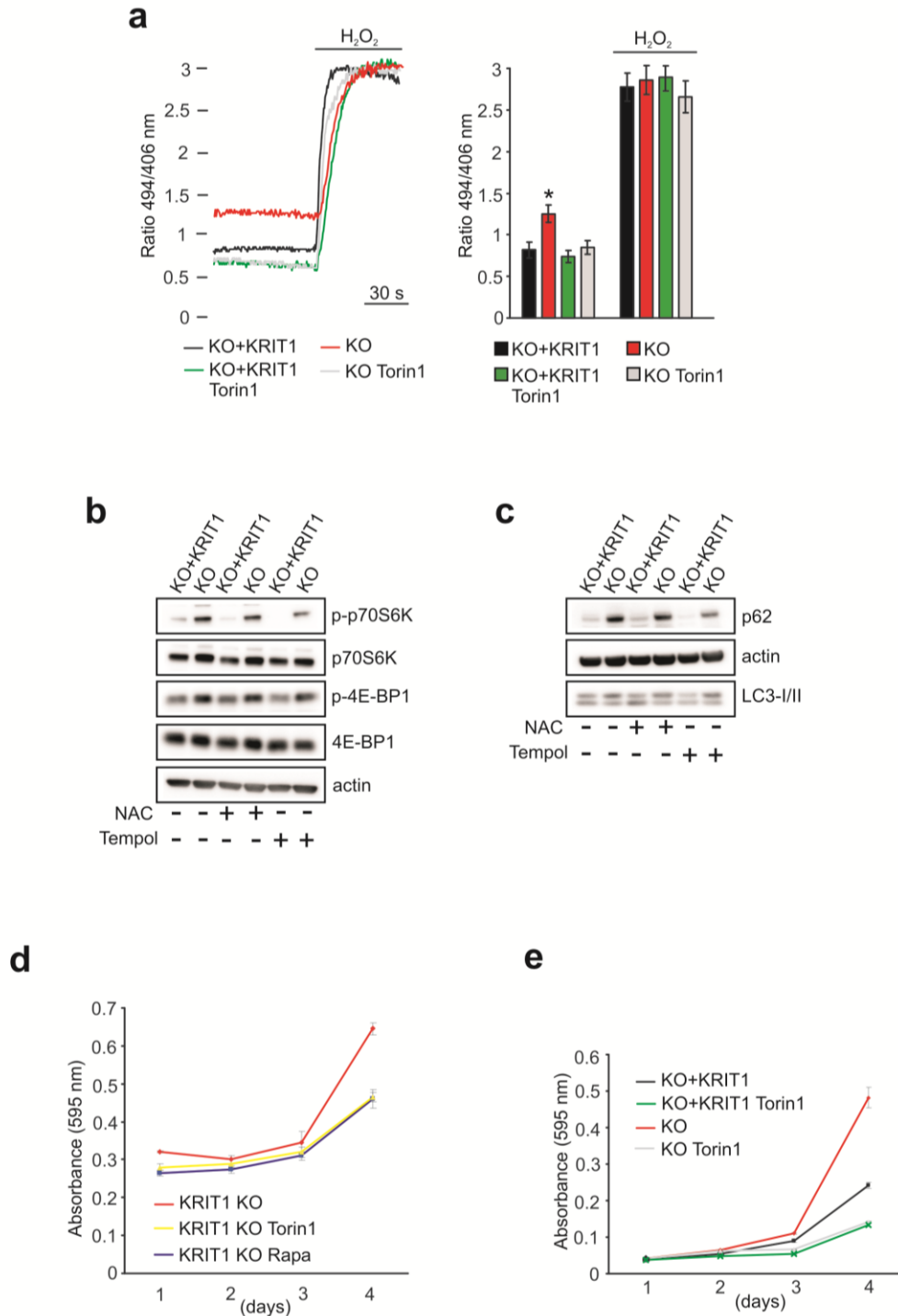
Appendix Figure S3.

(a) KRIT1 KO re-expressing KRIT1 (KO+KRIT1) and KRIT1 KO MEFs were transiently transfected with the genetically-encoded ratiometric H_2O_2 sensor mt-HyPer. Where indicated, cells were treated with 100 nM Torin1 for 16 hours. Time-course traces on the right show a gradual increase in the mt-HyPer ratio only in CCM1 KO cells, reverted by Torin1 treatment. H_2O_2 was added as a reference. Quantifications on the left; *p = 0.01174 (KI ctrl *vs* KO ctrl); n = 26 for each condition. **(b)** Immunoblot analysis of phosphorylated p70 S6 Kinase (Ser 371), total p70 S6 Kinase, phosphorylated 4E-BP1 (Thr 37/46), total 4E-BP1 and actin (loading marker). KRIT1 KO reexpressing KRIT1 (KO+KRIT1) and KRIT1 KO cells were treated or not with 20 mM NAC or 0.5 mM Tempol for 16 hours. Results are representative of three independent experiments. **(c)** Immunoblot analysis of p62, LC3 and actin (loading marker). KRIT1 KO re-expressing KRIT1 (KO+KRIT1) and KRIT1 KO cells were treated or not with 20 mM NAC or 0.5 mM Tempol for 16 hours. Results are representative of three independent experiments. **(d)** Proliferation of vehicle- 500 nM Rapamycin- or 100 nM Torin1-treated KRIT1 KO endothelial cells. Data are mean ± s.e.m of three independent experiments. **(e)** Proliferation of vehicle- or Torin1-treated KRIT1 KO re-expressing KRIT1 (KO+KRIT1) and KRIT1 KO MEFs. Torin1 was used at a concentration of 100 nM. Data are mean ± s.e.m of three independent experiments.

3. Defective autophagy underlies major phenotypic signatures of CCM disease

To further clarify whether defective autophagy is involved in the pathogenesis of CCM, we investigated the relationship between autophagy and endothelial-to-mesenchymal transition (EndMt), a pathological signature that contributes to CCM progression [27]. KRIT1-KO endothelial cells displayed higher expression of typical markers that are associated with EndMt, such as *PAI1* (also known as *Serpine1*), *Cd44*, and *Id1* (Fig. 7A). Both Torin1 and rapamycin treatments inhibited the EndMt switch by lowering the expression of mesenchymal markers (Fig. 7A) and by increasing the levels of key endothelial markers such as CD31 (also known as Pecam-1) and vascular endothelial cadherin (VE-cadherin) (Fig. 7B).

Down-regulation of the essential autophagy-related gene *ATG7* in human umbilical vein endothelial cells (HUVECs) suppressed autophagy (Appendix Fig. S4A) and was associated with changes in the expression of markers of EndMt, such as a decrease in endothelial markers (CD31 and VE-cadherin) and a complementary increase in mesenchymal markers (N-cadherin and alpha-SMA; Fig. 7C). Moreover, *ATG7* silencing in HUVECs slowed the formation of capillary-like structures (Fig. 7D) but significantly increased the migratory capacity of these cells (Appendix Fig. S4B). Importantly, inhibition of mTOR signaling reduced the migration of KRIT1-KO endothelial cells (Appendix Fig. S4C and D).

Considering the p62 significant role in the regulation of epithelial-mesenchymal transition [69], we investigated this aspect in the context of EndMt. Consistently, p62 down-regulation in KRIT1-ablated endothelial cells significantly lowered the expression of mesenchymal markers such as *PAI1*, *Cd44*, and *Id1* (Appendix Fig. S4E), further

supporting the existence of a significant correlation between EndMt and autophagy in CCM.

Because mutations in any of the three *CCM* genes lead to the onset of similar pathological signatures, the three CCM proteins likely share a common mechanism of action. Therefore, we examined the role of autophagy in CCM3-depleted endothelial cells derived from *Ccm3$^{fl/fl}$* mice [70]. Similar to KRIT1 down-regulation, we observed autophagy inhibition upon CCM3 ablation, which could be re-activated by treatment with mTOR inhibitors (Fig. 7E). Importantly, CCM3-KO endothelial cells displayed mTOR-ULK1 pathway up-regulation (Appendix Fig. S4F).

To confirm the data observed *in vitro*, we analyzed whether autophagy inhibition also occurred *in vivo* upon CCM3 ablation. As in patients with CCM [71], an inducible and endothelial-specific CCM3-KO mouse model (*CCM3*-ECKO) presented venous malformations at the periphery of the retinal vascular plexus. We found that p62 strongly accumulated in the endothelial cells that formed the vascular malformations (Fig. 7F and Appendix Fig. S4G). Moreover, an analysis of murine CCM3-KO brain sections showed p62 clusters in the surrounding area of vascular malformations (Fig. 7G).

To complete the analysis of all three CCM genes, we investigated the effect of CCM2 down-regulation in human endothelial cells on autophagy. *CCM2* silencing in EA.hy926 cells (Appendix Fig. S5A) induced p62 accumulation, as well as increased levels of LC3-I and LC3-II (Appendix Fig. S5B). Moreover, immunofluorescence staining showed a punctate pattern of p62 and the accumulation of aggresomes (Appendix Fig. S5C). These autophagy defects could be related to mTOR pathway hyperactivation (Appendix Fig. S5D and E).

Our findings suggest that defective autophagy and consequent p62 accumulation are common features of loss-of-function mutations of the three known CCM genes.
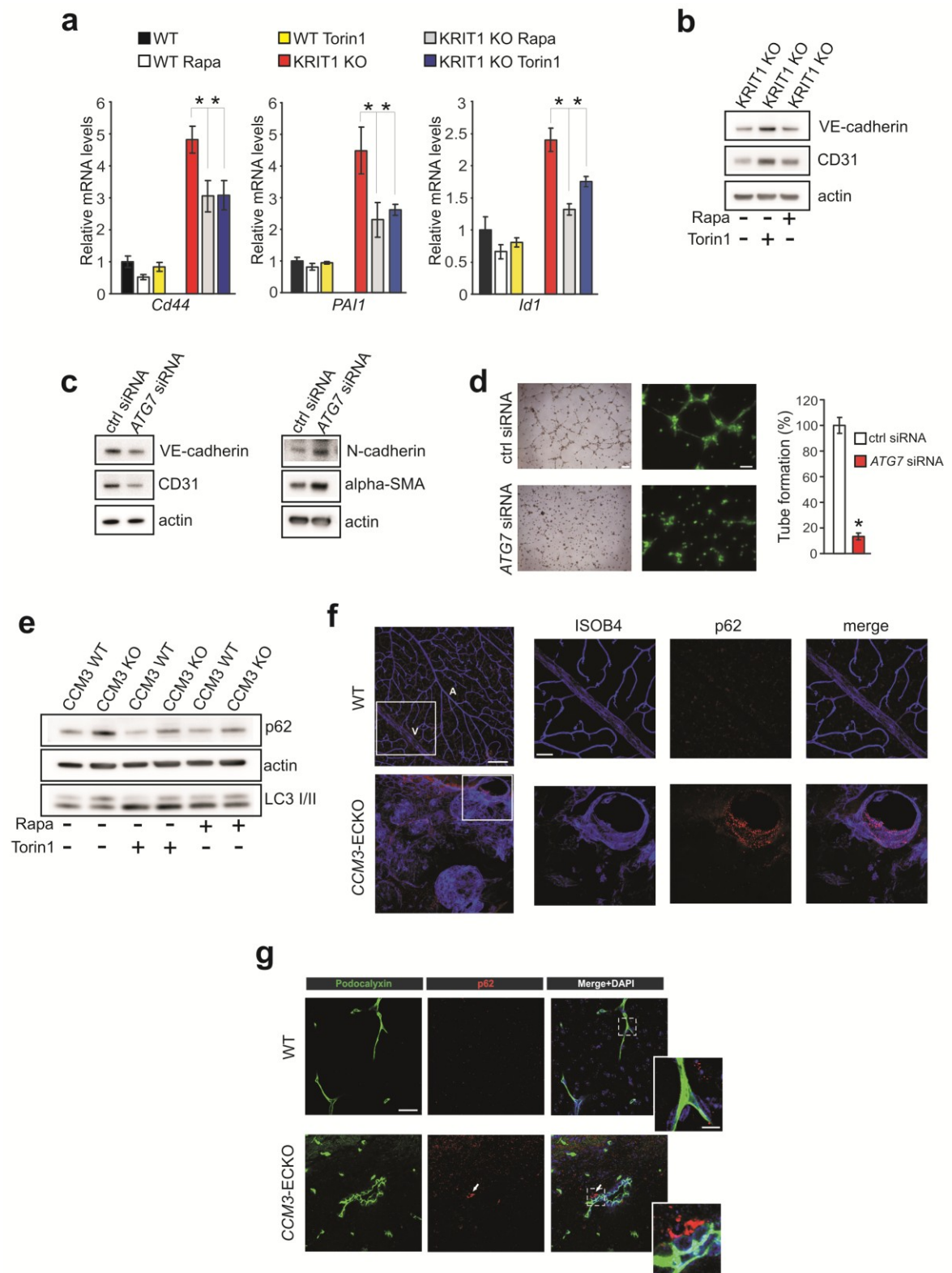
Figure 7. Defective autophagy underlies major phenotypic signatures of CCM disease.

(A) *Cd44*, *PAI1* (also known as *Serpine1*), and *Id1* mRNA expression levels in KRIT1 wt and KRIT1-KO endothelial cells were assessed by quantitative real-time PCR. Where indicated, KRIT1 wt and KRIT1-KO endothelial cells were treated with 100 nM Torin1 or 500 nM rapamycin for 16h. The data are expressed as the mean ± s.e.m. *Cd44*: *P = 0.02848 (KO ctrl vs. KO Rapa); *P = 0.02605 (KO ctrl vs. KO Tor1). *PAI1*: *P = 0.04446 (KO ctrl vs. KO Rapa); *P = 0.03996 (KO ctrl vs. KO Tor1). *Id1*: *P = 0.00266 (KO ctrl vs. KO Rapa); *P = 0.01554 (KO ctrl vs. KO Tor1). n = 3 independent experiments. **(B)** Immunoblot analysis of CD31/Pecam-

1, vascular endothelial cadherin (VE-cadherin), and actin in KRIT1-KO endothelial cells that were treated with 100 nM Torin1 or 500 nM rapamycin for 24 h. The results are representative of three independent experiments. **(C)** Immunoblot analysis of CD31/Pecam-1, vascular endothelial cadherin (VE-cadherin), N-cadherin, alpha-smooth muscle actin (alpha-SMA), and actin in HUVECs transfected with control siRNA or *ATG7* siRNA. **(D)** Formation of capillary-like structures measured by tube formation assays. HUVECs were transfected with control siRNA or *ATG7* siRNA for 72 h. Representative phase-contrast (Scale bar, 100 μm) and calcein-fluorescent (Scale bar, 50 μm) images were reported. All data are presented as percentage ± s.e.m from three different experiments performed in duplicate. *P = 1.29e^{-11}. **(E)** Immunoblot analysis of p62, LC3 I/II, and actin in CCM3 wt and CCM3-KO endothelial cells treated with 100 nM Torin1 or 500 nM rapamycin for 4 h. The results are representative of three independent experiments. **(F)** Representative immunostaining of retina sections from wt and a model of inducible and endothelial-specific CCM3-KO (*CCM3*-ECKO) at postnatal day 14. Endothelium was stained with isolectin B4 (ISOB4) (blue). A, artery; V, vein. p62 aggregates can be observed in endothelial cells forming retinal lesions in *CCM3*-ECKO animals (scale bar: 200 μm). Scale bar of magnifications: 100 μm. **(G)** Representative immunostaining of brain sections from wt and a model of inducible and endothelial-specific CCM3-knockout mice (*CCM3*-ECKO) at postnatal day 9. p62 aggregates can be observed in the proximity of CCM lesions (arrows). Cell nuclei (DAPI) are in blue. Scale bar, 30 μm. Smaller panel shows the magnifications of blood vessels (green). Scale bar, 10 μm.
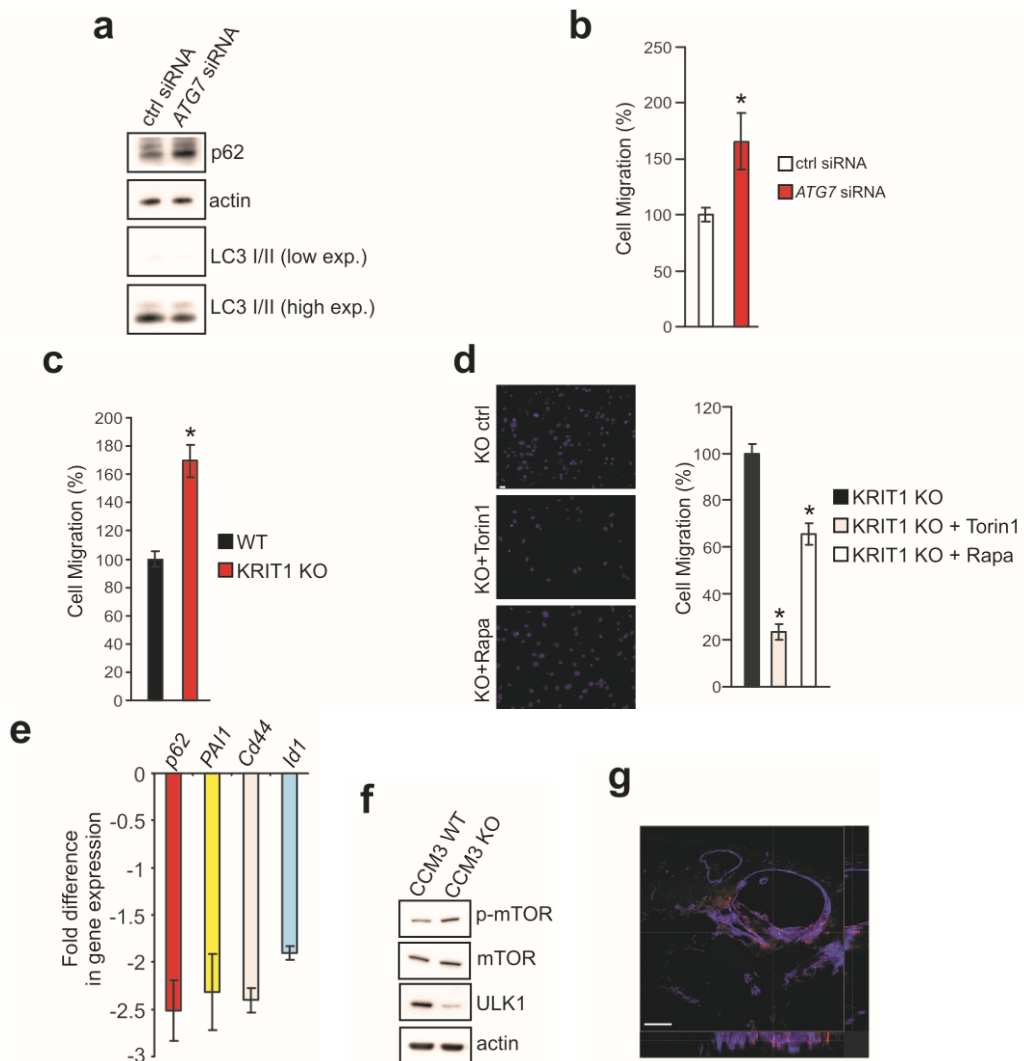
Appendix Figure S4.

◄ Appendix Figure S4.

(a) Immunoblot analysis of p62, actin, LC3I/II in HUVEC transfected negative siRNA (ctrl siRNA) or *ATG7* siRNA, for 72 hours. Results are representative of three independent experiments. **(b)** Cell migration (expressed as percentage) of HUVEC transfected with negative siRNA (ctrl siRNA) or *ATG7* siRNA, for 72 hours. Results are representative of three independent experiments, performed in triplicate. *p = 0.01477. **(c)** Cell migration (expressed as percentage) of WT and KRIT1 KO endothelial cells. Results are representative of three independent experiments, performed in triplicate. *p = 2.98e^{-6}. **(d)** Cell migration (expressed as percentage) of KRIT1 KO endothelial cells treated with vehicle (KO ctrl), 100 nM Torin1 (KO+Torin1) or 500 nM Rapamycin (KO+Rapa) for 24 hours. Representative DAPI-fluorescent (20x magnification; scale bar: 10 µm) images have been reported. Results are representative of three independent experiments, performed in triplicate. *p = 3.25e^{-23} (ctrl *vs* Torin1); *p = 2.65e^{-7} (ctrl *vs* Rapa). **(e)** Gene expression levels of EndMt markers in *p62* and control short interfering RNA (siRNA) in CCM1 KO endothelial cells. Fold changes in *p62* siRNA versus control. **(f)** Immunoblots analysis with antibodies specific to phosphorylated mTOR (Ser 2448), total mTOR and total ULK1 in CCM3 WT and CCM3 KO endothelial cells; actin was used as loading marker. Results are representative of three independent experiments. **(g)** 3D reconstruction of *CCM3-ECKO* merged images showed in Figure 3f, obtained with confocal Z-stack, shown in orthogonal view. Scale bar: 100 µm.

Appendix Figure S5.

4. Enhanced p62 accumulation occurs in endothelial cells lining in human CCM lesions

To examine the clinical relevance of our findings in cellular and animal models of CCM disease, we analyzed p62 expression in human CCM lesions. Indeed, p62 accumulates in several autophagy-deficient mouse tissues [72]; [73] and p62 represents a reliable marker for tissues with reduced autophagic activity [74]. Histological samples of human CCM lesions were obtained from archived paraffin-embedded surgically resected CCM specimens, and p62 levels were evaluated by immunohistochemical studies. The analysis of CCM specimens from 10 cases with confirmed diagnosis of CCM by both neuroradiological and histopathological analyses revealed enhanced staining intensity for p62 in endothelial cells lining CCM lesions (Appendix Table S1). Representative immunohistochemical results for the selected cases are shown in Figure 8. While normal brain vascular endothelium deriving from autoptic samples showed negative staining for p62 (Fig. 8A and B), either moderate (Fig. 8C and D) or marked (Fig. 8E and F) "pearl necklace-like" endothelial staining for p62 was observed in the ten CCM cases analyzed (Fig. 8C-F and Appendix Table S1). Intriguingly, a putative association between marked p62 accumulation and the multiple CCM lesion phenotype was also observed (Appendix Table S1), which deserves further investigation in larger samples for validation. Notably, in one of the eight tissue samples that displayed marked positive p62 staining in CCM lesions, typical normal vessels surrounding the lesion were also present and stained negative for p62, resulting in an internal negative control (Fig. 8G-I). Taken together, these data demonstrate that p62 accumulates in endothelial cells lining CCM brain lesions, supporting the clinical relevance of defective autophagy in CCM disease.
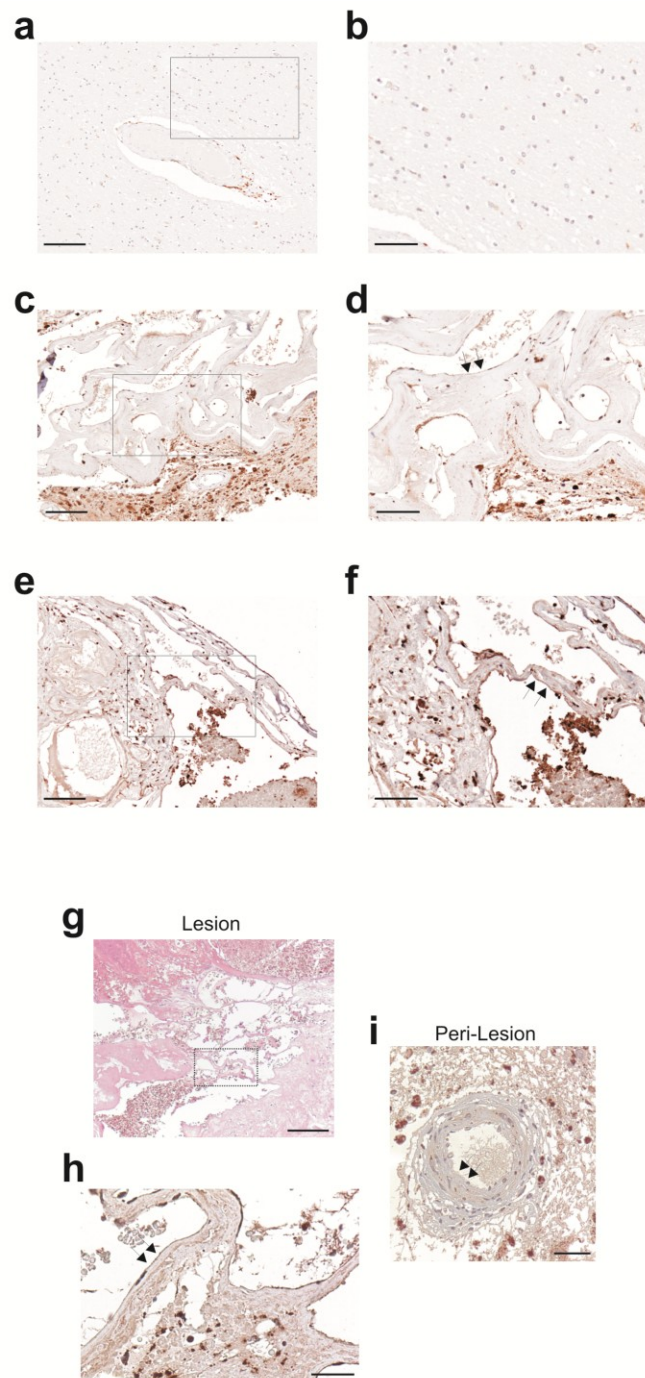
Figure 8. Accumulation of p62 in endothelial cells lining human CCM lesions.

p62 immunohistochemical (IHC) staining in human brain tissue. **(A, B)** Normal vascular endothelium of autoptic brain parenchyma samples is lacking the typical autophagic p62 granules as shown by the negative staining for p62. Scale bars: (A) 200 µm; (B) 100 µm. **(C-F)** Two different representative samples of CCM lesions with a thin, single layer brain endothelium displaying either moderate (C, D) or marked (E, F) positive perinuclear "pearl necklace-like" immunostaining for p62 granules. (C, D), case n° 4 (p62^{++}), and (E, F), case n° 8 (p62^{+++}) are representative of CCM cases listed in Appendix Table S1. Scale bars: (C, E) 200 µm; (D, F) 100 µm. Arrows indicate endothelial p62 positive staining. **(G-I)** Hematoxylin and eosin (H&E) staining (G) and p62 immunohistochemical analysis (H, I) of a CCM surgical sample (case n° 6 in Appendix Table S1) containing normal vessels in the peri-lesional area, which served as an internal control. Notice marked p62-positive staining in endothelial cells lining a CCM lesion (H, arrows) and p62-negative staining in endothelial cells lining a normal peri-lesional vessel (I, arrows). Scale bars: (G) 300 µm; (H, I) 100 µm. Background

33

staining in brain parenchyma surrounding CCM lesions may be attributed to either cell debris or p62 immunoreactivity in neuronal and glial cells.

Cases	Histological number	Stain Intensity	Multiple Lesions	Single large Lesion
1	2554/2013	+++	X	
2	8189/2012	+++	X	
3	6292/2003	+++	X	
4	9008/2012	++		X
5	2414/2007	+++	X	
6	7369/2007	++		X
7	760/2004	+++	X	
8	9368/2010	+++	X	
9	6577/2011	+++	X	
10	10490/2012	+++	X	

Appendix Table S1: Clinical records related to CCM specimens used in this study.
Formalin-fixed, paraffin-embedded surgically resected CCM specimens were retrieved from the archives of the Department of Anatomy and Diagnostic Histopathology at the "Città della Salute e della Scienza" University Hospital, Turin, Italy. Only archived specimens with confirmed diagnosis of CCM by both neuroradiological and histopathological analyses were included in the study.

From: Marchi S, Corricelli M, Trapani E, Bravi L, Pittaro A, Delle Monache S, Ferroni L, Patergnani S, Missiroli S, Goitre L, Trabalzini L, Rimessi A, Giorgi C, Zavan B, Cassoni P, Dejana E, Retta SF, Pinton P (2015) *Defective autophagy is a key feature of cerebral cavernous malformations.* EMBO Mol Med 7(11):1403-17.

Discussion

Cerebral Cavernous Malformation (CCM) is a dysplasia occurring mainly within the central nervous system, characterized by abnormally enlarged and leaky capillaries, which can lead to severe clinical symptoms, as neurological deficits, stroke and intracerebral hemorrhage (ICH) [1]; [2]; [3]; [4]. Causative loss-of-function mutations have been identified in three genes, *KRIT1, CCM2, and CCM3* [5]. At present, no direct therapies for CCM disease exist. Therefore, useful insights into the definition of novel pharmacological approaches for CCM disease prevention and treatment could derive from a deep understanding of the mechanisms underlying CCM pathogenesis. Autophagy is a degradation process responsible for the maintenance of intracellular homeostasis and quality control [30]. Numerous reports have strongly linked dysregulated autophagy and numerous human diseases, including human cancer [75]. Additionally, CCM disease shares multiple molecular features with tumors, although the clinical outcomes are completely different.

Our data reveal that defective autophagy can now be considered a key aspect of CCM and we propose the inhibition of mTOR-ULK1 signalling as a promising therapeutic approach. Moreover, our results correlate the defective autophagy to the loss-of-function mutations of the three CCM genes, based on the observations made upon KRIT1 depletion, in CCM3-KO cells and tissues, and in CCM2 silenced cells, but also in human sporadic lesions, highlighting the clinical significance of our findings.

Upon KRIT1 silencing or disruption, four different cell lines displayed the typical features of defective autophagy, as increased amounts of p62/SQSTM1, LC3-I and total LC3 (Fig. 5A, C, E and F), which indicate a block in the completion of the autophagic process [50], and p62 accumulation in cytoplasmic inclusions (Fig. 5B and D), which is also a typical feature of autophagy inhibition already observed to occur in neurodegenerative diseases [52]. Furthermore, the augmented levels of p62 in both soluble and insoluble fractions (Appendix Fig S1D and E), which is consistent with previous observations made under defective autophagy and high protein aggregation conditions [74]; [76]; [77], and the enhanced p62 colocalization with aggresomes (Fig. 5G and H, Appendix Fig S1F and G), indicate that KRIT1 ablation leads to aberrant proteins accumulation. Similar observations have been reported for other autophagy-deficient scenarios [78]; [79].

We demonstrated that KRIT1 depletion induces autophagy inhibition through the dysregulation of the mTOR-ULK1 pathway. mTOR exterts a pivotal role in the control of the autophagic process, which appears altered in several human diseases [60], while ULK1 is directly involved in the autophagic process and ULK1-deficient mice display suppressed autophagy [62]; [63]. Our data show that CCM1 loss-of-function induces mTOR pathway up-regulation (Fig. 6A, D, Appendix Figure S2A and B) and a consequent

inhibition of pro-autophagic ULK1 activity not only by phosphorylation (Fig. 6E, Appendix Figure S2B), but also reducing its protein expression (Fig. 6B). The dual regulation of ULK1 has been yet described as highly mTOR-dependent [45]; [64]; [62].

Both the mTOR inhibitors rapamycin and Torin1 strongly suppressed mTOR hyperactivation and efficiently re-activated autophagy upon *KRIT1* depletion (Fig. 6A-H, Appendix Figure S2B). These evidences imply that mTOR inhibitors might extensively counteract the metabolic disorders KRIT1-dependent. In fact, autophagy re-activation through mTOR inhibitors significantly reduced the cell migration (Appendix Figure S4C and D), the ROS levels (Appendix Fig S3A), and the cell proliferation (Appendix Fig S3D and E), which have been observed to be enhanced in consequence of KRIT1 loss-of-function [28]; [27].

We associated the autophagy impairment to endothelial-to-mesenchymal transition (EndMt). It has been previously established the EndMt involvement in CCM progression [27] and the p62 crucial role in the regulation of epithelial-mesenchymal transition [69]. We observed higher levels of the typical EndMt markers upon KRIT1 ablation and, importantly, Torin1 and rapamycin treatments counteracted the EndM switch (Fig. 7A and B).

In conclusion, we identified a key role for the autophagy inhibition in the development of CCM disorder and suggest the utilization of mTOR inhibitors, which are currently used in several clinical trials, including the treatment of complicated vascular anomalies [80], as a promising therapeutic strategy for treating CCM disease and improve the long-term prognosis of CCM patients. Recent observations regarding the role of mTOR in arteriovenous malformations [81], the higher number and tortuosity of tumor microvessels in Atg5[EC-KO] mice carrying an endothelial cell-specific deletion of the autophagy-related gene *Atg5* [82], and the involvement of autophagy in CCM3-dependent senescence induction [83], provide further support to our data, strengthening the original finding that CCM is an autophagy-related disease.

Materials and methods

Immunoblotting

For immunoblotting, cells were scraped into ice-cold, phosphate-buffered saline (PBS) and lysed in a buffer containing 50 mM Tris HCl pH 7.4, 150 mM NaCl, 1% Triton X-100, 0.2% SDS, protease, and phosphates inhibitor cocktail. After 30 min of incubation on ice and centrifugation at 2,500 rpm 4°C for 5 min, proteins were quantified by the Lowry method and 10 µg of each sample were loaded on a Novex NuPage Bis-Tris 4-12% precast gel (Life Technologies) and transferred to PVDF membranes. After incubation with TBS-Tween-20 (0.05%) supplemented with 5% non-fat powdered milk for 1 h to saturate unspecific binding sites, membranes were incubated overnight with primary antibodies. The revelation was assessed by appropriate horseradish peroxidase-labeled secondary antibodies (Santa Cruz Biotechnology), followed by detection by chemiluminescence (ThermoScientific), using ImageQuant LAS 4000 (GE Healthcare).

Antibodies

For immunofluorescence and Western blotting, the following primary antibodies were used: rabbit anti-p62 (1:2,000 for Western blot; 1:100 for immunofluorescence), mouse anti-β-actin (1:10,000), rabbit anti-LC3B (1:1,000), rabbit anti-CCM2 (1:1,000), and rabbit anti-AMBRA1 (1:1,000) from Sigma-Aldrich; rabbit anti-GAPDH (1:5,000), rabbit anti-mTOR (1:1,000), rabbit anti-phospho-mTOR (Ser2448) (1:1,000), rabbit anti-p70 S6 Kinase (1:1,000), rabbit anti-phospho-p70 S6 Kinase (Ser 371) (1:1,000), rabbit anti-4E-BP1 (1:1,000), rabbit anti-phospho-4E-BP1 (Thr 37/46) (1:1,000), rabbit anti-ULK1 (1:1,000), and rabbit anti-phospho-ULK1 (Ser 757) (1:500) from Cell Signaling; rabbit anti-phospho-AMBRA1 (Ser 52) (1:1,000) from Millipore; rabbit anti-alpha-SMA (1:1,000) from NovusBio; mouse anti-N-cadherin (1:500) from Invitrogen; goat anti-CD31/Pecam-1 (1:1,000), mouse anti-LAMIN A/C (1:1,000), and mouse anti-VE-cadherin (1:500) from Santa Cruz Biotechnology; and rabbit anti-KRIT1 (1:500) from S.F. Retta.

Reagents

Chemicals used were the following: N-acetylcysteine (NAC; Sigma-Aldrich), Bafilomycin A1 (BafA1; Sigma-Aldrich), Torin1 (Torin1; Calbiochem), Rapamycin (Rapa; Calbiochem), and Cycloheximide (CHX; Sigma-Aldrich).

Cell cultures and transfections

KRIT1 wt, KRIT1 KO, and KRIT1 KO re-expressing KRIT1 mouse embryonic fibroblasts (MEFs) were provided by S.F. Retta [28] and cultured in a humidified 5% CO_2, 37°C

incubator in Dulbecco's modified Eagle's medium (DMEM) supplemented with 10% fetal bovine serum (FBS; Life Technologies), 2 mM L-glutamine, 100 U/ml penicillin (EuroClone), and 100 mg/ml streptomycin (EuroClone).

KRIT1 wt, KRIT1 KO, CCM3 wt, and CCM3 KO endothelial cells were provided by E. Dejana. Endothelial cells were cultured in a humidified 5% CO_2, 37°C incubator on 0.1% gelatin-coated 75 cm^2 Falcon flasks in MCDB 131 Medium (Life Technologies) supplemented with 20% FBS, 2 mM L-glutamine, 1 mM sodium pyruvate, 100 U/ml penicillin and 100 mg/ml streptomycin, 100 µg/ml heparin, and 50 µg/ml Endothelial Cell Growth Supplement (ECGS, Sigma-Aldrich). Transient transfections were performed using JetPEI (Polyplus transfection™) and Lipofectamine 2000 (Life Technologies) as transfecting reagents, according to the manufacturer's instructions.

Human umbilical vein endothelial cells (HUVECs) were purchased from Life Technologies and cultured in Medium 200 supplemented with low serum growth supplement (LSGS). The cells in the present study were used in passages 2-6. Transfections were performed using Lipofectamine RNAiMax (Life Technologies) as transfecting reagent, according to the manufacturer's instructions. ATG7 and negative siRNAs were purchased from Cell Signaling.

The human cerebral microvascular endothelial cells (hBMEC) were purchased from ScienceCell Research Laboratory (Carlsbad). The hBMECs were grown in EGM-2MV medium (Lonza). Cells were grown on 6-well plates and coated with rat tail collagen type-I (BD Biosciences). The human umbilical vein cell line, EA.hy926, established by fusing primary human umbilical vein cells with a thioguanine-resistant clone of A549, was purchased by ATCC and cultured in Dulbecco's modified Eagle's medium (DMEM-Sigma-Aldrich, St Louis, MO, USA) supplemented with 10% FBS, 2 mM L-glutamine, and 1% penicillin/streptomycin. The cells were maintained in a 37°C incubator in a humidified atmosphere containing 5% CO_2.

hBMEC cells (2.5×10^5 per well) were subjected to two rounds of transfection with siRNA targeting KRIT1 or a scrambled control. Briefly, cells were passaged into 25 nM siRNA with 1:166 HiPerFect reagent (Qiagen) in 4:1 EGM-2MV, respectively, and plated. After an overnight incubation in the transfection mix, cells were washed and fed with EGM-2MV. After an additional 48 h, the transfection process was repeated to achieve more complete knockdown. During the second transfection, cells were seeded into assay plates as described below. Cells were again fed with EGM-2MV completed medium after overnight incubation with the transfection mix. After an additional 48-72 h, cells were subjected to experimental conditions.

EA.hy926 endothelial cells were plated in 10-cm culture dishes in 8 ml antibiotic-free standard growth medium supplemented with FBS. Cells were grown to 60% confluence and then transfected for 5 h at 37°C with KRIT1 or control siRNAs (final concentration:

100 nmol/l). Specifically, silencing experiments were performed using a mix of 4x pre-designed iBONi siRNA against KRIT1 target gene. IBONi positive and negative controls were purchased from Ribbox Life Sciences. Cell transfections were performed using INTERFERin kit (Polyplus transfection) according to the manufacturer's protocol. Cells were cultured with siRNAs for 24 h before treatments and analysis.

For *CCM2*-silencing experiments, transfections were performed using Lipofectamine RNAiMax (Life Technologies) as transfecting reagents, according to the manufacturer's instructions. CCM2 and negative siRNAs (final concentration 40 nM) were purchased from Life Technologies.

Immunohistochemical analysis

The study was performed according to the standards of the Institutional Ethical Committee and the Helsinki Declaration and was approved by the Institutional Review Board of our hospital. Specifically, approval was given by the ethic institutional review board for "Biobanking and use of human tissue for experimental studies" of the Pathology Services (Azienda Ospedaliera Città della Salute e della Scienza di Torino and Department of Medical Sciences of the University of Torino). All patient records were anonymized and deidentified prior to analysis. Histological samples of human CCM lesions were obtained from archived, formalin-fixed, paraffin-embedded surgically resected CCM specimens retrieved from the Department of Anatomy and Diagnostic Histopathology at the "Città della Salute e della Scienza" University Hospital, Turin, Italy. At the time of neurosurgery, an informed consent was asked by neurosurgeons to patients (or legal representatives) for scientific use of residual materials according to Institutional Rules defined by the Ethical Committee of the "Città della Salute e della Scienza" University Hospital, Turin. Only archived specimens with confirmed diagnosis of CCM by both neuroradiological and histopathological analyses were included in the study. Most of the selected CCM specimens were linked to patients carrying multiple CCM lesions, which are considered a marker of hereditary CCM, suggesting that they could represent the familial form of the disease. However, whereas some specimens derived from carriers of a single CCM lesion, which might be suggestive of a sporadic case, neither documented family history information nor genetic data were available from most of the corresponding medical records. Histological serial sections (3 µm thick) of selected paraffin-embedded CCM specimens were prepared and routinely stained with hematoxylin and eosin (H&E). Two pathologists (A.P. and P.C.) independently reviewed the H&E-stained slides, whereas additional sections, collected on superfrost plus slides, were used for immunohistochemical analysis. Immunohistochemical reactions were performed referring to the following protocol: briefly, histological sections were deparraffinized, rehydrated, and subjected to a 30-min cycle at boiling temperature in citrate buffer (pH 6.0) for antigen

retrieval. Endogenous peroxidase activity was blocked by a 7-min incubation with H_2O_2 solution RPE 6%. Thereafter, the sections were incubated for 45 min with guinea pig monoclonal anti-p62 primary antibody (diluted 1:300, Progen Biotechnik), followed by incubation with an HRP-labeled polymer conjugated secondary antibody (1:800, Santa Cruz Biotechnology) for 30 min at RT. Labeling was then visualized by a 5- to 10-min incubation with 3,3' diaminobenzidine + H_2O_2 substrate chromogen which results in a brown-colored precipitate at antigen site. The sections were subsequently counterstained with hematoxylin. Immunohistochemical variables were scored by evaluating the percentage of stained perinuclear regions at a 40x magnification in endothelial lumens.

Immunofluorescence

Cells, transfected or treated as described, were washed with phosphate-buffered saline (PBS) and fixed with 4% formaldehyde for 10 min at room temperature. After washing three times with PBS, cells were permeabilized with 0.1% Triton X-100 in PBS (PBS-T) at room temperature for 10 min and blocked with PBS-T containing 5% BSA at room temperature for 1 h. Cells were incubated with primary antibody in PBS-T containing 5% BSA overnight at 4°C, washed three times with PBS, and then incubated with appropriate isotype-matched, AlexaFluor-conjugated secondary antibodies (Life Technologies) at room temperature for 1 h. Digital images were acquired with confocal microscope (Zeiss LSM510) using a 63 x 1.4 NA Plan-Apochromat oil-immersion objective. Acquired images were then analyzed by using open source software Fiji.

Immunostaining for fluorescence microscopy of brain sections and retinas

All animal procedures were performed in accordance with the Institutional Animal Care and Use Committee (IACUC), in compliance with the guidelines established in the Principles of Laboratory Animal Care (directive 86/609/EEC) and approved by the Italian Ministry of Health. Brains and eyes from mice pups were fixed in 3% paraformaldehyde immediately after dissection, and fixation was continued overnight at 4°C. The retinas were dissected from the eyes just before staining as the whole mount. Fixed brains were embedded in 4% low-melting-point agarose and sectioned along the sagittal axis (150 µm) using a vibratome (1000 Plus, The Vibratome Company, St. Louis, MO, USA). Brain sections and retinas (as whole mount) were stained as floating samples in 12-well and 96-well plates, respectively. They were blocked overnight at 4°C in 1% fish-skin gelatin with 0.5% Triton X-100 and 5% donkey serum in phosphate-buffered saline (PBS) containing 0.01% thimerosal. The samples were incubated overnight at 4°C with the primary antibodies diluted in 1% fish-skin gelatin with 0.25% Triton X-100 in PBS containing 0.01% thimerosal. Following washing with 0.1% Triton X-100 in PBS, the secondary antibodies were added for 4 h at room temperature in 1% fish-skin gelatin with 0.25%

Triton X-100 in PBS containing 0.01% thimerosal. The incubation with DAPI was in PBS for 4 h, which was followed by several washes in PBS, post-fixation with 3% paraformaldehyde for 5 min at room temperature, and further washes in PBS. The brain sections were mounted in Vectashield with DAPI, and the coverslips fixed with nail varnish; the retinas were mounted in Prolong gold with DAPI.

CCM3-ECKO mice

CCM3-*flox/flox* mice were bred with *Cdh5(PAC)-CreERT2* mice for Tamoxifen-inducible endothelial cell-specific expression of Cre recombinase and *CCM3* gene recombination.

CCM3-flox/flox mice: these mice were generated at Taconic- Artemis (Koeln, Germany) on a C57BL/6N background according to the knock-in procedures. In this case, two P-lox sequences were inserted that flank exons 4 and 5 of the murine *CCM3* gene. P-lox sites can be targeted by the Cre recombinase enzyme, which induces recombination and subsequent excision of the nucleotides inserted between P-lox sequences. These mice have been used to control in a time-dependent manner for the deletion of *CCM3* gene.

Cdh5(PAC)-CreERT2 mice175: these mice have been kindly donated by Dr. R.H. Adams, (University of Munster, Munster, Germany) and present the CreERT2 gene under the VE-cadherin (Cdh5) promoter. Since VE-cadherin is an endothelial-specific gene, the expression of CreERT2 is confined to the endothelial district. CreERT2 gene expresses a fusion protein in which Cre recombinase has been fused together with the regulatory domain of the estrogen receptor. This domain is able to retain Cre recombinase into the cytoplasm of ECs in resting conditions. Only after stimulation with estrogen or an analog such as Tamoxifen CreERT2, fusion protein can dimerize and translocate to the nucleus where it can act on P-lox sites to drive homologous recombination. This model allows the operator to induce Cre recombinase expression in an endothelial-specific fashion just by Tamoxifen administration.

mRFP-GFP-LC3 detection

For autophagic flux measurements, cells cultured on 24-mm glass coverslips were transfected with the mRFP-GFP-LC3 tandem construct. After 24 h of expression, cells were placed in an open Leyden chamber on a 37°C thermostated stage. The quantitative analysis of the autophagic flux was performed on a Nikon LiveScan Swept Field Confocal Microscope (*SFC*) Eclipse *Ti* with a 60x magnification and equipped with NIS-Elements microscope imaging software (Nikon Instruments). For each condition, the colocalization of the red and green signals was determined by manual counting of fluorescent puncta in at least 20 independent visual fields.

ROS measurements using mt-HyPer probe

For mitochondrial H_2O_2 levels measurements, KRIT1 KO and KRIT1 KO re-expressing KRIT1 cells were cultured on 24 mm glass coverslips and transfected with the H_2O_2 sensor pHyPer-dMito (mt-HyPer). After 24 h of expression, cells were maintained in Krebs-Ringer buffer (KRB: 135 mM NaCl, 5 mM KCl, 1 mM $MgSO_4$, 0.4 mM KH_2PO_4, 5.5 mM glucose, 20 mM HEPES, pH 7.4), supplemented with 1 mM $CaCl_2$, and placed in an open Leyden chamber on a 37°C thermostated stage. 494/406 nm excitation filters and a 500-nm long-pass beam splitter were used, and an image pair was obtained in every 200 ms. The fluorescence data collected were expressed as emission ratios. The experiments were performed on Cell^R multiple wavelength high-resolution fluorescence microscopy system.

Soluble/Insoluble fraction

Total cellular proteins were separated into detergent-soluble and detergent-insoluble fractions. For detergent-soluble fraction, cells were lysed with a 1% Triton X-100 buffer (50 mM Tris pH 8.0, 150 mM NaCl, 1 mM EDTA, 10% glycerol, 1% Triton X-100, protease, and phosphates inhibitor cocktail). After 30 min on ice, lysates were centrifuged for 15 min at 12,000 g at 4°C and supernatant was collected as detergent-soluble fraction. The pellet was solubilized in the same buffer with addition of 1% SDS for 10 min at RT and, after centrifugation at 12,000 g for 15 min, the supernatant was collected as detergent-insoluble fraction. The detergent-soluble (10 µg) and detergent-insoluble (5 µg) fractions were subjected to immunoblot analysis. GAPDH and Lamin A/C were used as controls of the detergent-soluble and detergent-insoluble fractions, respectively.

Real-time PCR

Total RNA was extracted with TRIzol® Reagent (Invitrogen, Carlsbad, CA, USA). RNAs were purified with RNeasy Mini Kit (Qiagen GmbH, Hilden, Germany), and DNase digestion was performed with RNase-Free DNase Set (Qiagen). The RNA quality and concentration were measured using the NanoDrop™ ND-1000 (Thermo Scientific). For the first-strand cDNA synthesis, 1,000 ng of total RNA of each sample was reverse-transcribed with M-MLV Reverse Transcriptase (Invitrogen), following the manufacturer's protocol. Human primers were selected for each target gene with Primer 3 software. Real-time PCRs were carried out using the designed primers at a concentration of 300 nM and FastStart SYBR Green Master (Roche Diagnostics, Mannheim, Germany) on a Rotor-Gene 3000 (Corbett Research, Sydney, Australia). Thermal cycling conditions were as follows: 10 min denaturation at 95°C, followed by 40 cycles of denaturation for 10 s at 95°C; annealing for 20 s at 60°C; and elongation for 30 s at 72°C. Values were normalized to the expression of the glyceraldehyde-3-phosphate dehydrogenase

(GAPDH) and glucuronidase beta (GUSB) internal references, whose abundance did not change under our experimental conditions.

Cell proliferation assay

Cell proliferation assays were performed using a colorimetric method based on crystal violet staining. Cells, seeded at a density of n cells per well in 12-well plates, are left untreated or treated with Rapamycin (500 nM) or Torin1 (100 nM) in complete medium at 37°C for different time periods. Starting from the following day (day 1), 1 set of wells (at days 2, 3, 4) was washed with PBS, fixed for 10 min at room temperature in 4% formaldehyde, and then left in PBS at 4°C. The last day, all the wells were washed with PBS and then stained with crystal violet for 20 min. Excess dye was removed by three washes with PBS, and plates were allowed to air dry. After solubilization with 10% acetic acid solution, the absorbance was read at 595 nm with a microplate reader (SPECTROstar Nano-BMG Labtech).

Aggresome detection

The ProteoStat Aggresome Detection Kit (Enzo Life Sciences) was used according to the manufacturer's instructions. The kit provides a 488-nm excitable red fluorescent molecular rotor dye for the specific detection of aggregated proteins and aggresome-like inclusion bodies in fixed and permeabilized samples.

Tube formation assay

HUVECs (2×10^5 cells) transfected with scrambled siRNA or *ATG7* siRNA were seeded onto 6-cm culture dishes coated with BD Matrigel^{TM} Matrix (Becton-Dickinson) and incubated for 6 h at 37°C. After that, the formation of capillary-like structures was stained with calcein (Life Technologies) for 20 min at 37°C and then observed using an Axiovert 200M Carl Zeiss fluorescence microscope (20x objective); phase-contrast images were scanned with Leica DM IL LED, using a 4x objective.

Endothelial cell migration assay

Endothelial cell migration was detected by Transwell chamber assay (Corning). Briefly, the medium containing a 5% FBS was added to the lower chambers, and then, cells (HUVEC or lung endothelial cells) were suspended in 100 µl of serum-free medium and seeded onto the upper chambers. After incubation at 37°C for 8 h, the migrated cells were fixed with 4% paraformaldehyde, stained with the nuclear marker DAPI, and then photographed and automatically counted using a custom-made Cell Profiler pipeline. The images have been taken with a Carl Zeiss Axiovert 200 M using a 20x magnification.

Statistical analysis

Statistical analyses were performed using an unpaired two-tailed *t*-test (two groups) or one-way ANOVA with Bonferroni correction (for groups of three or more). For grouped analyses, multiple unpaired *t*-test with correction for multiple comparisons using the Holm-Sidak method was performed. Normal distribution of data was assessed by applying a D'Agostino & Pearson omnibus normality test. *F*-test was used to compare variances between groups. A *P*-value < 0.05 was considered significant. All data are reported as mean ± s.e.m. Exact *P*-values are indicated in the figure legends.

From: Marchi S, Corricelli M, Trapani E, Bravi L, Pittaro A, Delle Monache S, Ferroni L, Patergnani S, Missiroli S, Goitre L, Trabalzini L, Rimessi A, Giorgi C, Zavan B, Cassoni P, Dejana E, Retta SF, Pinton P (2015) *Defective autophagy is a key feature of cerebral cavernous malformations.* EMBO Mol Med 7(11):1403-17.

(2) c-Src regulates intracellular Ca^{2+} homeostasis via IP3R3 phosphorylation

Introduction

1. c-Src, key modulator of signal transduction

Src was the first discovered and molecularly-defined proto-oncogene, and its protein product has been associated to protein kinase activity [84]. The discovery of the cellular proto-oncogene c-*Src* (or p60$^{c\text{-}src}$) was preceded by the identification of the viral Src (v-*src*), a transforming retroviral oncogene by Peyton Rous in 1911 [85]; [86]; [87]. The viral protein encoded by this oncogene, which corresponds to a truncated form of the cellular Src, is responsible for the cancer-inducing activity of the Rous sarcoma virus, a chicken tumor virus. Among metazoans Src is highly conserved, and the expression of its ortholog was also found in unicellular choanoflagellates.

The cellular proto-oncogene product c-Src is a 60 kDa cytoplasmic non-receptor protein tyrosine kinase, responsible for the transfer of the terminal phosphoryl group of Adenosine triphosphate (ATP) onto specific tyrosine residues within protein substrates. c-Src is activated through several signaling inputs via interaction with multiple cell surface receptors, including integrins, G-protein-coupled receptors, cytokines, growth factors, steroid hormone receptors, and immune cell receptors. Through its recruitment and subsequent activation by cell surface receptors, c-Src, as the other Src-family kinases (SFKs), is involved in multiple pathways that modulate the signal transduction within the cell, regulating critical processes as survival and cell death, cell growth and differentiation, adhesion between adjacent cells and to extracellular matrix, cell migration and invasion, angiogenesis, and synaptic plasticity and transmission [88]; [89]. c-Src-dependent functions are related to its subcellular localization, predominantly in the cytoplasm and, upon activation, at the cytoplasmic side of the plasma membrane [90]. It has been observed its association with focal adhesions, nuclear and endosomal membranes, mitochondria, and specialized secretory vesicles [91]; [92]; [93]; [94]; [95].

c-Src is considered the prototype for the Src-family kinases (SFKs) that, in humans, include 11 members [96]. Based on the overall homology between the different kinases, the SFKs can be divided in two subfamilies: Src-related SFKs that include c-Src, Fyn, Yes and Fgr, and the Lyn-related, Lyn, Blk, Hck and Lck. In addition, there are three further SFK-related kinases, Brk, Frk and Srm, which do not share noteworthy homology to c-Src nor Lyn sequences, do not have a myristoylation site and a regulatory C-terminal tyrosine, except Srm. Some of the SFKs, as c-Src, Fyn and Yes, are ubiquitously expressed in a wide range of cell types, whereas other SFKs display a specific and more limited pattern

of expression: Blk, Fgr, Hck, Lck, and Lyn are typically expressed in hematopoietic cells, Srm in keratinocytes, Frk mainly in bladder, brain, breast, colon, and lymphoid cells, while Brk in colon, prostate, and small intestine. Although each SFK has evolved to execute specific and unique functions in the network of the intracellular signalling, SFKs display a considerable redundancy in their functions.

1.1 c-Src structure

The structure and the distinct domains of c-Src kinase have been intensively studied and are known in detail. The 536 amino acids protein (in humans) contains a N-terminal region followed by the Unique domain, three modular Src homology (SH) domains, a catalytic domain, and a C-terminal regulatory tail (Fig. 14A). Unlike the Unique domain, all the other domains are strictly conserved within the different SFKs.

The amino-terminal region or SH4 domain contains a myristoylation site, which is conserved among the family members, and some SFKs, including Yes and Fyn, exhibit a further palmitoylation site [97]. Myristoylation, a permanent lipid modification that occurs on glycine residue at position 2 as the protein is translated, is essential for the anchorage into the lipid bilayer and seems to be critical for the biological activity, while palmitoylation is a reversible lipid modification affecting cystine residues. Additional electrostatic interactions, between the membrane negative charge and the positively charged residues within the N-terminus, get stable but reversible the insertion. Recent evidences suggest that further protein portions of lower affinity within the Unique and SH3 domains also contribute in directing c-Src membrane binding and subcellular localization [98].

The Unique domain is the most differing region within the SFKs. Many evidences suggest a role in providing a specific and likely different function to each SFK, as specific interactions or targeting at different subcellular compartments. Although its function remains undefined for most of SFKs, it is known to mediate Lck interaction with T cell coreceptors. This domain directs the myristoylation and palmitoylation at N-terminus and it has been observed that Hck Unique domain phosphorylation influences its catalytic activity.

SH3 domain mediates c-Src protein-protein interactions owing to its affinity with proline-rich motifs, related to the PXXP consensus, thus enabling substrate or adaptor recruitment [99]. Since SH3 domain is directly involved in the autoinhibitory intramolecular interactions, which held the molecule in the downregulated state, it plays an additional role in the modulation of c-Src catalytic activity. Indeed, mutations or deletions in c-Src SH3 domain or SH3 domain binding to substrates, by affecting the downregulatory effect of these interactions, increase its kinase activity and, in some cases, the transforming potential.

The SH2 domain mediates the interaction with phosphotyrosine-containing sequences in target proteins. Not only the tyrosine phosphorylation is strictly required for the interaction, but the phosphorylation itself and the surrounding sequences provide the specificity of this binding [100]. The binding with the tyrosine phosphate group is driven by a conserved arginine residue (175 in chicken, 178 in humans), exhibiting high affinity for the canonical sequence pTyr-Glu-Glu-Ile (pYEEI). Moreover, the intramolecular binding of the SH2 domain with p-Tyr527 (in chicken, p-Tyr530 in humans) in the C-terminus defines a SH2 pivotal negative regulatory role on the kinase activity. Although some mutations in the SH2 domain decrease the c-Src transformation competence, other mutations or deletions lead to upregulated kinase activity and provide transforming potential and probably alter the spectrum of c-Src interactions.

The catalytic or SH1 domain provides the enzymatic activity. It consists of a small N- and a large C-terminal lobe. The N-lobe contains a phosphate binding loop (P-loop or G-rich loop), where the phospho-transfer reaction occurs and a conserved glycine-rich sequence mediates the interaction with the γ-phosphate of ATP, and an α-helix (C-helix) that is critical for the intramolecular regulatory mechanism. Within the C-terminal lobe there is the catalytic loop and a kinase activation loop (A-loop). The A-loop, which is involved in ATP and substrate binding, contains a regulatory autophosphorylation site, Tyr416 (in chicken, Tyr419 in humans) that is crucial for the protein stabilization. When not phosphorylated, Tyr416 results inaccessible to the substrate and unavailable for the catalytic activity whereas, upon phosphorylation, it forms a salt bridge with a conserved arginine, leading to the stabilization of the active conformation and the full catalytic activity. Upstream of the A-loop is sited a highly conserved DFG (Aspartate-Phenylalanine-Glycine) motif.

Within the carboxy-terminal tail, the highly conserved Tyrosine in position 527 (in chicken, Tyr530 in humans) plays a critical regulatory role, as its phosphorylation leads to c-Src kinase activity downregulation [101]. Therefore, its substitution with phenylalanine determines a strong upregulation of c-Src catalytic activity, which is sufficient to convert the proto-oncogene to oncogene. Indeed, by preventing Tyr527 phosphorylation, this mutation leads to SH2 domain detachment, intramolecular interactions disruption and consequent increase of the kinase potential. Unlike Tyr416, Tyr527 is phosphorylated by other regulatory kinases.

1.2 c-Src regulation and dysregulation

In order to ensure c-Src-mediated fast cell responses, its kinase activity and substrate targeting are rigorously down-regulated in resting state and c-Src is transiently activated. c-Src catalytic activity is finely controlled by biochemical events like phosphorylation and protein-protein interactions. Structural studies have revealed that c-Src can switch between two different configurations: an open and fully active or a closed and catalytically

inactive conformation (Fig. 9) [102]. Although the molecular details of this activation may vary depending on the extracellular environment and the cell type, the general mechanism is conserved among the SFKs. This regulation involves both SH3 and SH2 domains-mediated intramolecular interactions and their association with additional molecules such as receptors, substrates, activators and inhibitors.
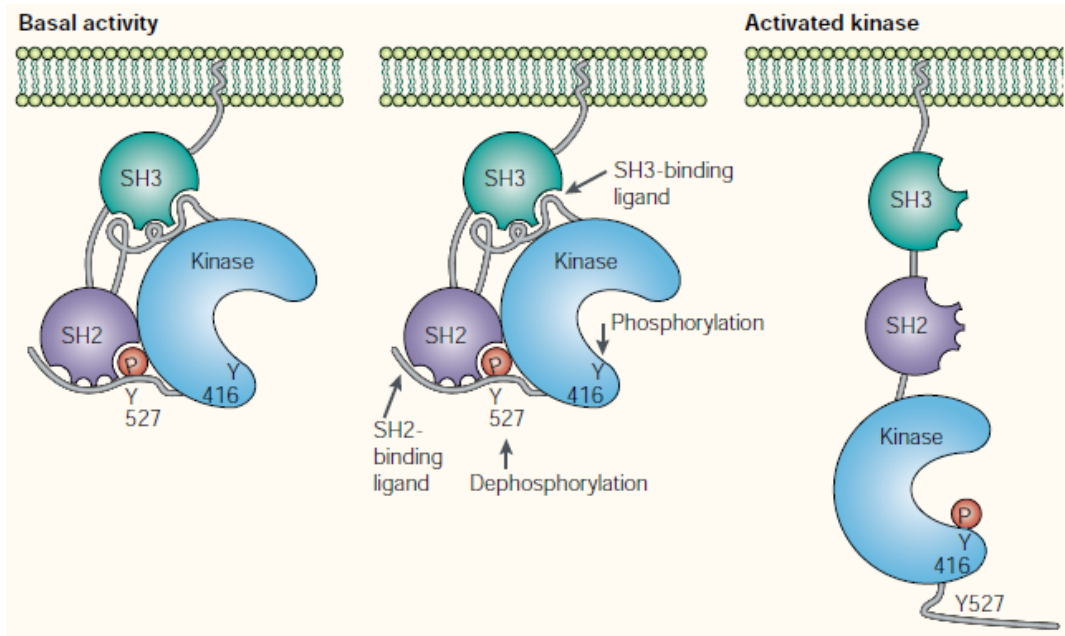
Figure 9 | Activation of c-Src. The left panel represents the inactive conformation of Src, in which Tyr527 (chicken c-Src) interacts with the SH2 domain, positioning the SH3 domain to interact with the linker between the SH2 and catalytic domains. The middle panel illustrates different mechanisms involved in the activation of Src, and the right panel represents the open or active conformation. From "The hunting of the Src" Martin, Nature Reviews, Molecular Cell Biology; 2(6):467-75 (2001).

In the inactive turned-out configuration, the intra-molecular interactions involve the C-terminal p-Tyr527 and the SH2 domain, and the SH3 domain with a PPII helix (type-II polyproline helix) formed by the linker connecting the SH2 and catalytic domains [103]; [102] (Fig. 9). Detailed characterization of SFKs molecular structures reveals that SH3 domain anchors to a non-canonical consensus sequence, whereas SH2 domain binds a consensus p-Tyr motif a quite different from the high affinity sequence experimentally established, but it renders stable the inactive conformation by making p-Tyr527 inaccessible to phosphatases. In particular, SH3 and SH2 domains push against to the N- and the C-lobe respectively, thus rendering the A-loop inaccessible to substrates and ATP, sequester the Tyr416, and the hydrogen bond between Glu310 in the αC-helix and Lys295 (in chicken, Lys298 in humans), required for Mg-ATP binding, is disrupted. In this way, the synergistic effects of two weak interactions cooperate to turn off c-Src kinase activity by stabilizing the inactive configuration [103].

From this fully closed inactive form, harboring a phosphorylated Tyr527 in the C-tail, an unphosphorylated Tyr416, and the intramolecular SH3/SH2 interactions, SFKs can be activated by dephosphorylation of Tyr527, disruption of the inhibitory intramolecular interactions, or autophosphorylation of Tyr416. Indeed, Tyr527 dephosphorylation, substitution with phenylalanine, or C-terminus deletion, and disruption of either SH2/C-tail or SH3/linker interactions by mutation or interaction with other proteins, are enough to induce c-Src activation. It is possible to switch into a partially active form, in which one or both the SH3/SH2 interactions are disrupted but Tyr416 is still not phosphorylated. Indeed, to reach the maximal kinase activity, the phosphorylation of Tyr416 is required, and prevails on the auto-inhibitory intramolecular interactions.

Dephosphorylation of p-Tyr527 at the C-terminus leads to SH2 domain release, which causes dramatic conformational change in the kinase domain, αC-helix is re-oriented towards the active site and the A-loop assumes an appropriate conformation that results in the formation of a hydrogen bond between Glu310 and Lys295, indispensable for the binding with ATP or interactors. The following autophosphorylation of Tyr416 stabilizes and locks the catalytic pocket into the completely active conformation and enables the substrate binding [104]. This phosphorylation is obtained via a trans-autophosphorylation likely mediated by other SFKs or further tyrosine kinases. Furthermore, the DFG motif can coordinate the interaction between Mg^{2+} and the phosphate group of ATP, and the P-loop assumes an open conformation, which enables the binding with ATP. Activation of c-Src via Tyr527 dephosphorylation is mediated by protein-tyrosine phosphatases. Currently several tyrosine phosphatases are known to be implicated in c-Src dephosphorylation of either the A-loop or C-terminus and, depending on the cell context, some of them can mediate both SFKs activation and inactivation. Receptor protein-tyrosine phosphatase alpha (PTP-α or RPTP-α) acts by displacing from the SH2 domain and subsequently dephosphorylating the C-terminal tyrosine [105]. In addition, PEP (proline-enriched tyrosine phosphatase), TCPTP (T cell protein tyrosine phosphatase), SHP1 (tandem SH2 domain-containing protein tyrosine phosphatase), and CD45 (transmembrane receptor-like tyrosine phosphatase) dephosphorylate the tyrosine located in both the C-terminal and A-loop.

c-Src activation by SH3/SH2 domain displacement occurs also upon the recognition of ligand phosphotyrosine or proline-rich motifs, resulting in the disruption of the inhibitory intramolecular bindings, which are weaker compared to the intermolecular interactions. In fact, the SH3 intramolecular target region adopts a PPII helical conformation instead to the canonical PXXP motif, and at the +3 position near the p-Tyr527 there is a glycine rather than a favorite isoleucine. Numerous interactor molecules have been identified, acting via SH2 domain, as phosphorylated forms of Cas, FAK, paxillin, EGFR, CSF-1 and PDGF, or via SH3 domain, such as Shc, PI3K, Tks5, and Arhgef5.

Another mechanism responsible for c-Src activation is the direct phosphorylation of Tyr416 by other protein kinases.

When the cell response is concluded, c-Src is rapidly inactivated or degraded. The inactivation is triggered by catalytic inhibitors, including C-terminal Src kinase (Csk), the main and well-known kinase responsible of c-Src inactivation [106], and CSK-homologous kinase (Chk) [107], through the high affinity phosphorylation of Tyr527, which force the molecule into the closed structure by inducing the two consequential intramolecular interactions. Both Csk and Chk contain SH2 and SH3 domains and a catalytic domain. While Csk is ubiquitously expressed in mammalian cells, Chk expression is restricted to breast, testes, hematopoietic cells, and neurons. Furthermore, the c-Src catalytic inhibitors include also the protein tyrosine phosphatases acting on Tyr416 dephosphorylation within active SFKs. Additionally, non-catalytic inhibitors are responsible for c-Src inactivation by direct binding. Among these inhibitors, Chk acts as both catalytic and non-catalytic factor. Non-catalytic inhibitors include WASP, caveolin, and RACK1, which provide SFKs downregulation in specific subcellular locations [107].

c-Src irreversible degradation occurs via the ubiquitin-proteasome machinery, that marks and drives to degradation exclusively the highly active kinases [108], and the specificity of polyubiquitylation is provided by the E3 ligases. This regulation mechanism is likely mediated by Cullin-5-dependent ubiquitylation, which acts only on active c-Src harboring p-Tyr416. c-Src activity is also controlled by Cdk5, a proline-directed protein kinase, through phosphorylation of Ser75 in the N-terminal sequence of c-Src. Furthermore, c-Cbl has been identified as a E3 ligase responsible for c-Src ubiquitylation and degradation.

The pleiotropic involvement in the regulation of critical cellular functions underlines the importance of a complex regulatory system for controlling the potentially dangerous effects of an inappropriate or uncontrolled SFKs activity. Their activity dysregulation plays a causative role in a wide range of diseases, including cancer, neurodegenerative diseases, epilepsy, and HIV/AIDS. c-Src kinase activity results elevated in several types of human cancer, including breast, colon, pancreatic, brain, lung, ovarian, and gastric cancer [109], as direct consequence of both increased protein expression and augmented specific activity. It has been strongly implicated in cancer growth, development, progression, and metastasis and, interestingly, c-Src levels concomitantly increase with the stage of disease. In this context, c-Src catalytic activity may be enhanced by direct or indirect interaction with receptor tyrosine kinases, including fibroblast growth factor receptor (FGFR), epidermal growth factor receptor (EGFR), platelet derived growth factor receptor (PDGFR), and colony stimulating factor-1 receptor (CSF-1R). An alternative way for c-Src hyper activation is related to decrease of Csk protein levels or activity, or higher activity of those phosphatases responsible for the Tyr527 dephosphorylation. Upon its upregulation, in cancer cells many c-Src substrates are in turn phosphorylated, and most

of them are involved in pathways leading to tumor development and metastasis [88]. Thus, these dramatic alterations in signal transduction affect multiple hallmarks of the metastatic phenotype as cell adhesion, apoptosis, angiogenesis, tumor growth and invasiveness. Counteract any of these events would potentially reduce the tumor growth and metastasis. Therefore, c-Src becomes an excellent target for the development of therapeutic drugs.

2. Ca^{2+} as intracellular signal

Eukaryotic cells respond to a wide range of extracellular signals, including growth factors, hormones, neurotransmitters and cell-cell interactions, by conveying them in intracellular responses. Frequently those inputs, through the interaction with receptors harboring intrinsic enzymatic activity, acting as ion channels or coupled to intracellular effectors via G proteins, lead to cytoplasmic calcium (Ca^{2+}) concentration ($[Ca^{2+}]_{cyt}$) increase with defined amplitude and kinetics [110]; [111]. The versatility of Ca^{2+} as intracellular messenger capable of regulating multiple processes depends mainly on the spatiotemporal complexity of Ca^{2+} signals, and the Ca^{2+} signalling toolkit is continuously remodeled in both health and disease. Single cell measurements have revealed the actual complexity of spatial and temporal Ca^{2+} dynamics, which can occur as repetitive spikes (Ca^{2+} oscillations) [112] or localized increases, confined or gradually propagate within the cells (Ca^{2+} waves) [113]; [114]. While highly localized Ca^{2+} spikes function to control rapid responses, repetitive global Ca^{2+} transients or Ca^{2+} waves mediate slower responses. Across the plasma membrane there is an electrochemical gradient of 70-90 mV, with a negative charge on the cytoplasmic side of the membrane, and the $[Ca^{2+}]_{cyt}$ results less than one-ten thousandth compared to the extracellular environment and one- to ten thousand folds less than intracellular stores, as endoplasmic reticulum (ER) and secretory granules.

Throughout the *on reaction*, extracellular stimuli lead to intracellular Ca^{2+} increase through the external Ca^{2+} entry and the release from the intracellular stores, ER and Golgi. Ca^{2+} is predominantly bound to buffers and to those effectors involved in diverse pathways. During a typical Ca^{2+} transient, the generation of Ca^{2+} signal is counteracted by the switching off mechanisms, in order to preserve the resting levels of Ca^{2+} and ensure the refilling of the internal stores. Thus, during the *off reactions*, Ca^{2+} has to be removed from the cytoplasm via Ca^{2+} exchangers and pumps: Na^+/Ca^{2+} exchanger (NCX) and plasma membrane Ca^{2+}-ATPase (PMCA) are responsible for its extrusion to the extracellular milieu, while the sarco/endoplasmic reticulum Ca^{2+}-ATPase (SERCA) takes Ca^{2+} back into the ER. In addition, mitochondrial Ca^{2+} uptake via the uniporter contributes to the ion sequestration, followed by a slow release back into the cytosol. Since cell survival is

related to Ca^{2+} homeostasis, Ca^{2+} fluxes during the off reactions exactly have to match those of the on reaction.

In order to keep Ca^{2+} levels low in resting conditions, its intracellular distribution is finely regulated. Therefore, controlled variations of $[Ca^{2+}]$ permit to use it as a messenger in the context of multiple cellular events, such as gene expression, cell division, proliferation, cell death, motility, membrane trafficking, secretion, development, immune responses, learning and memory, muscle contraction, membrane excitability, and synaptic transmission.

An increase in the cytoplasmic $[Ca^{2+}]$ relies on the activity of channels that sit on the plasma membrane and internal stores, ER and Golgi apparatus.

Ca^{2+} entry from the external milieu occurs via several plasma membrane channels in response to a wide range of stimuli, such as extracellular agonists, toxic stimuli, membrane depolarization, and stretch, and is driven by the electrochemical gradient existing between the two sides of the plasma membrane. These Ca^{2+}-entry channels display different features and their opening is triggered by different external signals. The voltage-operated channels (VOCs), typical of excitable cells, produce rapid Ca^{2+} fluxes involved in fast cellular events as muscle contraction or exocytosis at synaptic endings. Other channels open in response to different external stimuli and include store-operated channels (SOCs), receptor-operated channels (ROCs), for example the NMDA receptor that responds to glutamate, second-messenger-operated channels (SMOCs) that respond to internal messengers, as the cyclic-nucleotide-gated channels located in sensory systems and the arachidonic-acid-sensitive channel. G protein-operated-calcium channels (GOCCs) execute most of the cell responses to hormones, neurotransmitters, autocrine and paracrine factors. G protein-coupled receptors include more than 1000 distinct members, all characterized by a conserved primary structure and called seven transmembrane spanning domain receptors, because of the seven stretches of 20-25 hydrophobic amino acid residues spanning the plasma membrane. Upon agonist interaction, GOCCs undergo a conformational change that drives the coupling to G proteins, heterotrimeric guanine regulatory proteins. The agonist-G protein-coupled receptor complex induces the heterotrimeric G protein activation by promoting the exchange between GDP and GTP. A fine modulation of these events ensures to limit the amplitude and the time extent of the stimulus' effect, which generally reaches a milliseconds or minutes range. For example, saturating concentrations of the agonist produce their desensitization and the following ending of the response.

Ca^{2+} release from internal stores is modulated by Ca^{2+} itself or by other messengers, such as Inositol 1,4,5-trisphosphate (IP3), cyclic ADP ribose (cADPr), nicotinic acid adenine dinucleotide phosphate (NAADP), and sphingosine-1-phosphate. Among the intracellular Ca^{2+} release mechanisms, the main are represented by Inositol 1,4,5-trisphosphate

receptor (IP3R) and ryanodine receptor (RYR). IP3R is the most ubiquitous and sits on the endoplasmic reticulum membrane. It is activated by the binding of the second messenger IP3 and is modulated by Ca^{2+} and IP3 itself. Cytosol low and higher concentrations sensitize and inhibit the receptor, respectively, and probably also Ca^{2+} on the luminal side sensitizes the receptor to IP3. The RYR family includes RYR1, found in skeletal muscle and certain neurons (e.g. Purkinje cells), RYR2 in cardiac muscle, brain and some other cells, and RYR3 typical of smooth muscle, brain and other cells [115]; [116]. As Ca^{2+} is generally the physiological ligand for the channel, RYR is considered a *Calcium-Induced Calcium Release* receptor-Ca^{2+} channel, somehow differently to IP3R, which is sensitized to IP3 by Ca^{2+} but strictly requires always IP3. In addition, some RYR forms can be affected by small water-soluble molecules acting as regulatory ligands. Cyclic adenosine diphosphate ribose (cADPr), by increasing RYR sensitivity to Ca^{2+}, increases its opening probability.

Off reaction is mediated by the plasma-membrane Ca^{2+}-ATPase (PMCA), the Na^+/Ca^{2+} exchanger (NCX), SERCA (sarco/endoplasmic reticulum Ca^{2+}-ATPase), and the mitochondrial Ca^{2+} uniporter (MCU). PMCA and SERCA function to maintain basal Ca^{2+} levels and in response to modest Ca^{2+} elevations, since they display high affinities but lower transport rates. By contrast, NCX and MCU, with greater transport rates, can limit Ca^{2+} transient over a wider dynamic range.

Ca^{2+}-ATPases are a family of proteins that include the SERCA and the PMCA, co-expressed by most eukaryotic cells, in a tissue-specific and differentiation stage-specific manner. PMCA, plasma membrane Ca^{2+} pumps, act in Ca^{2+} transport between the intracellular and the extracellular environment. In Mammals, there are four PMCA genes and more than four protein products, thanks to the alternative splicing, distributed in a tissue- and cells-specific manner. In addition to their typical role in basal Ca^{2+} handling, they seem to be involved in more specialized functions [117]. SERCA are Ca^{2+} pumps responsible for taking Ca^{2+} back from the cytosol to the cellular stores sarcoplasmic reticulum, endoplasmic reticulum, and calciosomes. This is an active transport that requires ATP and enables the translocation of the two Ca^{2+} bound to the enzyme from a high affinity site to a low affinity site, and the following release into the lumen [118]. There are three known SERCA genes: SERCA 1, exclusively expressed in fast twitch skeletal muscle, SERCA 2 in slow-twitch skeletal muscle, cardiac muscle, smooth muscle and non-muscle tissues, and SERCA 3, with widespread tissue distribution.

Na^+/Ca^{2+} exchangers are responsible for the Ca^{2+} export from the cytosol against its concentration gradient, by taking advantage of the energy residing in the Na+ (K+) gradient across the plasma membrane [119]; [120]. Two types of Na^+/Ca^{2+} exchangers have been identified: the prototype, located on plasma membrane of cardiac and numerous other cells (NCX), which exchanges three Na^+ for one Ca^{2+}, and an exchanger,

initially found in the outer segment of retinal rods and cones (NCKX), which exchanges four Na^+ with one Ca^{2+} and one K^+.

Ca^{2+} uptake by mitochondria, which is related to several cell functions including ATP production and cell death, is carried out by outer mitochondrial membrane Ca^{2+} channels (VDAC) and mitochondrial inner membrane Ca^{2+} uniporter (MCU). MCU is a highly selective ion channel and reaches saturation only at more than physiological $[Ca^{2+}]_{cyt}$. MCU allows the Ca^{2+} transport across the inner mitochondrial membrane by taking advantage of the significant driving force related to the negative transmembrane potential [121]. MCU is regulated biphasically by Ca^{2+}, as $[Ca^{2+}]_{cyt}$ increase can both activate or inactivate mitochondrial Ca^{2+} uptake, and is principally inhibited by Rutenium Red and its related compound RuR360, clonazepam and CGP37157.

2.1 Tools for intracellular Ca^{2+} measurements

To measure Ca^{2+} homeostasis at the subcellular level the Ca^{2+}-sensitive photoprotein aequorin is currently used. It is targeted to defined cytoplasmic regions, as the bulk cytosol and the subplasmalemmal rim, or to intracellular organelles, as mitochondria, endo- and sarcoplasmic reticulum, Golgi apparatus, and nucleus.

Aequorin is a Ca^{2+}-sensitive photoprotein of a coelenterate, isolated from the jellyfish *Aequorea Victoria.* The protein, consisting of a 21 kDa apoprotein and a hydrophobic prosthetic group of ~400 Da, coelenterazine, harbors 3 high affinity Ca^{2+} binding sites. After Ca^{2+} binding, the coelenterazine is oxidized to coelenteramide, with a concomitant release of carbon dioxide and emission of one photon. This irreversible reaction takes place only when coelenterazine and the apoprotein are associated.

The existence of a definite relationship between the rate of photon emission and the free Ca^{2+} concentration makes aequorin an ideal calcium indicator. The rate of this reaction depends on the $[Ca^{2+}]$ surrounding the photoprotein: at $[Ca^{2+}]$ between 10^{-7} and 10^{-5} M (living cells cytoplasmic $[Ca^{2+}]$), exists a direct relationship between $[Ca^{2+}]$ and the fractional rate of consumption of the photoprotein. Figure 10 shows the curve of aequorin Ca^{2+} response, at physiological conditions of pH, temperature, and ionic strength. It is apparent that the fractional rate of aequorin consumption, expressed as the ratio between the emission of light at a defined Ca^{2+} concentration (L) and the maximal rate of the light emission at saturating $[Ca^{2+}]$ (Lmax), is proportional to the 2nd-3rd power of $[Ca^{2+}]$. Thus, if the total light emitted throughout an experiment and discharged at the end of the measurement is collected, it is possible to estimate Lmax and then obtain the $[Ca^{2+}]$ to which the photoprotein is exposed in each moment.
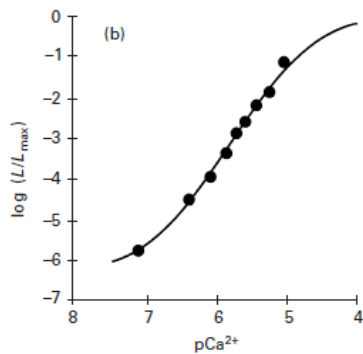
Figure 10 | The Ca^{2+} concentration response curve of recombinant aequorin. The fractional rate of aequorin consumption is expressed as the ratio between the emission of light at a defined Ca^{2+} concentration (L) and the maximal rate of light emission at a saturating Ca^{2+} concentration (L max).
From "Recombinant aequorin and green fluorescent protein as valuable tools in the study of cell signalling" Chiesa et al., The Biochemical journal; 355(Pt 1):1-12 (2001).

Aequorin photon emission can be also generated by lanthanides, displaying high affinity for the photoprotein, and by Sr^{2+} but with weaker affinity, about 100 folds lower than Ca^{2+}. Although K^{+} or Mg^{2+}, the main cations of the intracellular environment, do not affect aequorin luminescence, both ions are competitive inhibitors of Ca^{2+}, while pH affects aequorin luminescence at values below 7. For these reasons, aequorin experiments are actually performed at controlled conditions of pH and ionic concentrations, notably of Mg^{2+}.

In vitro, it is possible to obtain an active aequorin by incubating the apoprotein with coelenterazine in the presence of oxygen and 2-mercaptoethanol, and in living cells its reconstitution is reached through aequorin recombinant expression and following addition of coelenterazine to the medium. Indeed, coelenterazine, thanks to its hydrophobicity, can easily permeate cell membranes of numerous cell types [122].

At first, aequorin was employed to measure cytoplasmic [Ca^{2+}] in living cells after microinjection, especially in a limited number of giant cells, as invertebrate muscle cells. Because of the time-consuming and traumatic procedure of microinjection, this use remained strictly limited. Only after molecular biology advances, aequorin cDNA cloning [123] and its recombinant expression led to an extensive use of the protein as Ca^{2+} indicator in living cells. Upon cDNA transfection, a wide range of cells (bacteria, yeast, plants and mammalian) can express the aequorin. Interestingly, it is also possible to express recombinant aequorin in definite subcellular locations, due to specific targeting sequencing. The targeting strategies adopted were three: inclusion of a minimal targeting signal sequence, fusion with the cDNA of a compartment resident protein, or addition of sequences encoding for polypeptides that bind to endogenous proteins. All targeted aequorins encompass modifications at the N-terminal, since manipulations in this region have been shown to not alter the photoprotein chemiluminescence properties and its Ca^{2+} affinity. Moreover, C-terminal modifications abolish luminescence or considerably increase Ca^{2+} independent photon emission [124]. Indeed, Watkins and Campbell [125] demonstrated that the proline at the C-terminus of aequorin is strictly required for the long-term stability of the bound coelenterazine.

- *Aequorin targeted to cytoplasm (cytAEQ)*

An unmodified aequorin cDNA encoded protein has a cytosolic distribution in mammalian cells, and spreads into the nucleus thanks to its small size. The sequence was modified only by the addition of the epitope tag HA1 [126].

- *Aequorin targeted to mitochondria (mtAEQ)*

The mtAEQ is used for $[Ca^{2+}]$ measurements within the mitochondrial matrix. The mitochondrial localization is provided by the targeting presequence of subunit VIII of human cytochrome *c* oxidase, which is fused to the aequorin cDNA [127]. Because of the cooperativity between the three Ca^{2+}-binding sites of aequorin, the point mutation Asp119Ala [128] produces a mutated aequorin useful for $[Ca^{2+}]$ measurements in the range of 10-500 µM (mtAEQmut).

- *Aequorin targeted to Endoplasmic reticulum (erAEQ)*

The erAEQ contains the leader sequence (L), the VDJ and CH1 domains of an Igg2b heavy chain at the aequorin N-terminus. Specifically, ER localization relies to the CH1 domain ability to interact with the luminal ER protein BiP [129].

As intracellular Ca^{2+} sensor, aequorin displays many advantages but also some disadvantages. At first, all the recombinantly expressed aequorins have a selective and specific distribution within the cell. Additionally, low intrinsic luminescence of the cells and the steepness of the aequorin Ca^{2+} response provide a high signal-to-noise ratio; therefore, it is possible to detect minimal changes in $[Ca^{2+}]$. Aequorin is characterized by low Ca^{2+} buffering effect since, besides aequorin binding to Ca^{2+} may influence intracellular Ca^{2+} homeostasis, this effect is less relevant than for fluorescent indicators. Indeed, aequorin is used at concentration 2-3 orders of magnitude lower than fluorescent dyes, generally < 0.1 µM for the recombinantly expressed photoprotein. Aequorin, in contrast to most fluorescent indicators, can be used for measurements of $[Ca^{2+}]$ ranging from 0.5 µM to 10 µM. In addition, it is possible to reduce its sensitivity through point-mutations in the Ca^{2+}-binding sites [128], by modifying the prosthetic groups or using surrogate cations (such as Sr^{2+}), allowing Ca^{2+} measurements in intracellular compartments characterized by high $[Ca^{2+}]$, as ER lumen. Notably, it is also possible to co-express aequorin with other proteins of interest, which is useful for studying a protein role on Ca^{2+} homeostasis. However, if the $[Ca^{2+}]$ increase is not homogeneous, the average rise estimate will be based on the highest values, which may not reflect the real values. In contrast to fluorescent dyes, where photobleaching occurs not before the emission of up to 10^4 photons by a single molecule, an aequorin molecule emits just one photon; considering that only a limited portion of the total cells (ranging from 10^{-7} to 10^{-2}) is actual responsible for the photon emission each second, its use is ideal for population studies. Because of aequorin low light emission, for single cell imaging is preferred to use fluorescent dyes, which provide higher spatial and temporal resolution.

2.2 Luminescence detection

The aequorin detection system derives from the one described by Cobbold and Lee [130]. A low noise photomultiplier is placed in close proximity (2-3 mm) of the aequorin expressing cells, laying on a 13-mm diameter coverslip that is put on the cell chamber, on the top of a hollow cylinder, and is closed with a coverslip. Cells are continuously perfused via a peristaltic pump with a minimum volume (about 200 µl) of medium, kept at 37°C by a water jacket. The photomultiplier is kept in a dark box, cooled at 4°C and protected from light by a shutter during manipulations on the cell chamber. The shutter is opened only during measurements, and the chamber with cells sits in close proximity of the photomultiplier. The output of the amplifier-discriminator is captured by the photon counter C8855-01 connected via a USB cable to a workstation and recorded by the sample software (Hamamatsu Photonics) for the analysis. It has been developed an algorithm to calibrate the crude luminescent signal in terms of $[Ca^{2+}]$, based on the instant rate of photon emission and the total number of photons emitted by the aequorin. To exactly evaluate the total number of photons emitted, at the end of each experiment the cells are perfused with a hyposmotic medium containing 10 mM $CaCl_2$ and a detergent (100 µM digitonin or 0,1% Triton X-100), leading to cell lysis and residue aequorin discharging.
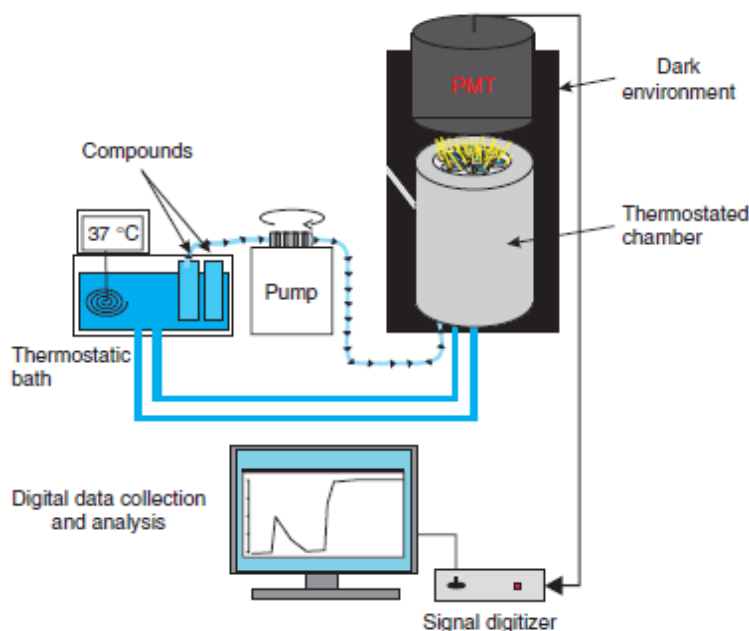

Figure 11 | Schematic representation of the typical organization of a custom-made aequorin recording system for whole-cell population measurements. From "Subcellular calcium measurements in mammalian cells using jellyfish photoprotein aequorin-based probes" Bonora et al., Nature protocols; 8(11):2105-18 (2013).

3. Inositol 1,4,5-trisphosphate receptors (IP3Rs)

Modulation of cytoplasmic free Ca^{2+} levels is the most versatile cellular signalling device for the regulation of several and markedly different events. Endoplasmic (ER) and sarcoplasmic (SR) reticulum represent the main Ca^{2+} storage compartment within the eukaryotic cells, strictly involved in the intracellular signal transduction and the maintenance of Ca^{2+} homeostasis. However, the ER Ca^{2+} contribution is highly variable among the different cell types, since each cell displays distinct functions, morphologies, ion channel density, and ER contents. Besides its role in controlling Ca^{2+} fluxes, ER supports the integration and coordination of several cellular processes, as lipid, secretory and cell-surface protein synthesis, folding and modification, and trafficking. It is delimited by a membrane bilayer and consists of interconnected network of flattened, membrane-enclosed sacs or tube-like structures known as cisternae, enclosing a continuous lumenal space. Since several ER residing proteins bind Ca^{2+}, the overall $[Ca^{2+}]$ in its lumen can be more than 1 mM, whereas the free $[Ca^{2+}]$ reaches ~ 100-700 µM.

ER is generally considered a dynamic organelle, closely connected with mitochondria. In particular, the two networks generate a definite intracellular compartment, the Mitochondria-Associated Membranes (MAMs). Through physical proximity provided by MAMs, ER and mitochondria can intensively communicate, and ER selectively conveys physiological and pathological Ca^{2+} signals directly to mitochondria, thus affecting crucial processes like energy production, metabolism, and apoptosis [131]; [132]; [133]. These specialized hotspots at the interface between the two organelles have been identified as microdomains enriched in Ca^{2+} signalling factors, whose composition depends on cell type and status.

The Ca^{2+} transport from the endoplasmic reticulum is mainly mediated by the integral membrane ligand-gated channels Inositol 1,4,5-trisphosphate receptors (IP3Rs) [134], although Ca^{2+} may be released also by Ryanodine receptors. In some tissues IP3Rs are expressed also at the plasma membrane, nucleus, vesicles, and Golgi apparatus.

This ubiquitous intracellular Ca^{2+} pathway is stimulated by numerous extracellular ligands, including growth factors, hormones and neurotransmitters, which interact with the plasma membrane G protein-coupled receptors (GPCRs) or receptor tyrosine kinases. GPCRs, a family of receptors typical of eukaryotic cells, display a characteristic spatial organization consisting of seven transmembrane loops, with a N-terminal on the extracellular side, representing the agonist target, and an intracellular C-terminal. These receptors are coupled to heterotrimeric G proteins, constituted by three subunits α, β, γ. Upon agonist binding, which causes a conformational change in the intracellular domain of the receptor, the GPCR exchanges the GDP bound to the G protein with a GTP, leading to α subunit activation. The α subunit-GTP dissociate from the β and γ subunits and, in relation to the specific α subunit type (Gαs, Gαi, Gαq), interact with definite intracellular targets.

Specifically, Gαq proteins lead to the activation of Phospholipase C (PLC)-β, a phosphodiesterase responsible for the hydrolyses of the membrane phospholipid phosphatidylinositol 4,5-bisphosphate (PIP$_2$), leading to the generation of Diacylglycerol (DAG) and Inositol 1,4,5-trisphosphate (IP3) [135]. Whereas DAG affects the activity of some protein kinase C isoforms, IP3, able to diffuse in the cytosol, binds to IP3R, causing its opening an Ca^{2+} release, following the electrochemical gradient, into the cytosol, where it spreads via passive diffusion. IP3 stimulates Ca^{2+} release also from the Golgi apparatus, nucleus, and secretory vesicles. A distinct distribution pattern of IP3R, effectors, and Ca^{2+} binding proteins acing as buffers, provides cell-specific spatial and temporal properties of this signalling system.

Since the total [Ca^{2+}]$_{ER}$ is estimated to be a 1000-10000-fold higher compared to the cytosol, the existing Ca^{2+} gradient promotes the signal activation via the two channels. The IP3R distribution and organization within clusters, in cooperation with the regulation mediated by IP3 and Ca^{2+}, allow the formation of local and long-range Ca^{2+} signals. Starting from the opening of single IP3R at a discrete site, the Ca^{2+} released induces the coordinated opening of multiple IP3R channels within the same cluster, through a process named Ca^{2+}-induced Ca^{2+} release (CICR). Moreover, Ca^{2+} released from one cluster can activate adjacent clusters by CICR, leading to the generation of Ca^{2+} waves, which propagate in a saltatory manner. Single cell studies revealed that Ca^{2+} signals occur as repetitive spikes or oscillations and the frequency is tuned by the intensity of the stimulation, and these responses may remain highly localized in discrete parts of the cell or propagate as waves.

IP3R is a glycoprotein receptor with a molecular weight of approximately 260 kDa. It was at first purified and characterized from rat cerebellum [136] and, the evidence of the native protein molecular mass of about 1 MDa revealed that the functional receptor exists as a tetramer, consisting of identical or different subtypes subunits. Electron microscopy analysis revealed that IP3R can reversibly switch between two fourfold symmetry structures, a square and a windmill structure, and Ca^{2+} is responsible for the transition from the square to the windmill configuration, by repositioning the four peripheral IP3-binding domains [137].

In mammalian cells, three different genes are known to encode for three different isoforms of the receptor, which share 60-80% amino acids sequence homology. The isoform variability derives from the alternative splicing and the IP3R homo- and hetero-tetrameric assembly into functional channels. Indeed, each IP3R isoform has splice variants, for example type 1 IP3R has three main splice regions (Fig.12), and likely two further isoforms (IV and V) exist [138].

In mammals, IP3R has a ubiquitous pattern of expression and most cells express multiple isoforms, changing in response to physiological and pathological factors, differentiation

and development. Expression of more than one isoform offers the functional redundancy likely necessary because of the critical importance of IP3R-Ca^{2+}-signalling. The diverse IP3Rs expression pattern reflects the specificity of Ca^{2+} signals required in the different biological contexts. For example, IP3R1 is the dominant isoform in neuronal cells and smooth muscle, while IP3R2 in skeletal and cardiac muscle, and IP3R3 has a widespread expression in all tissues.

Besides their localization, the different properties between the IP3R isoforms rely to specific regulation mechanisms, including expression levels, post-transcriptional and post-translational modifications, and regulation mediate by other proteins. It has been suggested that the different isoforms may have different IP3 affinity, in particular that IP3R2 is more sensitive than IP3R1, and both are substantially more sensitive than IP3R3 [139]. There are differences also in the response of each isoform to the activation mediated by Ca^{2+}, responsible for the generation of unique CICR and specific spatial and temporal Ca^{2+} signals.

3.1 IP3R structure

Functional IP3R channel consists of four IP3R molecules, each one containing a cytoplasmic N-terminus, a hydrophobic region containing six transmembrane helices, and a cytoplasmic C-terminus (Fig. 12). A subnanometer-level resolution was reached through cryo-electron microscopy (cryo-EM) of functional IP3R1, the most studied among the IP3Rs.
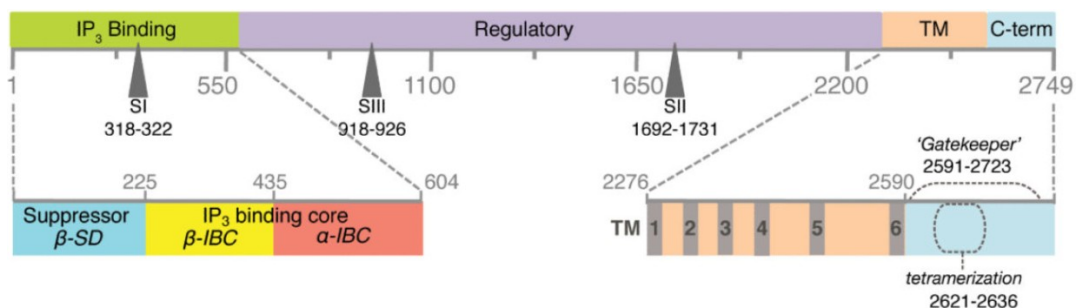
Figure 12 | Topology of structure-functional domains in primary sequence of IP3R. Four key regions defined in the primary structure of IP3R are highlighted: the N-terminal ligand-binding region, the large central modulatory region, the membrane-spanning/pore-forming, and the C-terminal 'gate-keeping' region; SI, SII and SIII refer to the three splice sites. Lower panel shows detailed topology of domains within the N- and C-terminal regions. Adapted from "Toward a High-Resolution Structure of IP3R Channel" Serysheva, Cell Calcium; 56(3):125-32 (2014).

The N-terminal region contains a proximal IP3 binding domain or IP3 binding core and a distal regulatory/coupling domain. The observation that deleting the amino-terminal 410 amino acids of IP3R prevented its binding to the ligand IP3, although it was still able to

form high molecular weight complexes [140], led to the definition of the IP3 binding domain, extending from amino acid 226 to 578 of mouse IP3R1, as the minimal sufficient region required for the binding to IP3 [141]. Further experiments subsequently identified the same IP3 binding site in the other isoforms. IP3 binding to IP3R induces conformational changes that lead to the activation gate and a following ion movement across the channel. Conserved positively charged residues, such as Arg265, Lys508 and Arg511, are crucial for the interaction with the highly charged molecule IP3, as shown by site-directed mutagenesis [141]. Nevertheless, more than one N-terminal sequence contributes to generate the IP3 binding site, probably helped by the tertiary structure.

The first 223 amino acids of mouse IP3R1 form the inhibitory or suppressor domain, which suppresses the binding with IP3, as demonstrated by IP3R 10- to 100-fold higher affinity after deletion of this region, compared with the full-length receptor [141]. Amino acids ranging from 1 to 223 are also crucial for the functional coupling between the N- and C-terminus. Experimental evidences suggest that the suppressor domain is required for IP3-induced channel gating and Ca^{2+} release, since when the entire domain is removed from the receptor, it can still bind IP3 but cannot function, in particular a single aromatic residue (Tyr167 in IP3R1 and Trp168 in IP3R3) seems to be critical for the coupling between ligand binding and channel gating [142].

Between the IP3 binding domain and the pore, there is the regulatory and transducing domain, a region encompassing consensus sequences for binding and phosphorylation by several factors. This region plays a critical role in coupling the IP3 binding to the channel gating. Within this modulatory domain, there are several consensus sites for the binding of small molecules and factors involved IP3R regulation, including Ca^{2+}, CaBP1, Calmodulin (CaM), ATP, RACK1, Caspase 3, and CARP. Phosphorylation sites for several protein kinases, as cAMP-dependent protein kinase (PKA), Ca^{2+}-calmodulin-dependent protein kinase II (CaMKII), Protein Kinase C (PKC), cGMP-dependent protein kinase (PKG), are located within this region.

IP3R is embedded in the ER membrane by six putative transmembrane domains TM1-TM6, extending between residues 2276 and 2589 of IP3R1, while the C-terminal region of the protein is pointing into the cytoplasm. Between TM5 and TM6 there is a critical sequence for creating the basic pore structure in the center of the channel, formed by the two helices and the luminal loop that links them to each of the four subunits, and harbors two N-glycosylation sites, Asn2475 and Asn2503 [143]. It has been demonstrated by experimental data showing that a channel constituted by only helices 5 and 6 displayed normal conductance and selectivity properties [144]. The high density of luminal negatively charged acidic residues likely contributes to concentrate the positively charged calcium ions. To note, IP3R can also mediate the transport of other divalent and monovalent cations, as Mg^{2+}, Sr^{2+}, Ba^{2+}, Na^+, K^+, Li^+, Cs^+ and Rb^+. A helical linker domain,

which connects the ligand-binding to the TM domains, creates the functional link with the channel opening, probably in addition to a multiple inter- and intra-domain interfaces. Furthermore, the C-terminal region has a key role in the tetramerization, helped by more distal cytoplasmic regions. Indeed, the minimum structural requirements for the tetramer formation are included between TM5 and the C-terminus, since IP3R containing only the transmembrane and the cytoplasmic C-terminal region still formed tetramers, while upon deletion of the transmembrane domain it resulted monomeric [145]; [146]. IP3R are co-translationally targeted and retained to the ER thanks to redundant signals, and this targeting depends on its transmembrane domains.

The last 160 residues, extending from the end of TM6 to the C-terminus, contain the cytoplasmic C-terminal tail or coupling domain. This domain cooperates with the TM for the receptor tetramerization and directly interacts with the N-terminus. Moreover, the tail is involved in the channel functionality, since the removal of the last 14 residues reduced the channel Ca^{2+} conductance [147]. This tail has been observed to interact with numerous proteins, including ankyrin, chromogranin A, Cytochrome *c*, and 4.1N, prevalently enhancing the IP3R sensitivity to IP3.

3.2 IP3R regulation

IP3R activation requires both IP3 and Ca^{2+}, which basically act as channel co-agonists. Conformational change induced by IP3 or Ca^{2+} binding to IP3R spreads within the transmembrane region and causes the pore opening.

Ca^{2+} acts as a key regulator of IP3R channel function, since it is fundamentally the real IP3R ligand. Although initial theories proposed that cytosolic Ca^{2+} affects its release in an inhibitory way [148]**,** patch-clamp experiments and molecular models highlighted a more intricate regulation mechanism, which consists of both inhibitory and stimulatory effects [149]; [150]. Indeed, Ca^{2+} acts on IP3R with biphasic regulation: at low $[Ca^{2+}]$, of about 100 nM, enhances the response to IP3, while at higher concentrations reaching ~5 µM reduces the IP3R Ca^{2+} release ability. The receptor responsiveness to the ion is due to the multiple Ca^{2+} binding sites located within the protein, two residing within the IP3-binding core, five within the modulatory domain, and one in the channel region. The stimulatory and inhibitory effects of cytosolic Ca^{2+} are probably mediated by two independent Ca^{2+} binding sites. Additionally, the inhibition of IP3R mediated by Ca^{2+} contributes to switch off the local cytosolic Ca^{2+} signals and even luminal Ca^{2+} probably modulates the IP3R sensitivity to the cytosolic regulation. The CICR allows an activated IP3R to propagate the signal to adjacent receptors. Therefore, a specific localization of Ca^{2+} signals coordinates the response to different stimuli or to stimuli with different intensities, and local Ca^{2+} signals can selectively control local responses. In addition, since Ca^{2+}-binding effectors modulate their response in dependence to transient or

sustained signals, the Ca^{2+} increase duration and frequency determine the nature and the amplitude of the response.

The principal effect of IP3 binding to IP3R is to trigger Ca^{2+} release from the ER [151]. IP3 acts by tuning the sensitivity of the receptor to Ca^{2+}, by relieving the IP3R inhibition mediated by Ca^{2+} [152]. For channel opening, it is necessary the IP3 binding to all the four subunits, thus inducing the conformational change responsible for Ca^{2+}-binding site sensitization. Then, upon Ca^{2+} binding, the channel opens and initiates the Ca^{2+} release.

ATP affects IP3R activity in a biphasic way, although it is not essential for the channel gating. ATP upregulates the receptor activity at low concentrations, within micromolar, and downregulates it when reaches millimolar levels. The consensus binding motif residing within the modulatory domain is involved in the stimulatory effect, whereas the inhibition relies to the ATP highly charged nature, which provides a competitive antagonism against IP3 for its binding site.

Numerous different proteins control IP3Rs expression, localization, and function, and most of them act via their interaction with the suppressor domain, the IP3-binding core, or the regions adjacent to the pore.

IP3R activity is controlled via specific phosphorylation and dephosphorylation. Moreover, several IP3R regulators are themselves substrates or bind both protein kinases and phosphatases, thus providing a localized regulation of Ca^{2+} signals [153]. It has been demonstrated how cAMP-dependent protein kinase (PKA) phosphorylation of IP3R upregulates Ca^{2+} release [154]; and two consensus sites, Ser1589 and Ser1755, have been identified on IP3R1, three on IP3R3, Ser916, Ser934, and Ser1832. cGMP-dependent protein kinase (PKG) phosphorylates IP3R1 at the same sites of PKA [155]. IP3R phosphorylation is further mediated by numerous protein tyrosine kinases (PTKs), protein kinase C (PKC), Akt, and calmodulin-dependent protein kinase II (CaMKII).

In addition, proto-oncogenes and tumor suppressors, as PTEN, PML, Bcl-2, and BRCA1, affect IP3Rs functionality decreasing and enhancing it, respectively. A wide range of proteins are known to interact with IP3R, including IRBIT, ER lumen-specific protein ERp44, Cytochrome *c*, and the proteases caspase-3 and calpain.

Additional regulation is provided by a wide range of stimulators and inhibitors. Proteins encompassing EF-hand Ca^{2+}-binding motifs, including Ca^{2+}-binding protein calmodulin (CaM), NCS-1, and Ca^{2+}-binding protein 1 (CaBP1), are involved in IP3Rs modulation. CaM binding with IP3R occurs both in the presence and absence of Ca^{2+} and reduces the affinity for IP3 and the Ca^{2+} release [156]. Caffeine is known to exert an inhibitory effect on both IP3R1 and IP3R3 [157].

Even the cellular redox state affects IP3Rs activity [158]. The switch from a reduced to an oxidized state, which causes oxidative stress, can provoke IP3Rs oxidation and the

substantial increase of its sensitivity. IP3R1 is known to be activated by oxidative reagents. Among them, thimerosal, which increases the $[Ca^{2+}]_i$, is the well-studied.

Crucial point for IP3Rs activity is represented by its expression levels within the cell. Most of mechanisms controlling IP3R transcription are Ca^{2+} dependent, but Ca^{2+}-independent mechanisms or acting via specific drugs are also known. At post-transcriptional level, IP3Rs mRNA is modulated by microRNAs. IP3R expression is finally limited by its ubiquitylation and following proteasomal degradation via endoplasmic reticulum-associated degradation (ERAD) [159].

Results

1. c-Src regulates the intracellular Ca^{2+} homeostasis

The starting point of this project was to investigate if the protein tyrosin kinase c-Src modulates the intracellular Ca^{2+} signalling. To measure Ca^{2+} homeostasis at the subcellular level, we used the Ca^{2+}-sensitive photoprotein aequorin that, owing to specific sequences targeted to defined intracellular organelles, enables to measure the Ca^{2+} concentrations in specific cellular compartments, including cytosol, mitochondria, and endoplasmic reticulum. The measurements were performed in HeLa cells, transiently expressing the appropriate aequorin, encompassing a different tag depending on the intracellular compartment or organelle to probe.

Using a cytosolic targeted aequorin (cytAEQ), we measured the concentration of free cytosolic Ca^{2+} ($[Ca^{2+}]_{cyt}$) upon stimulation with the extracellular agonist Histamine (100 µM), which triggers the generation of Inositol 1,4,5-trisphosphate (IP3) and the subsequent release of Ca^{2+} from the ER. Compared to the control condition, c-Src wild-type (Src wt) overexpressing cells showed a significant reduction of $[Ca^{2+}]_{cyt}$ evoked by Histamine (Fig. 13A). In order to deeply investigate the c-Src effect on Ca^{2+} homeostasis, we monitored the Ca^{2+} content in the mitochondrial compartment, using an aequorin specifically directed to this organelle (mtAEQmut). As shown in Figure 13B, upon Histamine stimulation, the Src wt overexpressing condition displayed a strong reduction in mitochondrial Ca^{2+} concentration ($[Ca^{2+}]_{mt}$).

Since the source of the Ca^{2+} involved in the pathway of our interest is the ER, the main Ca^{2+} intracellular store, we further investigated the c-Src effect on Ca^{2+} dynamics at this site. Indeed, a decrease in the $[Ca^{2+}]$ at cytosol and mitochondria is directly depending on a lower amount of Ca^{2+} accumulated or a reduction of Ca^{2+} released from the ER. For the measurements we employed a ER-targeted aequorin (erAEQ). To accurately analyze both the refilling and release Ca^{2+} kinetics, a complete emptying of the organelle is required, followed by Ca^{2+} refilling, which reflects the Ca^{2+} accumulation, then the agonist stimulation allowed to examine the Ca^{2+} depletion. The latter consists of an initial rapid phase, responsible for the most of Ca^{2+} amount released by ER, and a slow phase, due to the inhibition of Ca^{2+} release by Ca^{2+} itself. The traces in Figure 13C illustrate the ER Ca^{2+} kinetics: compared to the control, c-Src overexpression led to a slight but significant reduction in the total amount of Ca^{2+} accumulated by the ER. While the refilling rate was not influenced by c-Src (Fig. 13D), the ER Ca^{2+} efflux was significantly lower compared to the control (Fig. 13E). Furthermore, c-Src overexpressing condition displayed a substantial reduction in the total amount of Ca^{2+} released from the ER during the rapid phase (Fig. 13F).

Taken together, these data strongly support the assumption that c-Src controls the intracellular Ca^{2+} fluxes, acting mostly on the Ca^{2+} release from the ER upon agonist stimulation, which is responsible for the overall reduction of the Ca^{2+} levels at cytosol and mitochondria.
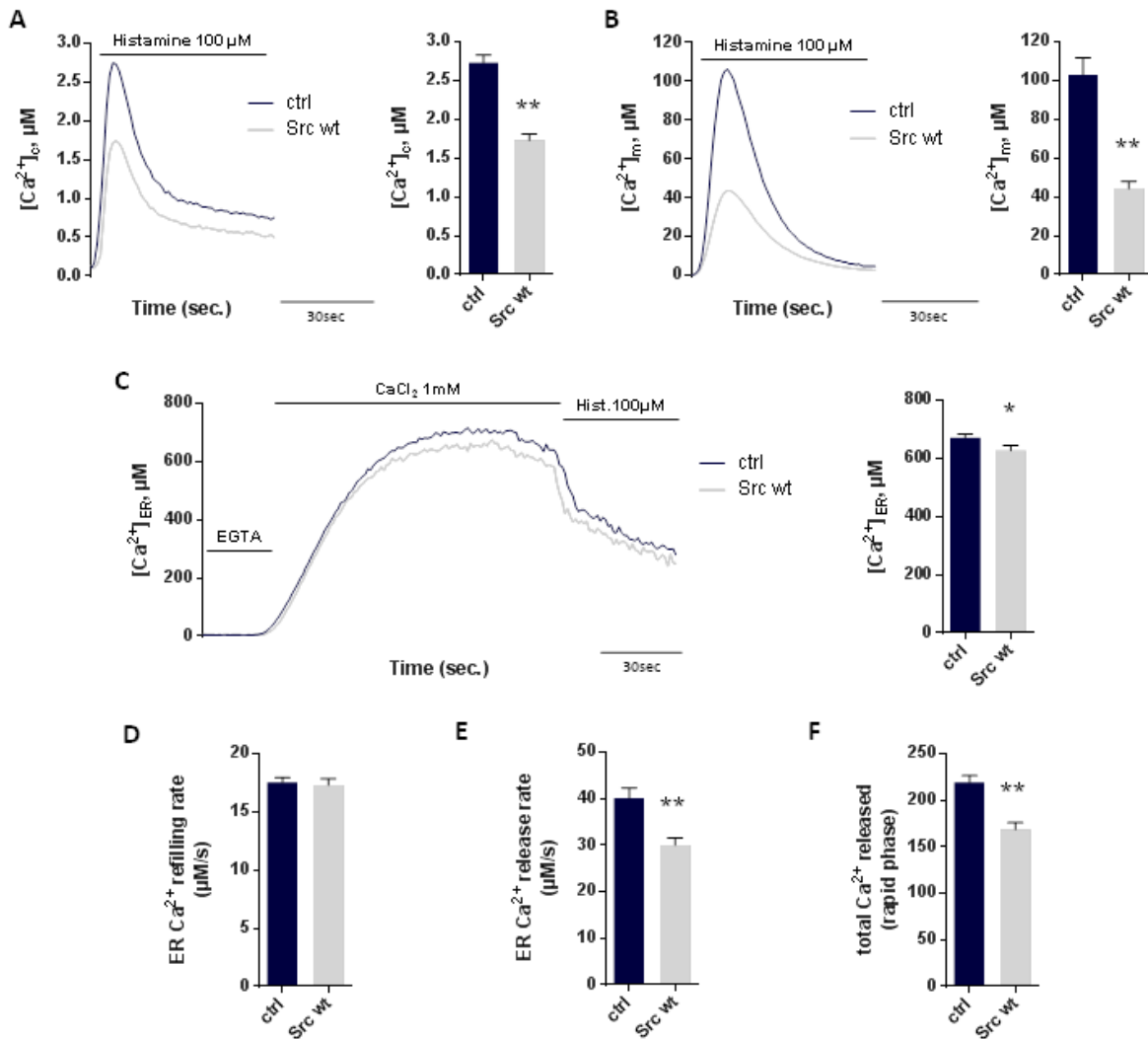
Figure 13. c-Src regulates the intracellular Ca^{2+} homeostasis.

(A) Cytosolic Ca^{2+} levels measurements in control and Src wt-overexpressing HeLa cells, using cytoplasmic aequorin (cytAEQ). **(B)** Mitochondrial Ca^{2+} measurements in control and Src wt-overexpressing HeLa cells, using mitochondrially targeted aequorin (mtAEQmut). **(C)** ER Ca^{2+} measurements in control and Src wt-overexpressing HeLa cells, using aequorin targeted to endoplasmic reticulum (erAEQ). **(D)** ER maximum Ca^{2+} refilling rate. **(E)** ER maximum Ca^{2+} release rate. **(F)** Total amount of Ca^{2+} released during the rapid phase. To induce Ca^{2+} release from ER, cells were stimulated with Histamine 100 µM, an agonist that, through interaction with G-protein-coupled receptors, evokes a rapid discharge from IP3Rs. The bars in a-c indicate the Ca^{2+} levels. All traces are from single representative experiments and $[Ca^{2+}]$ are presented as means of at least 20 experiments (± stdev). T Test * $p < 0.05$; ** $p < 0.01$ vs ctrl.

2. c-Src kinase activity and N-terminal domain are required for the modulation of Ca^{2+} dynamics

As specific structural or functional roles have been associated to c-Src different domains (Fig. 14A), we took advantage of several c-Src mutants harboring single amino acid substitutions or deletion of entire domains. We monitored the mitochondrial Ca^{2+} uptake upon Histamine stimulation in HeLa cells upon overexpression of a group that includes c-Src mutants characterized by null or constitutively catalytic activity, and a second mutants group characterized by mutations that suppress the function related to each domain.

The mutants with increased or reduced kinasic activity were useful to assess if c-Src acts on intracellular Ca^{2+} dynamics via target proteins phospholylation (Fig. 14B). c-Src constitutively active mutants, Src Y530F and Src ΔC-ter, lacking the negative effect of Tyr530 and the entire C-terminus, respectively, drastically reduced the $[Ca^{2+}]_{mt}$ compared to both control and Src wt conditions. By contrast, the cells overexpressing the catalytically inactive mutant Src K298R, in which the Arg298 substitution with Lys prevents the binding with ATP, the double mutant Src K298R Y530F, which cannot be inhibited but is catalytically dead, and Src Y419F, a mutant that is unable to reach a stable active configuration, lost the ability to downregulate Ca^{2+} uptake by mitochondria. Furthermore, Src S75A, which cannot reach a maximal kinase activity, displayed an effect similar to Src wt. Collectively, these data confirm that c-Src kinase activity is essential for the regulation of Ca^{2+} intracellular levels.

The next measurements provided a detailed definition of the role of each domain in the Ca^{2+} modulation. $[Ca^{2+}]_{mt}$ reduction was not influenced by deletion of SH3 or SH2 domain (Src ΔSH3 and Src ΔSH2) or amino acid substitution (Src W121A and Src R178A) of the residues responsible for the interaction with target proteins containing proline-rich motifs or p-Tyr (Fig. 14C and D). This means that SH3/SH2-related functions are not involved in c-Src control of Ca^{2+} homeostasis and that c-Src acts on its target directly. Furthermore, since the two domains are also involved in the inhibitory intramolecular interactions, the entire deletion or point mutation affecting the residue responsible for the bindings, led to a constitutively active kinases. This is confirmed by the null effect exerted by a further point mutation that prevents c-Src inactivation (Src W121A Y530F, Src R178A Y530F), compared to the single point mutation (Fig. 14C). Similarly, $[Ca^{2+}]_{mt}$ diminution was not affected by deletion of L1 and L2 linker regions (Fig. 14D), indicating that the two sequences are not required for Ca^{2+} regulation. Instead, their removal prevents the molecule locking in the inactive configuration, producing a constitutively active kinase. $[Ca^{2+}]_{mt}$ was comparable to those of Src wt overexpressing cells upon deletion of the Unique domain, a data that prompted us to conclude that it is dispensable for the c-Src function investigated (Fig. 14D). The only indispensable region resulted the N-terminus

domain, as the cells transfected with Src Δ1-87 completely lost the modulatory effect on Ca^{2+} (Fig. 14D).

Taken together, the data obtained from these measurements established that c-Src-mediated Ca^{2+} handling strictly depends on its kinase activity and that the membrane anchorage, provided by the N-terminal region, is crucial to carry out this function.

Ca^{2+} measurements, in both cytosol and ER, upon overexpression of those mutants that displayed the most interesting effects, further corroborated the mitochondrial Ca^{2+} analysis. Indeed, the constitutively active mutant Src Y530F strongly downregulated the $[Ca^{2+}]_{cyt}$, while the kinase dead Src K298R and the mutant lacking the N-terminus Src Δ1-87, lost the effect owned by Src wt (Fig. 14E). At the ER, Src Y530F provoked a significant reduction in the total $[Ca^{2+}]_{ER}$ (Fig. 14F), refilling rate (Fig. 14G), releasing Ca^{2+} rate (Fig. 14H) and total amount of release during the rapid phase (Fig. 14I), compared to both control and Src wt. All these effects were completely lost with the kinase dead and Src Δ1-87 mutants overexpression (Fig. 14F, G, H and I).

Nevertheless, to further test whether the N-terminus and the kinase domain were the only regions responsible for the c-Src-mediated Ca^{2+} handling, we made an additional c-Src mutant, Src ΔSH3-L2, lacking all the regions previously identified as not required for Ca^{2+} modulation, thus encompassing only the N-terminus, the kinase domain and the C-terminal regulatory tail. In both cytosolic (Fig. 14J) and mitochondrial (Fig. 14K) compartments Src ΔSH3-L2 overexpression caused a significant reduction of $[Ca^{2+}]$, compared to both control and Src wt. The ER Ca^{2+} kinetics (Fig. 14L) reveal that Src ΔSH3-L2 still affected the total $[Ca^{2+}]_{ER}$, the maximal refilling and releasing rate, and consequently reduced the total Ca^{2+} released from the ER (Fig. 14L, M, N and O). These data definitively demonstrated that only the functions related to its catalytic domain and N-terminus, likely due to the anchorage to a definite cellular membrane, are crucial for the c-Src-related Ca^{2+} handling.

A
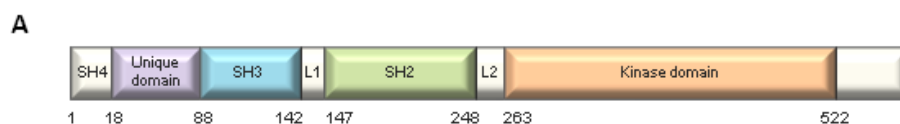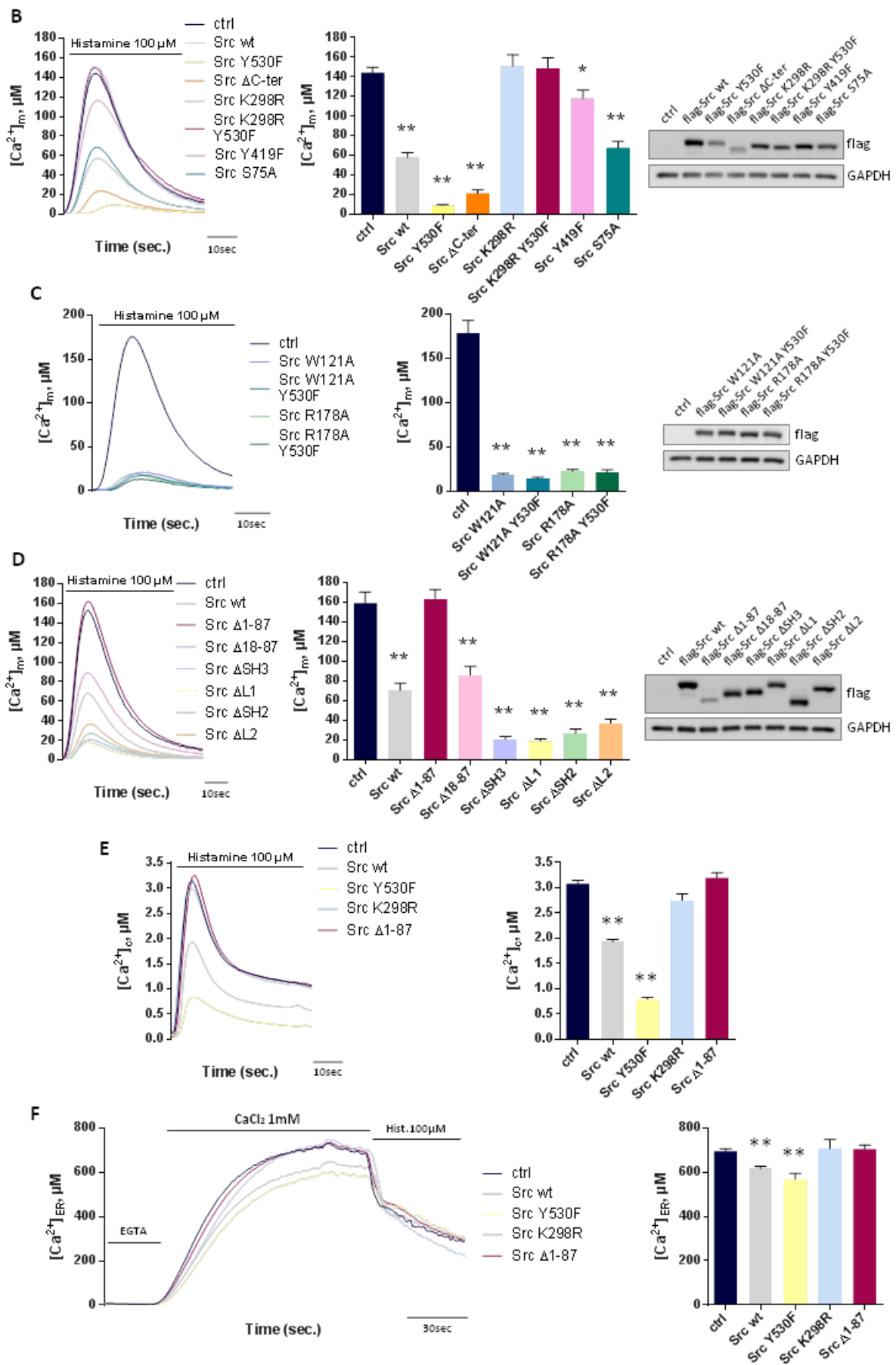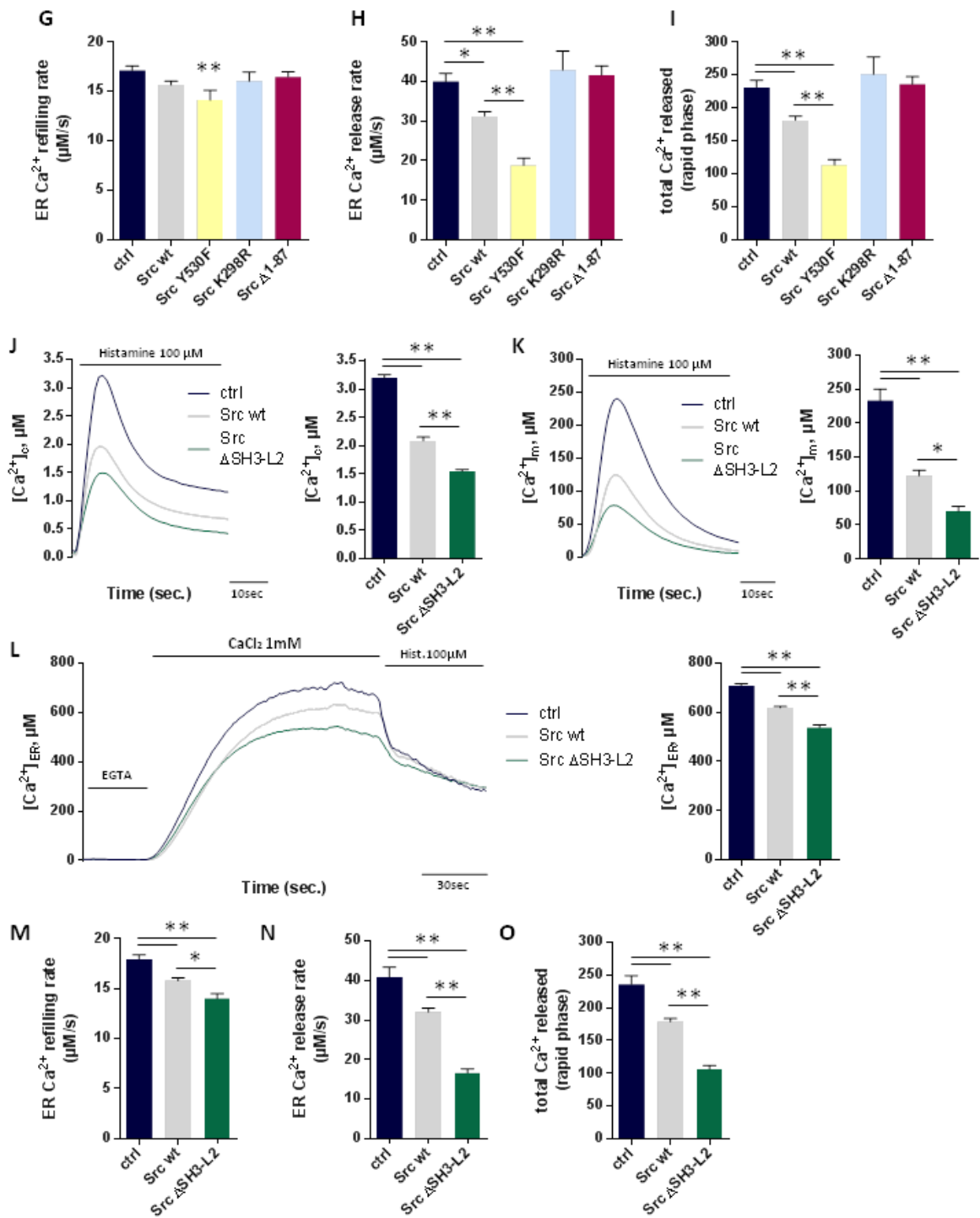
Figure 14.

Figure 14.

Figure 14. c-Src kinase activity and N-terminal domain are required for the modulation of Ca²⁺ dynamics.

(A) Structural organization of human c-Src. c-Src mutants: Src Δ1-87 → deletion of N-terminal region; Src Δ18-87 → deletion of Unique domain; Src ΔSH3/Src W121A → inactivated SH3 domain binding to poly-proline motifs; Src W121A Y530F → open conformation, inactivated SH3 domain; Src ΔSH2/Src R178A → inactivated phospho-tyrosine binding by the SH2 domain; Src R178A Y530F → conformationally open, inactivated SH2 domain; Src ΔL1/Src ΔL2 → deletions of structural linker regions; Src Y530F/Src ΔC-ter → lack the negative regulatory tyrosine (constitutively active c-Src); Src K298R → lacks a critical lysine in the ATP-binding pocket (completely inactive c-Src); Src K298R Y530F → conformationally open but catalytically inactive; Src Y419F → lacks the positive regulatory tyrosine for maximal kinase activity; Src S75A → lacks a

positive regulatory serine for maximal kinase activity; Src ΔSH3-L2 → Src mutant containing the N-terminus, the kinase domain and the C-terminal regulatory tail.

Mitochondrial Ca^{2+} measurements in HeLa cells, using aequorin targeted to mitochondria (mtAEQmut). For the measurements, in **(B)** cells were transiently transfected with c-Src mutants displaying increased or reduced kinase activity (Src Y530F, Src ΔC-ter, Src K298R, Src K298R Y530F, Src Y419F, Src S75A); in **(C)** cells were transiently transfected with c-Src point mutants lacking specific interaction properties (Src W121A, Src W121A Y530F, Src R178A, and Src R178A Y530F); in **(D)** cells were transiently transfected with c-Src deletion mutants (Src Δ1-87, Src Δ18-87, Src ΔSH3, Src ΔL1, Src ΔSH2 and Src ΔL2) and compared to control. **(E)** Cytosolic and **(F)** ER Ca^{2+} measurements in HeLa cells, using cytoplasmic aequorin (cytAEQ) and aequorin targeted to endoplasmic reticulum (erAEQ), respectively. Cells were transiently transfected with constitutively active c-Src mutant (Src Y530F), kinase dead Src mutant (Src K298R), and the Src mutant lacking the N-terminal region (Src Δ1-87). **(G)** ER maximum Ca^{2+} refilling rate. **(H)** ER maximum Ca^{2+} release rate. **(I)** Total Ca^{2+} released during the rapid Ca^{2+} releasing phase. Cytosolic, mitochondrial and ER Ca^{2+} measurements in HeLa cells overexpressing Src wt and Src ΔSH3-L2, compared to control. In **(J)** cells overexpress the cytoplasmic aequorin (cytAEQ), in **(K)** the specifically mitochondrially targeted aequorin (mtAEQmut), and in **(L)** the endoplasmic reticulum targeted aequorin (erAEQ). **(M)** ER maximum Ca^{2+} refilling rate. **(N)** ER maximum Ca^{2+} release rate. **(O)** Total Ca^{2+} released during the rapid Ca^{2+} releasing phase. ER Ca^{2+} release was stimulated with Histamine 100 μM to induce Ca^{2+} release from ER. The bars in the graphs indicate the Ca^{2+} levels, presented as means of at least 20 experiments (± stdev). All traces are from single representative experiments. ANOVA test * $p < 0.05$; ** $p < 0.01$.

3. c-Src effect on intracellular Ca^{2+} homeostasis is cell-autonomous

All the previous experiments, demonstrating the c-Src crucial role in the control of intracellular Ca^{2+} signalling pathway, were executed in HeLa cells, a human immortalized adenocarcinoma epithelial cell line. Thus, in order to investigate if it represents a widespread phenomenon rather than a cell-dependent mechanism, we performed the key experiments in other cell types. Since it is well established the link between c-Src increased protein levels and activity and human colon cancer [160], we monitored the mitochondrial Ca^{2+} uptake in HCT 116 cells, a human colorectal carcinoma cell line. $[Ca^{2+}]_{mt}$ was significantly downregulated by Src Y530F upon Adenosine triphosphate (ATP, 100 μM) stimulation, but not by Src wt nor Src K298R, the latter displaying $[Ca^{2+}]_{mt}$ even higher compared to the control (Fig. 15A). Similarly, in COS-7 cells, a fibroblast-like cell line derived from African green monkey kidney, Src Y530F significantly affected the $[Ca^{2+}]_m$ upon ATP stimulation, whereas Src K298R acted as a dominant negative mutant (Fig. 15C). Otherwise, NIH 3T3 cells, a mouse embryo fibroblast cell line, overexpressing Src wt and simulated with Bradykinin 1 μM, displayed a decreased $[Ca^{2+}]_{mt}$ compared to the control, in Src Y530F overexpressing cells the effect was strongly amplified, while it was prevented with Src K298R (Fig. 15B). Compared to what happened in HeLa cells, in these three cell lines c-Src effect on $[Ca^{2+}]_{mt}$ resulted weaker, as Src wt had a null or drastically lower effect compared to the control. Collectively, the experiments discussed above confirmed that the c-Src role as modulator of intracellular Ca^{2+} signalling is conserved in several biological contexts.
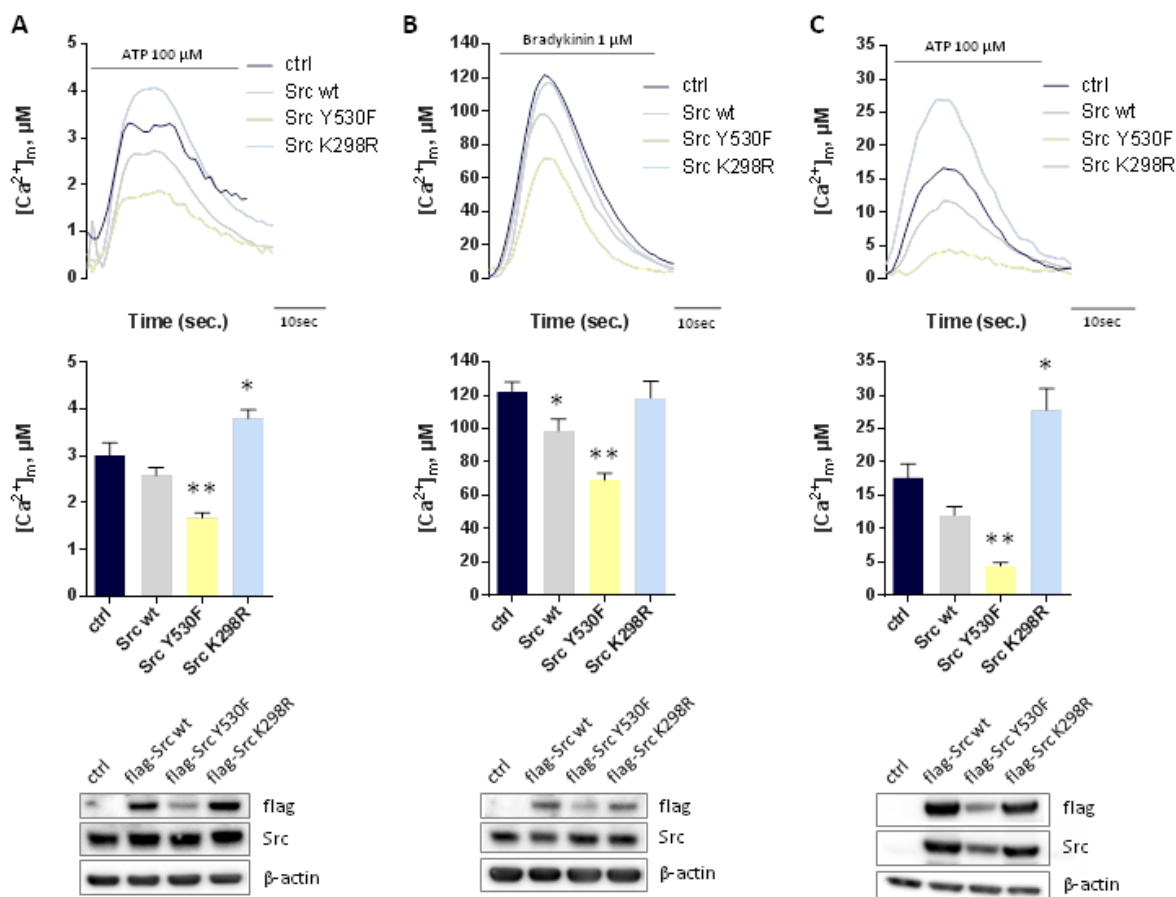
Figure 15. c-Src effect on intracellular Ca^{2+} homeostasis is cell-autonomous.
Mitochondrial Ca^{2+} measurements in HCT 116 **(A)**, NIH 3T3 **(B)**, COS7 **(C)** cells. Src wt, Src Y530F and Src K298R-overexpressing cells are compared to control (pcDNA3), using mitochondrially targeted aequorin (mtAEQwt for HCT 116 cells, mtAEQmut for NIH 3T3 and COS7 cells). For the measurements, HCT 116 and COS7 cells were challenged with ATP 100 μM, NIH 3T3 cells with Bradykinin 1 μM, as agonists to induce Ca^{2+} release from ER. The bars indicate the levels of mitochondrial Ca^{2+} uptake, presented as means of at least 20 experiments (± stdev). ANOVA test * $p < 0.05$, ** $p < 0.01$ vs ctrl. The western blots show c-Src endogenous levels (Src) and the levels of the overexpressed constructs (flag) in the three different cell lines. β-actin was used as a loading control.

4. c-Src phosphorylates IP3R3 at MAMs

The next aim was to define the molecular mechanism underlying the c-Src modulation of Ca^{2+} dynamics and to identify the target of c-Src, which likely mediates this alteration of Ca^{2+} signalling.

As c-Src functions seem to be strictly related to its subcellular distribution, at first, we investigated in detail the intracellular localization of the protein kinase via subcellular fractionation. Interestingly, endogenous c-Src in HeLa (Fig. 16A, left) and HEK293T (Fig. 16A, right) cells was detected partially in the mitochondrial (Mc, Mp) and ER fractions, and predominantly at MAMs (mitochondria-associated membranes). However, although Src wt and Src ΔSH3-L2 constructs revealed the same pattern of distribution as the endogenous kinase, Src Δ1-87 mutant was highly enriched in the cytosolic fraction (C), suggesting its

inability localize at other different intracellular compartments, in particular at MAMs (Fig. 16C). This assumption was further supported by Na_2CO_3-based extraction, a technique that allows the separation of the membrane-associated proteins (pellet) from those proteins with a free cytoplasmic localization (sur), showing that the c-Src mutant lacking the N-terminus was completely unable to localize to the membrane-associated fraction, since it was detected as free protein in the supernatant fraction (Fig. 16B). Intriguingly, Src wt and the mutant containing the minimal regions required for Ca^{2+} modulation displayed a typical membrane-bound distribution, by contrast the c-Src mutant that lost the effect on Ca^{2+} handling, Src Δ1-87, simultaneously lacked the property to anchor to membranes and to localize at MAMs.

Focusing on the data demonstrating c-Src to modulate Ca^{2+} release from ER and to localize at MAMs, and since MAMs represent a preferential site of Ca^{2+} exchange from ER to mitochondria [131]; [132], we investigated if Inositol 1,4,5-trisphosphate receptors (IP3Rs), the main channels involved in the ER Ca^{2+} release [161]; [134], could be a c-Src molecular target. Among the IP3R isoforms, we focused on the isoform 3, the mainly expressed at MAMs [162], and assessed the interaction of c-Src with IP3R3 and its phosphorylation status. Immunoprecipitation assay on HEK293T cells transiently expressing wild-type IP3R3 (IP3R3 wt) and the different GFP-tagged c-Src mutants, showed that both Src wt and Src ΔSH3-L2 interacted with and phosphorylated IP3R3 (Fig. 16D). By contrast, Src Δ1-87 mutant did not interact with the receptor, and IP3R3 phosphorylation levels were strongly reduced and comparable to those of the control condition (GFP-EV).

At this point, we asked if Src Δ1-87 still conserved its kinase activity and the undetected IP3R3 phosphorylation was due to their missing interaction, or if the N-terminus deletion somehow affected the catalytic activity. We checked the phosphorylation levels of Stat3, a known c-Src substrate, which is directly phosphorylated by the kinase at Tyr705 [163]. Immunoblot analysis of HeLa cells transiently transfected with the GFP-tagged c-Src constructs, shows that Stat3 was still phosphorylated by Src Δ1-87, at levels comparable to those of Src wt (Fig. 16E). Thus, deletion of 1-87 region of c-Src did not affect its catalytic property. The relation existing between c-Src kinase activity, interaction with IP3R3 and phosphorylation of the receptor, was further clarified through an immunoprecipitation experiment in HEK293T cells revealing that, independently from their kinase activity, both the constitutively active and the kinase dead mutant interacted with IP3R3 (Fig. 16F). These observations prompted us to conclude that Src Δ1-87 mutant inability to phosphorylate IP3R3 was a consequence of the lacking interaction with its target.

Collectively, our data established that c-Src directly phosphorylates IP3R3 at MAMs, leading to a downregulation of the receptor activity, thus reducing the amount of Ca^{2+} that

can spread in the cytosol and be internalized by mitochondria. However, without its N-terminal region, c-Src cannot be targeted at MAMs and, consequently, results unable to phosphorylate the IP3R3 and to modulate the Ca^{2+} intracellular levels.
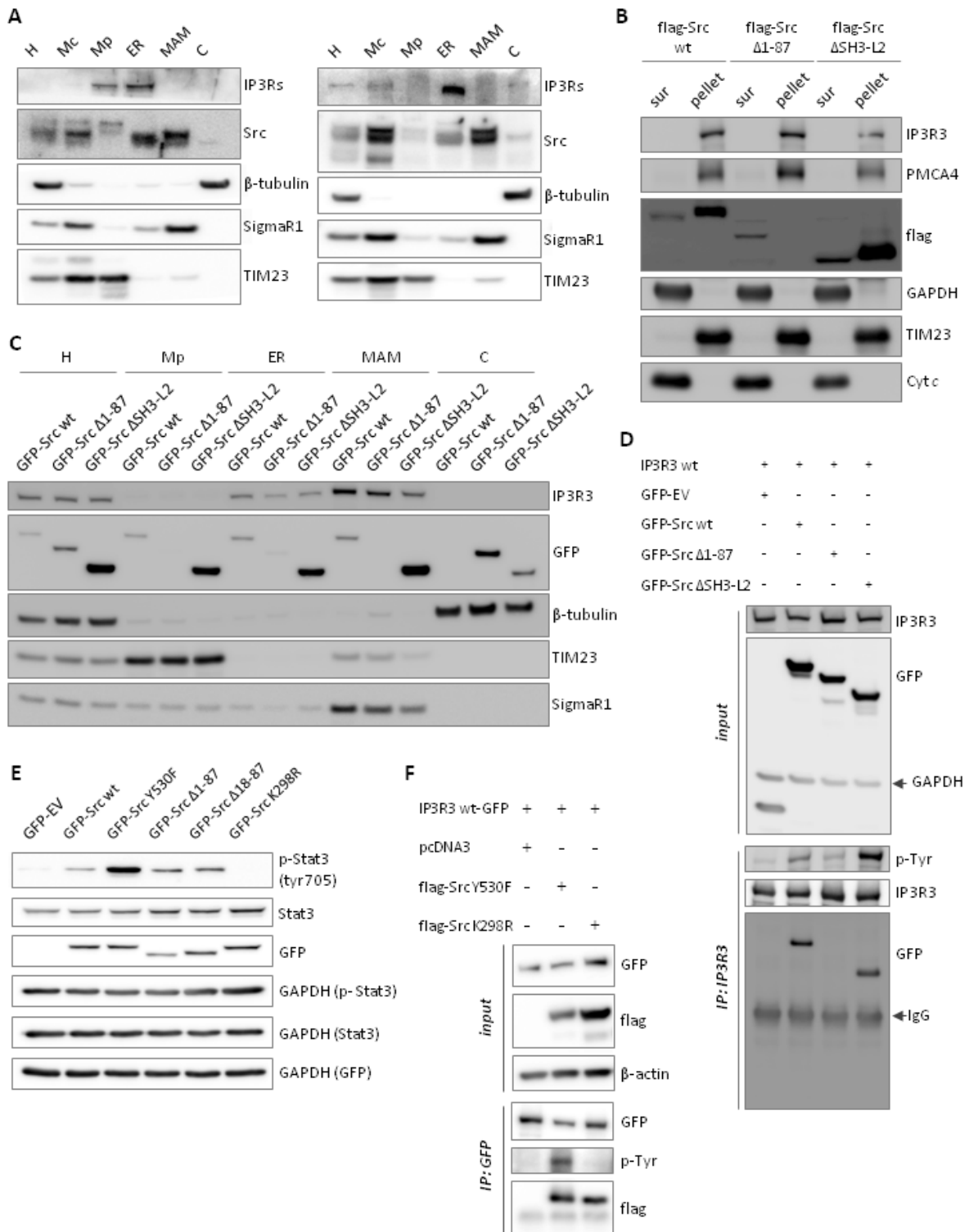

Figure 16. c-Src phosphorylates IP3R3 at MAMs.

(A) Protein components of subcellular fractions prepared from HeLa (left) and HEK293T (right) cells revealed by immunoblot analysis showing the endogenous c-Src intracellular localization. H, homogenate; Mc, crude mitochondrial fraction; Mp, pure mitochondrial fraction; ER, endoplasmic reticulum; MAM, mitochondria-

associated membranes; C, cytosol. Markers: IP3Rs (ER), β-tubulin (cytosol), SigmaR1 (MAM), TIM23 (mitochondria). **(B)** Na$_2$CO$_3$-based extraction from HeLa cells revealed by immunoblot analysis. Markers: IP3R3, PMCA4 and TIM23 (pellet), GAPDH and Cyt *c* (sur). For the experiment, HeLa cells were transiently transfected with flag-Src wt, flag-Src Δ1-87, or flag-Src ΔSH3-L2. **(C)** Protein components of subcellular fractions prepared from HeLa cells stably expressing GFP-Src constructs (Src wt, Src Δ1-87, Src ΔSH3-L2) revealed by immunoblot analysis. H, homogenate; Mp, pure mitochondrial fraction; ER, endoplasmic reticulum; MAM, mitochondria-associated membrane; C, cytosol. Markers: IP3R3, SigmaR1 (MAM), β-tubulin (cytosol), TIM23 (mitochondria). **(D)** Immunoblotting showing the phosphorylation levels of IP3R3 on tyrosine residues (p-Tyr) and its interaction with the different GFP-tagged c-Src constructs (GFP), after immunoprecipitation (IP) of transiently overexpressed IP3R3 wt. GAPDH was used as a loading control. For the experiment, HEK293T cells were transiently transfected with GFP-Src wt, GFP-Src Δ1-87, GFP-Src ΔSH3-L2, or empty vector (GFP-EV) as negative control (input). **(E)** Immunoblotting showing the Stat3 phosphorylation levels on Tyr705. GAPDH was used as a loading control. HeLa cells were transiently transfected with GFP-Src wt, GFP-Src Y530F, GFP-Src Δ1-87, GFP-Src Δ18-87, GFP-Src K298R, or empty vector (ctrl). **(F)** Immunoblotting showing the phosphorylation levels of IP3R3 on tyrosine residues (p-Tyr) and its interaction with the different flag-tagged c-Src constructs (flag), after immunoprecipitation (IP) of transiently overexpressed IP3R3 wt-GFP. β-actin was used as a loading control. For the experiment, HEK293T cells were transiently transfected with flag-Src Y530F, flag-Src K298R, or pcDNA3 as negative control (input). The results are representative of three independent experiments.

Discussion

Starting from the intriguing clues indicating a partially shared signaling network for c-Src and Ca^{2+}, the aim of this project was to investigate a possible involvement of c-Src in the modulation of Ca^{2+} signals. It is well established the c-Src crucial role in multiple pathways controlling critical cellular events, including cell proliferation, cell death, cellular adhesion, migration and invasion [88]. Ca^{2+} ion acts as intracellular second messenger in the transduction from various stimuli into cellular signaling pathways controlling metabolism, differentiation, migration, proliferation, cell death, and secretion. As for c-Src, it is well known that Ca^{2+} is essential also throughout carcinogenesis and tumor progression, when Ca^{2+} homeostasis is extensively remodeled in order to promote some of emblematic cancer hallmarks, in particular unregulated cell proliferation and evasion of programmed cell death [109]; [164].

In this study we show that c-Src plays a key function in the regulation of Ca^{2+} homeostasis in the different intracellular compartments within several cell lines, reflecting a widespread phenomenon. We defined the molecular details underlying the c-Src modulation of Ca^{2+} dynamics. Our results demonstrated that c-Src acts on the Ca^{2+} release from the endoplasmic reticulum (Fig. 13C-F), by significantly reducing the overall Ca^{2+} released by the organelle upon agonist stimulation, leading to a subsequent decrease of the amount of Ca^{2+} that can spread in the cytosol (Fig. 13A) and the uptake by mitochondria (Fig. 13B).

Measurements upon overexpression of different c-Src mutants revealed that c-Src control of intracellular Ca^{2+} homeostasis is strictly related to its catalytic activity (Fig. 14B) and is driven by the membrane targeting provided by the N-terminal region (Fig. 14D) [88]; [97]; [165]. N-terminal myristoylation and membrane anchorage are known to direct c-Src in the different intracellular sites and affect its kinase activity and stability [166]. However, our results revealed that even after deletion of the entire N-terminal region that prevents its membrane translocation (Fig. 16B), c-Src preserved its catalytic activity (Fig. 16E).

Literature data abundantly affirm that c-Src functions are strictly dependent on its association with specific membrane-associated assemblies, and that c-Src is mainly cytoplasmic in resting conditions, but was also observed at plasma membrane upon activation [90]; [167], at endosomes, mitochondria, and secretory vesicles [92]; [93]; [94]; [95]. Here, we provide the unprecedented evidence that a fraction of c-Src is localized at the MAMs, driven by its N-terminal sequence (Fig. 16A and C). Several proteins, including proto-oncogenes and tumor suppressors, have been already observed to exert their function at MAMs, which act also as a physical and functional scaffold [168]; [131]; [169].

MAMs are specialized and close membrane contact sites between the ER and mitochondria and are currently considered a subcellular compartment involved in a selective exchange of physiological and pathological Ca^{2+} signals [170]; [131]; [132].

Interestingly, we demonstrated that this anchorage to MAM membranes is essential for c-Src modulation of Ca^{2+} fluxes and identified IP3R3 as c-Src direct target at this site (Fig. 16D). Indeed, our data showing that the intracellular Ca^{2+} handling was still observed even preventing its interaction with other proteins (Fig. 14C and D), suggest that the c-Src action on its target is direct. IP3Rs are the most important receptors responsible for Ca^{2+} release from the ER, which can be regulated by phosphorylation, along with the various mechanisms [161]; [134]; [153], and the isoform 3 is the most abundant at MAMs [162]. The assumption that IP3R3 represents the c-Src effector in the Ca^{2+} modulating pathway is further corroborated by the evidence that the N-terminus removal from the c-Src molecule prevented the interaction with IP3R3 and the receptor phosphorylation, whereas did not affect the kinase potential (Fig. 16D and E).

In contrast with our data, several reports delineate an opposite effect of Src. In 1992 v-src was linked, in the context of T cell receptor (TCR) stimulation, to intracellular Ca^{2+} increase [171]. Another group related the enhanced Ca^{2+} release during T and B cell activation to the phosphorylation of IP3R1 at Tyr353 mediated by Fyn [172]; [173]. On the other hand, their data also suggested that Fyn might phosphorylate other tyrosine residues besides Tyr353, indicating that SFKs might regulate IP3Rs activity in multiple ways. Another report showed as Lck positively regulates IP3R1 upon strong TCR stimulation [174]. However, these studies were performed in particular cellular models, therefore this regulation of IP3Rs mediated by SFKs might be specific and limited to some biological contexts, in response to antigen-induced lymphocyte activation. Indeed, it has yet been established an IP3Rs pivotal role in Ca^{2+} signalling during lymphocyte activation and SFKs are known to be involved in TCR stimulation [175]; [176]; [177]. Yokoyama et al. demonstrated that, upon B cell stimulation, the Ca^{2+} mobilization enhanced by the protein BANK is associated to Lyn-mediated IP3R2 phosphorylation [178]. Nevertheless, BANK expression is restricted to functional BCR-expressing B cells. Thus, also this pathway may be specifically induced by foreign antigen-induced immune responses. Similarly, c-Src enhancement of Ca^{2+} release through IP3R2 phosphorylation induced by ouabain [179], or via IP3R1 phosphorylation in response to IL-1 [180], and downstream of PKG1 activation in osteoclasts motility [181], might be highly limited for specific events in definite contexts. Moreover, these Ca^{2+} measurements were performed upon a pharmacological manipulation of Src activity, whereas our method, consisting of a genetic approach, ensures a higher degree of specificity.

Our experiments showed that when c-Src loses its ability to anchor to membranes, due to the deletion of the N-terminus residues, it cannot localize at the MAM compartment (Fig. 16C), interact with IP3R3, and phosphorylate its target (fig. 16D). We speculated that the N-myristoylation could be responsible for the c-Src targeting at MAMs. Indeed, it has been

already demonstrated the N-myristoylation role in protein post-translationally targeting at mitochondria, ER, and MAMs [182]; [183]; [184]; [185].

Our overall findings demonstrated that c-Src contributes to the regulation of the intracellular Ca^{2+} signal and point out a novel mechanism of action of this important oncogene. Our current work is aimed to map the c-Src interaction with IP3R3, with the purpose to identify the specific tyrosine residue(s) that could be crucial for the c-Src-dependent regulation of ER Ca^{2+} efflux.

This signaling cascade is likely critical for one or more events that drive the cell fate. This assumption might open an interesting view on the regulation of c-Src activity in the context of both physiological and pathological conditions, especially in cancer developing and progression. Therefore, ongoing experiments and future studies are aimed at investigating the biological effect underlying this alteration of Ca^{2+} signalling c-Src-mediated. Intriguingly, the definition of a link between this newly identified pathway and specific pathological events, and the possibility to manipulate the c-Src outcomes at multiple levels, might provide new insights for the identification of therapeutic targets.

Materials and methods

Cell culture and transfection

HeLa, HEK293T, HCT 116, NIH 3T3, and COS-7 cells were cultured in Dulbecco's modified Eagle's medium (DMEM) (Euroclone) supplemented with 10% fetal bovine serum (FBS; Life Technologies), 2 mM L-glutamine, 100 U/ml penicillin, and 100 mg/ml streptomycin (all from Euroclone). For HeLa, HEK293T, HCT 116 and COS7 cells transient transfections were performed with a standard calcium-phosphate procedure. For NIH 3T3 cell line transient transfections were performed using Lipofectamine LTX (Thermo Fisher Scientific) as transfecting reagent.

To produce a stable cell line, HeLa cells were transfected with the different GFP-Src constructs using a standard calcium phosphate procedure. To select the cells that have integrated the plasmid containing a selectable marker was used a complete medium with G418 0,8 mg/ml. After three days, the medium was replaced with G418 0,2 mg/ml complete medium. The selection medium was changed every 3 days for 3-4 weeks. When large colonies of cells were clearly visible, they were picked and expanded.

Aequorin measurements

For the experiments with the chimeric aequorins targeted to cytosol (cytAEQ) and mitochondria (mtAEQwt/mtAEQmut), cells were seeded and transfected. Before the measurement, cells were incubated for 1,5 h with 5 µM coelenterazine in Krebs-Ringer modified buffer (KRB; 125 mM NaCl, 5 mM KCl, 1 mM Na_3PO_4, 1 mM $MgSO_4$, 5.5 mM glucose, and 20 mM 4-(2-hydroxyethyl)-1-piperazineethanesulfonic acid [HEPES], pH 7.4, at 37°C) supplemented with 1 mM $CaCl_2$, and then transferred to the perfusion chamber. To reconstitute the endoplasmic reticulum targeted aequorin (erAEQ), initially the ER luminal [Ca^{2+}] was drastically reduced by incubation for 45 min at 4°C (in order to preserve membranes integrity) in KRB supplemented with 5 µM coelenterazine, 5 µM Ca^{2+} ionophore ionomycin (Sigma-Aldrich), and 600 µM EGTA. Then cells were extensively washed with KRB supplemented with 2% bovine serum albumin (BSA) and 1 mM EGTA, and then transferred to the perfusion chamber. All the measurements were carried out in KRB supplemented with either 1 mM $CaCl_2$ (cytAEQ and mtAEQ) or 100 µM EGTA (erAEQ), and the agonist (Histamine 100 µM, ATP 100 µM, or Bradykinin 1 µM) was added to the same medium. The experiments were concluded by lysing cells with Triton X-100 in a hypotonic Ca^{2+}-rich solution (10 mM $CaCl_2$ in H_2O), thus discharging the remaining aequorin pool. Briefly, a 13 mm-round coverslip with the transfected cells was placed in a perfused, thermostatted chamber, placed in the close proximity of a low-noise photomultiplier, with built-in amplifier-discriminator. The output of the discriminator was captured by the photon counter C8855-01 connected via a USB cable to a workstation

and recorded by the sample software (Hamamatsu Photonics). The aequorin luminescence data were calibrated off-line into $[Ca^{2+}]$ values, using a computer algorithm based on the Ca^{2+} response curve of wild-type and mutant aequorins [186].

Sub-cellular fractionation

Cell fractionation was performed as previously described [187]. Approximately 10^9 cells were harvested, washed in phosphate-buffered saline medium (PBS), and pelleted by centrifugation at 600 g for 5 min. The pellet was suspended in homogenization buffer (225 mM mannitol, 75 mM sucrose, 30 mM Tris-HCl pH 7.4) and gently disrupted by Dounce homogenization. The homogenate was centrifuged twice at 600 g for 5 min to remove nuclei and unbroken cells, and the supernatant was centrifuged at 10,300 g for 10 min to pellet crude mitochondria, which were resuspended in homogenization buffer. The supernatant was centrifuged at 20,000 g for 30 min. Additional centrifugation of the supernatant at 100,000 g for 90 min (70-Ti rotor; Beckman) lead to the isolation of ER (pellet) and cytosolic fraction (supernatant). To purify mitochondria, the crude mitochondrial fraction was suspended in isolation buffer (250 mM mannitol, 5 mM HEPES pH 7.4, and 0.5 mM EGTA), layered on top of 8 ml of Percoll medium (225 mM mannitol, 25 mM HEPES pH 7.4, 1 mM EGTA, and 30% v/v Percoll) and subjected to Percoll gradient centrifugation in a 10 ml polycarbonate ultracentrifuge tube, at 95,000 g for 30 min (SW40 rotor; Beckman). The band containing purified mitochondria was removed and diluted with isolation medium, washed twice by centrifugation at 6,300 g for 10 min to remove the Percoll, and finally resuspended in isolation medium. MAMs, removed from the Percoll gradient as a diffuse white band located above the mitochondria, were diluted in isolation medium and centrifuged at 6,300 g for 10 min. The supernatant containing MAMs was centrifuged at 100,000 g for 1 h in a Beckman 70 Ti rotor, and the resulting pellet was resuspended in the homogenization buffer. All centrifugation steps were performed at 4°C. The quality of the preparation was assessed by immunoblot analysis using different markers for the fractions obtained.

Na_2CO_3-based extraction

Cells were harvested, washed in phosphate-buffered saline medium (PBS), and pelleted by centrifugation at 2500 rpm for 5 min. The pellet was resuspended and incubated in 100 mM Na_2CO_3 pH 11,3 for 30 min on ice and then pelletted at 36,500 rpm for 30 min at 4°C. Both the pellet and the supernatant were resuspended in 100 mM Na_2CO_3 and concentrated by TCA incubation for 30 min on ice. After centrifugation at max speed for 30 min at 4°C, both the pellet and the supernatant were incubated in ice cold acetone for 15 min on ice. After centrifugation at max speed for 20 min at 4°C, the samples were resuspended in 2x Laemly sample buffer.

Immunoprecipitation

For immunoprecipitation experiments, cells were lysed in an appropriate volume of lysis buffer (50 mM Tris-HCl pH 7.4, 0.1% NP-40, 0.05% SDS, 10% Glycerol, 50 mM NaF, 150 mM NaCl, protease inhibitor mixture and Phos-STOP Phosphatase Inhibitor Cocktail (Roche Applied Science)). The same proteins amount from the whole cell lysate of each condition was incubated overnight with the specific primary antibody at 4°C. Precipitation of the immune complexes was performed with protein A/G-coated Sepharose beads (GE Healthcare). Beads were pelleted and washed three times with lysis buffer at 4°C. The bait was eluted in 2x Laemly sample buffer and denatured for 5 min at 100°C. The whole cell lysate (input) and the immunoprecipitated (IP) samples were separated by SDS-PAGE and analyzed by immunoblot (see below).

Immunoblotting

For immunoblotting, cells were washed with ice-cold phosphate-buffered saline (PBS), scraped and lysed, for 30 min on ice, in a buffer containing 50 mM TrisHCl pH 7.4, 150 mM NaCl, 1% Triton X-100, 0.2% SDS, protease and phosphates inhibitor cocktail. After centrifugation at 12,000 rcf for 10 min, proteins were quantified by the Lowry method and 10-15 µg of total proteins, denatured for 5 min at 100°C in LDS sample buffer (Life Technologies) and Sample Reducing Agent (Life Technologies), were loaded on a Novex NuPage Bis-Tris 4-12% precast gel (Life Technologies), and transferred onto nitrocellulose membranes. To saturate unspecific binding sites, the membranes were incubated with TBS-Tween-20 (0.05%) supplemented with 5% non-fat powdered milk for 1 h at RT, and then incubated overnight with primary antibodies. The revelation was assessed by specific horseradish peroxidase-labeled secondary antibodies (Thermo Fisher Scientific), followed by detection by chemiluminescence (Thermo Fisher Scientific), using ImageQuant LAS 4000 (GE Healthcare). Western blots shown in figures are representative of at least 3 different independent experiments.

The antibodies used are: flag (Sigma-Aldrich, 1:1000), c-Src (Cell Signaling, 1:1000), β-actin (Sigma-Aldrich, 1:10000), IP3Rs (Millipore, 1:1000), β-tubulin (Sigma-Aldrich, 1:5000), SigmaR1 (Sigma-Aldrich, 1:1000), TIM23 (BD Transduction Laboratories, 1:1000), IP3R3 (BD Transduction Laboratories, 1:1000), PMCA4 (Sigma-Aldrich, 1:1000), GAPDH (Cell Signaling, 1:5000), Cytochrome *c* (BD Biosciences, 1:5000), GFP (Santa Cruz Biotechnology, 1:1000), phospho-Tyr (Cell Signaling, 1:500), Stat3 (Cell Signaling, 1:1000), phospho-Stat3 (Tyr705, Cell Signaling, 1:1000).

Statistical analysis

The results were expressed as the mean ±SD. The probability of statistical differences between experimental groups was determined by the ANOVA test. To determine the

statistical significance between two groups was used the Student's T-test. p values <0.05 were considered statistically significant.

References

1. Clatterbuck, R.E., et al., *Ultrastructural and immunocytochemical evidence that an incompetent blood-brain barrier is related to the pathophysiology of cavernous malformations.* J Neurol Neurosurg Psychiatry, 2001. **71**(2): p. 188-92.

2. Gault, J., et al., *Pathobiology of human cerebrovascular malformations: basic mechanisms and clinical relevance.* Neurosurgery, 2004. **55**(1): p. 1-16; discussion 16-7.

3. Batra, S., et al., *Cavernous malformations: natural history, diagnosis and treatment.* Nat Rev Neurol, 2009. **5**(12): p. 659-70.

4. Cavalcanti, D.D., et al., *Cerebral cavernous malformations: from genes to proteins to disease.* J Neurosurg, 2012. **116**(1): p. 122-32.

5. Riant, F., et al., *Recent insights into cerebral cavernous malformations: the molecular genetics of CCM.* FEBS J, 2010. **277**(5): p. 1070-5.

6. Akers, A.L., et al., *Biallelic somatic and germline mutations in cerebral cavernous malformations (CCMs): evidence for a two-hit mechanism of CCM pathogenesis.* Hum Mol Genet, 2009. **18**(5): p. 919-30.

7. Serebriiskii, I., et al., *Association of Krev-1/rap1a with Krit1, a novel ankyrin repeat-containing protein encoded by a gene mapping to 7q21-22.* Oncogene, 1997. **15**(9): p. 1043-9.

8. Craig, H.D., et al., *Multilocus linkage identifies two new loci for a mendelian form of stroke, cerebral cavernous malformation, at 7p15-13 and 3q25.2-27.* Hum Mol Genet, 1998. **7**(12): p. 1851-8.

9. Liu, W., et al., *Mechanism for KRIT1 release of ICAP1-mediated suppression of integrin activation.* Mol Cell, 2013. **49**(4): p. 719-29.

10. Francalanci, F., et al., *Structural and functional differences between KRIT1A and KRIT1B isoforms: a framework for understanding CCM pathogenesis.* Exp Cell Res, 2009. **315**(2): p. 285-303.

11. Liquori, C.L., et al., *Mutations in a gene encoding a novel protein containing a phosphotyrosine-binding domain cause type 2 cerebral cavernous malformations.* Am J Hum Genet, 2003. **73**(6): p. 1459-64.

12. Uhlik, M.T., et al., *Rac-MEKK3-MKK3 scaffolding for p38 MAPK activation during hyperosmotic shock.* Nat Cell Biol, 2003. **5**(12): p. 1104-10.

13. Zhang, J., et al., *Interaction between krit1 and malcavernin: implications for the pathogenesis of cerebral cavernous malformations.* Neurosurgery, 2007. **60**(2): p. 353-9; discussion 359.

14. Fisher, O.S., et al., *Structural studies of cerebral cavernous malformations 2 (CCM2) reveal a folded helical domain at its C-terminus.* FEBS Lett, 2013. **587**(3): p. 272-7.

15. Bergametti, F., et al., *Mutations within the programmed cell death 10 gene cause cerebral cavernous malformations.* Am J Hum Genet, 2005. **76**(1): p. 42-51.

16. Gunel, M., et al., *KRIT1, a gene mutated in cerebral cavernous malformation, encodes a microtubule-associated protein.* Proc Natl Acad Sci U S A, 2002. **99**(16): p. 10677-82.

17. Glading, A., et al., *KRIT-1/CCM1 is a Rap1 effector that regulates endothelial cell cell junctions.* J Cell Biol, 2007. **179**(2): p. 247-54.

18. Zhang, J., et al., *Interaction between krit1 and icap1alpha infers perturbation of integrin beta1-mediated angiogenesis in the pathogenesis of cerebral cavernous malformation.* Hum Mol Genet, 2001. **10**(25): p. 2953-60.

19. Fournier, H.N., et al., *Nuclear translocation of integrin cytoplasmic domain-associated protein 1 stimulates cellular proliferation.* Mol Biol Cell, 2005. **16**(4): p. 1859-71.

20. Kleaveland, B., et al., *Regulation of cardiovascular development and integrity by the heart of glass-cerebral cavernous malformation protein pathway.* Nat Med, 2009. **15**(2): p. 169-76.

21. You, C., et al., *Loss of CCM3 impairs DLL4-Notch signalling: implication in endothelial angiogenesis and in inherited cerebral cavernous malformations.* J Cell Mol Med, 2013. **17**(3): p. 407-18.

22. Zhang, M., et al., *Structural mechanism of CCM3 heterodimerization with GCKIII kinases.* Structure, 2013. **21**(4): p. 680-8.

23. Kean, M.J., et al., *Structure-function analysis of core STRIPAK Proteins: a signaling complex implicated in Golgi polarization.* J Biol Chem, 2011. **286**(28): p. 25065-75.

24. Jenny Zhou, H., et al., *Endothelial exocytosis of angiopoietin-2 resulting from CCM3 deficiency contributes to cerebral cavernous malformation.* Nat Med, 2016. **22**(9): p. 1033-1042.

25. Crose, L.E., et al., *Cerebral cavernous malformation 2 protein promotes smad ubiquitin regulatory factor 1-mediated RhoA degradation in endothelial cells.* J Biol Chem, 2009. **284**(20): p. 13301-5.

26. Harel, L., et al., *CCM2 mediates death signaling by the TrkA receptor tyrosine kinase.* Neuron, 2009. **63**(5): p. 585-91.

27. Maddaluno, L., et al., *EndMT contributes to the onset and progression of cerebral cavernous malformations.* Nature, 2013. **498**(7455): p. 492-6.

28. Goitre, L., et al., *KRIT1 regulates the homeostasis of intracellular reactive oxygen species.* PLoS One, 2010. **5**(7): p. e11786.

29. Goitre, L., et al., *KRIT1 loss of function causes a ROS-dependent upregulation of c-Jun.* Free Radic Biol Med, 2014. **68**: p. 134-47.

30. Mizushima, N., et al., *Autophagy fights disease through cellular self-digestion.* Nature, 2008. **451**(7182): p. 1069-75.

31. Xie, Z. and D.J. Klionsky, *Autophagosome formation: core machinery and adaptations.* Nat Cell Biol, 2007. **9**(10): p. 1102-9.

32. Feng, Y., et al., *The machinery of macroautophagy.* Cell Res, 2014. **24**(1): p. 24-41.

33. Mizushima, N. and M. Komatsu, *Autophagy: renovation of cells and tissues.* Cell, 2011. **147**(4): p. 728-41.

34. Levine, B. and D.J. Klionsky, *Development by self-digestion: molecular mechanisms and biological functions of autophagy.* Dev Cell, 2004. **6**(4): p. 463-77.

35. Orenstein, S.J. and A.M. Cuervo, *Chaperone-mediated autophagy: molecular mechanisms and physiological relevance.* Semin Cell Dev Biol, 2010. **21**(7): p. 719-26.

36. Wong, P.M., et al., *The ULK1 complex: sensing nutrient signals for autophagy activation.* Autophagy, 2013. **9**(2): p. 124-37.

37. Itakura, E., et al., *Beclin 1 forms two distinct phosphatidylinositol 3-kinase complexes with mammalian Atg14 and UVRAG.* Mol Biol Cell, 2008. **19**(12): p. 5360-72.

38. Tanida, I., *Autophagy basics.* Microbiol Immunol, 2011. **55**(1): p. 1-11.

39. Mizushima, N., et al., *A protein conjugation system essential for autophagy.* Nature, 1998. **395**(6700): p. 395-8.

40. Ichimura, Y., et al., *A ubiquitin-like system mediates protein lipidation.* Nature, 2000. **408**(6811): p. 488-92.

41. Stromhaug, P.E. and P.O. Seglen, *Evidence for acidity of prelysosomal autophagic/endocytic vacuoles (amphisomes).* Biochem J, 1993. **291 (Pt 1)**: p. 115-21.

42. Behrends, C., et al., *Network organization of the human autophagy system.* Nature, 2010. **466**(7302): p. 68-76.

43. Sengupta, S., T.R. Peterson, and D.M. Sabatini, *Regulation of the mTOR complex 1 pathway by nutrients, growth factors, and stress.* Mol Cell, 2010. **40**(2): p. 310-22.

44. Hosokawa, N., et al., *Nutrient-dependent mTORC1 association with the ULK1-Atg13-FIP200 complex required for autophagy.* Mol Biol Cell, 2009. **20**(7): p. 1981-91.

45. Kim, J., et al., *AMPK and mTOR regulate autophagy through direct phosphorylation of Ulk1.* Nat Cell Biol, 2011. **13**(2): p. 132-41.

46. Vega-Rubin-de-Celis, S., et al., *Multistep regulation of TFEB by MTORC1.* Autophagy, 2017. **13**(3): p. 464-472.

47. Jiang, P. and N. Mizushima, *Autophagy and human diseases.* Cell Res, 2014. **24**(1): p. 69-79.

48. Boulday, G., et al., *Developmental timing of CCM2 loss influences cerebral cavernous malformations in mice.* J Exp Med, 2011. **208**(9): p. 1835-47.

49. Komatsu, M., et al., *Homeostatic levels of p62 control cytoplasmic inclusion body formation in autophagy-deficient mice.* Cell, 2007. **131**(6): p. 1149-63.

50. Mizushima, N., T. Yoshimori, and B. Levine, *Methods in mammalian autophagy research.* Cell, 2010. **140**(3): p. 313-26.

51. Wang, R.C., et al., *Akt-mediated regulation of autophagy and tumorigenesis through Beclin 1 phosphorylation.* Science, 2012. **338**(6109): p. 956-9.

52. Bjorkoy, G., et al., *p62/SQSTM1 forms protein aggregates degraded by autophagy and has a protective effect on huntingtin-induced cell death.* J Cell Biol, 2005. **171**(4): p. 603-14.

53. Gibson, C.C., et al., *Strategy for identifying repurposed drugs for the treatment of cerebral cavernous malformation.* Circulation, 2015. **131**(3): p. 289-99.

54. Puissant, A., et al., *Resveratrol promotes autophagic cell death in chronic myelogenous leukemia cells via JNK-mediated p62/SQSTM1 expression and AMPK activation.* Cancer Res, 2010. **70**(3): p. 1042-52.

55. He, C. and D.J. Klionsky, *Regulation mechanisms and signaling pathways of autophagy.* Annu Rev Genet, 2009. **43**: p. 67-93.

56. Puissant, A., N. Fenouille, and P. Auberger, *When autophagy meets cancer through p62/SQSTM1.* Am J Cancer Res, 2012. **2**(4): p. 397-413.

57. Klionsky, D.J., et al., *Guidelines for the use and interpretation of assays for monitoring autophagy.* Autophagy, 2012. **8**(4): p. 445-544.

58. Rabinowitz, J.D. and E. White, *Autophagy and metabolism.* Science, 2010. **330**(6009): p. 1344-8.

59. Cheng, Y., et al., *Therapeutic targeting of autophagy in disease: biology and pharmacology.* Pharmacol Rev, 2013. **65**(4): p. 1162-97.

60. Laplante, M. and D.M. Sabatini, *mTOR signaling in growth control and disease.* Cell, 2012. **149**(2): p. 274-93.

61. Kundu, M., *ULK1, mammalian target of rapamycin, and mitochondria: linking nutrient availability and autophagy.* Antioxid Redox Signal, 2011. **14**(10): p. 1953-8.

62. Hara, T., et al., *FIP200, a ULK-interacting protein, is required for autophagosome formation in mammalian cells.* J Cell Biol, 2008. **181**(3): p. 497-510.

63. Kundu, M., et al., *Ulk1 plays a critical role in the autophagic clearance of mitochondria and ribosomes during reticulocyte maturation.* Blood, 2008. **112**(4): p. 1493-502.

64. Nazio, F., et al., *mTOR inhibits autophagy by controlling ULK1 ubiquitylation, self-association and function through AMBRA1 and TRAF6.* Nat Cell Biol, 2013. **15**(4): p. 406-16.

65. Thoreen, C.C., et al., *An ATP-competitive mammalian target of rapamycin inhibitor reveals rapamycin-resistant functions of mTORC1.* J Biol Chem, 2009. **284**(12): p. 8023-32.

66. Rubinsztein, D.C., P. Codogno, and B. Levine, *Autophagy modulation as a potential therapeutic target for diverse diseases.* Nat Rev Drug Discov, 2012. **11**(9): p. 709-30.

67. Zhou, J., et al., *Dual suppressive effect of MTORC1 on autophagy: tame the dragon by shackling both the head and the tail.* Autophagy, 2013. **9**(5): p. 803-5.

68. Zhou, J., et al., *Activation of lysosomal function in the course of autophagy via mTORC1 suppression and autophagosome-lysosome fusion.* Cell Res, 2013. **23**(4): p. 508-23.

69. Bertrand, M., et al., *SQSTM1/p62 regulates the expression of junctional proteins through epithelial-mesenchymal transition factors.* Cell Cycle, 2015. **14**(3): p. 364-74.

70. Bravi, L., et al., *Sulindac metabolites decrease cerebrovascular malformations in CCM3-knockout mice.* Proc Natl Acad Sci U S A, 2015. **112**(27): p. 8421-6.

71. Labauge, P., et al., *Genetics of cavernous angiomas.* Lancet Neurol, 2007. **6**(3): p. 237-44.

72. Zatloukal, K., et al., *p62 Is a common component of cytoplasmic inclusions in protein aggregation diseases.* Am J Pathol, 2002. **160**(1): p. 255-63.

73. Martinet, W., et al., *Immunohistochemical analysis of macroautophagy: recommendations and limitations.* Autophagy, 2013. **9**(3): p. 386-402.

74. Waguri, S. and M. Komatsu, *Biochemical and morphological detection of inclusion bodies in autophagy-deficient mice.* Methods Enzymol, 2009. **453**: p. 181-96.

75. Choi, A.M., S.W. Ryter, and B. Levine, *Autophagy in human health and disease.* N Engl J Med, 2013. **368**(7): p. 651-62.

76. Fujita, K., et al., *Nrf2-mediated induction of p62 controls Toll-like receptor-4-driven aggresome-like induced structure formation and autophagic degradation.* Proc Natl Acad Sci U S A, 2011. **108**(4): p. 1427-32.

77. Magnaudeix, A., et al., *PP2A blockade inhibits autophagy and causes intraneuronal accumulation of ubiquitinated proteins.* Neurobiol Aging, 2013. **34**(3): p. 770-90.

78. Maejima, Y., et al., *Mst1 inhibits autophagy by promoting the interaction between Beclin1 and Bcl-2.* Nat Med, 2013. **19**(11): p. 1478-88.

79. Wolf, E., et al., *Miz1 is required to maintain autophagic flux.* Nat Commun, 2013. **4**: p. 2535.

80. Lackner, H., et al., *Sirolimus for the treatment of children with various complicated vascular anomalies.* Eur J Pediatr, 2015. **174**(12): p. 1579-84.

81. Kawasaki, J., et al., *RASA1 functions in EPHB4 signaling pathway to suppress endothelial mTORC1 activity.* J Clin Invest, 2014. **124**(6): p. 2774-84.

82. Maes, H., et al., *Tumor vessel normalization by chloroquine independent of autophagy.* Cancer Cell, 2014. **26**(2): p. 190-206.

83. Guerrero, A., et al., *The cerebral cavernous malformation 3 gene is necessary for senescence induction.* Aging Cell, 2015. **14**(2): p. 274-83.

84. Sefton, B.M., T. Hunter, and K. Beemon, *Product of in vitro translation of the Rous sarcoma virus src gene has protein kinase activity.* J Virol, 1979. **30**(1): p. 311-8.

85. Rous, P., *A Sarcoma of the Fowl Transmissible by an Agent Separable from the Tumor Cells.* J Exp Med, 1911. **13**(4): p. 397-411.

86. Martin, G.S., *The road to Src.* Oncogene, 2004. **23**(48): p. 7910-7.

87. Martin, G.S., *The hunting of the Src.* Nat Rev Mol Cell Biol, 2001. **2**(6): p. 467-75.

88. Brown, M.T. and J.A. Cooper, *Regulation, substrates and functions of src.* Biochim Biophys Acta, 1996. **1287**(2-3): p. 121-49.

89. Thomas, S.M. and J.S. Brugge, *Cellular functions regulated by Src family kinases.* Annu Rev Cell Dev Biol, 1997. **13**: p. 513-609.

90. Kaplan, J.M., H.E. Varmus, and J.M. Bishop, *The src protein contains multiple domains for specific attachment to membranes.* Mol Cell Biol, 1990. **10**(3): p. 1000-9.

91. Kaplan, K.B., et al., *Association of the amino-terminal half of c-Src with focal adhesions alters their properties and is regulated by phosphorylation of tyrosine 527.* EMBO J, 1994. **13**(20): p. 4745-56.

92. Kaplan, K.B., et al., *Association of p60c-src with endosomal membranes in mammalian fibroblasts.* J Cell Biol, 1992. **118**(2): p. 321-33.

93. Miyazaki, T., et al., *Regulation of cytochrome c oxidase activity by c-Src in osteoclasts.* J Cell Biol, 2003. **160**(5): p. 709-18.

94. Salvi, M., et al., *Characterization and location of Src-dependent tyrosine phosphorylation in rat brain mitochondria.* Biochim Biophys Acta, 2002. **1589**(2): p. 181-95.

95. Grandori, C. and H. Hanafusa, *p60c-src is complexed with a cellular protein in subcellular compartments involved in exocytosis.* J Cell Biol, 1988. **107**(6 Pt 1): p. 2125-35.

96. Manning, G., et al., *The protein kinase complement of the human genome.* Science, 2002. **298**(5600): p. 1912-34.

97. Resh, M.D., *Myristylation and palmitylation of Src family members: the fats of the matter.* Cell, 1994. **76**(3): p. 411-3.

98. Perez, Y., et al., *Lipid binding by the Unique and SH3 domains of c-Src suggests a new regulatory mechanism.* Sci Rep, 2013. **3**: p. 1295.

99. Ren, R., et al., *Identification of a ten-amino acid proline-rich SH3 binding site.* Science, 1993. **259**(5098): p. 1157-61.

100. Waksman, G., et al., *Binding of a high affinity phosphotyrosyl peptide to the Src SH2 domain: crystal structures of the complexed and peptide-free forms.* Cell, 1993. **72**(5): p. 779-90.

101. Kmiecik, T.E. and D. Shalloway, *Activation and suppression of pp60c-src transforming ability by mutation of its primary sites of tyrosine phosphorylation.* Cell, 1987. **49**(1): p. 65-73.

102. Xu, W., S.C. Harrison, and M.J. Eck, *Three-dimensional structure of the tyrosine kinase c-Src.* Nature, 1997. **385**(6617): p. 595-602.

103. Williams, J.C., et al., *The 2.35 A crystal structure of the inactivated form of chicken Src: a dynamic molecule with multiple regulatory interactions.* J Mol Biol, 1997. **274**(5): p. 757-75.

104. Cowan-Jacob, S.W., et al., *The crystal structure of a c-Src complex in an active conformation suggests possible steps in c-Src activation.* Structure, 2005. **13**(6): p. 861-71.

105. Su, J., M. Muranjan, and J. Sap, *Receptor protein tyrosine phosphatase alpha activates Src-family kinases and controls integrin-mediated responses in fibroblasts.* Curr Biol, 1999. **9**(10): p. 505-11.

106. Nada, S., et al., *Cloning of a complementary DNA for a protein-tyrosine kinase that specifically phosphorylates a negative regulatory site of p60c-src.* Nature, 1991. **351**(6321): p. 69-72.

107. Chong, Y.P., et al., *Endogenous and synthetic inhibitors of the Src-family protein tyrosine kinases.* Biochim Biophys Acta, 2005. **1754**(1-2): p. 210-20.

108. Hakak, Y. and G.S. Martin, *Ubiquitin-dependent degradation of active Src.* Curr Biol, 1999. **9**(18): p. 1039-42.

109. Irby, R.B. and T.J. Yeatman, *Role of Src expression and activation in human cancer.* Oncogene, 2000. **19**(49): p. 5636-42.

110. Berridge, M.J., P. Lipp, and M.D. Bootman, *The versatility and universality of calcium signalling.* Nat Rev Mol Cell Biol, 2000. **1**(1): p. 11-21.

111. Clapham, D.E., *Intracellular calcium. Replenishing the stores.* Nature, 1995. **375**(6533): p. 634-5.

112. Morgan, A.J. and A.P. Thomas, *Single cell and subcellular measurement of intracellular Ca2+ concentration ([Ca2+]i).* Methods Mol Biol, 1999. **114**: p. 93-123.

113. Jaffe, L.F. and R. Creton, *On the conservation of calcium wave speeds.* Cell Calcium, 1998. **24**(1): p. 1-8.

114. Petersen, O.H., D. Burdakov, and A.V. Tepikin, *Regulation of store-operated calcium entry: lessons from a polarized cell.* Eur J Cell Biol, 1999. **78**(4): p. 221-3.

115. Bennett, D.L., et al., *Expression and function of ryanodine receptors in nonexcitable cells.* J Biol Chem, 1996. **271**(11): p. 6356-62.

116. Giannini, G., et al., *The ryanodine receptor/calcium channel genes are widely and differentially expressed in murine brain and peripheral tissues.* J Cell Biol, 1995. **128**(5): p. 893-904.

117. Brini, M., *Plasma membrane Ca(2+)-ATPase: from a housekeeping function to a versatile signaling role.* Pflugers Arch, 2009. **457**(3): p. 657-64.

118. Brini, M. and E. Carafoli, *Calcium pumps in health and disease.* Physiol Rev, 2009. **89**(4): p. 1341-78.

119. Carafoli, E., *Biogenesis: plasma membrane calcium ATPase: 15 years of work on the purified enzyme.* FASEB J, 1994. **8**(13): p. 993-1002.

120. Philipson, K.D. and D.A. Nicoll, *Sodium-calcium exchange.* Curr Opin Cell Biol, 1992. **4**(4): p. 678-83.

121. Rizzuto, R., et al., *Ca(2+) transfer from the ER to mitochondria: when, how and why.* Biochim Biophys Acta, 2009. **1787**(11): p. 1342-51.

122. Shimomura, O., F.H. Johnson, and Y. Saiga, *Extraction, purification and properties of aequorin, a bioluminescent protein from the luminous hydromedusan, Aequorea.* J Cell Comp Physiol, 1962. **59**: p. 223-39.

123. Inouye, S., et al., *Cloning and sequence analysis of cDNA for the luminescent protein aequorin.* Proc Natl Acad Sci U S A, 1985. **82**(10): p. 3154-8.

124. Nomura, M., et al., *A C-terminal proline is required for bioluminescence of the Ca(2+)-binding photoprotein, aequorin.* FEBS Lett, 1991. **295**(1-3): p. 63-6.

125. Watkins, N.J. and A.K. Campbell, *Requirement of the C-terminal proline residue for stability of the Ca(2+)-activated photoprotein aequorin.* Biochem J, 1993. **293 (Pt 1)**: p. 181-5.

126. Brini, M., et al., *Transfected aequorin in the measurement of cytosolic Ca2+ concentration ([Ca2+]c). A critical evaluation.* J Biol Chem, 1995. **270**(17): p. 9896-903.

127. Rizzuto, R., et al., *Rapid changes of mitochondrial Ca2+ revealed by specifically targeted recombinant aequorin.* Nature, 1992. **358**(6384): p. 325-7.

128. Kendall, J.M., et al., *Engineering the CA(2+)-activated photoprotein aequorin with reduced affinity for calcium.* Biochem Biophys Res Commun, 1992. **187**(2): p. 1091-7.

129. Montero, M., et al., *Monitoring dynamic changes in free Ca2+ concentration in the endoplasmic reticulum of intact cells.* EMBO J, 1995. **14**(22): p. 5467-75.

130. Brini, M., et al., *Targeting of aequorin for calcium monitoring in intracellular compartments.* J Biolumin Chemilumin, 1994. **9**(3): p. 177-84.

131. Patergnani, S., et al., *Calcium signaling around Mitochondria Associated Membranes (MAMs).* Cell Commun Signal, 2011. **9**: p. 19.

132. Marchi, S., S. Patergnani, and P. Pinton, *The endoplasmic reticulum-mitochondria connection: one touch, multiple functions.* Biochim Biophys Acta, 2014. **1837**(4): p. 461-9.

133. Marchi, S., et al., *Mitochondrial and endoplasmic reticulum calcium homeostasis and cell death.* Cell Calcium, 2017.

134. Foskett, J.K., et al., *Inositol trisphosphate receptor Ca2+ release channels.* Physiol Rev, 2007. **87**(2): p. 593-658.

135. Berridge, M.J., *Inositol trisphosphate and calcium signalling.* Nature, 1993. **361**(6410): p. 315-25.

136. Supattapone, S., et al., *Solubilization, purification, and characterization of an inositol trisphosphate receptor.* J Biol Chem, 1988. **263**(3): p. 1530-4.

137. Hamada, K., et al., *Two-state conformational changes in inositol 1,4,5-trisphosphate receptor regulated by calcium.* J Biol Chem, 2002. **277**(24): p. 21115-8.

138. Nucifora, F.C., Jr., et al., *Molecular cloning of a cDNA for the human inositol 1,4,5-trisphosphate receptor type 1, and the identification of a third alternatively spliced variant.* Brain Res Mol Brain Res, 1995. **32**(2): p. 291-6.

139. Iwai, M., et al., *Molecular basis of the isoform-specific ligand-binding affinity of inositol 1,4,5-trisphosphate receptors.* J Biol Chem, 2007. **282**(17): p. 12755-64.

140. Mignery, G.A., et al., *Structure and expression of the rat inositol 1,4,5-trisphosphate receptor.* J Biol Chem, 1990. **265**(21): p. 12679-85.

141. Yoshikawa, F., et al., *Mutational analysis of the ligand binding site of the inositol 1,4,5-trisphosphate receptor.* J Biol Chem, 1996. **271**(30): p. 18277-84.

142. Chan, J., et al., *Structural studies of inositol 1,4,5-trisphosphate receptor: coupling ligand binding to channel gating.* J Biol Chem, 2010. **285**(46): p. 36092-9.

143. Michikawa, T., et al., *Transmembrane topology and sites of N-glycosylation of inositol 1,4,5-trisphosphate receptor.* J Biol Chem, 1994. **269**(12): p. 9184-9.

144. Ramos-Franco, J., et al., *Location of the permeation pathway in the recombinant type 1 inositol 1,4,5-trisphosphate receptor.* J Gen Physiol, 1999. **114**(2): p. 243-50.

145. Sayers, L.G., et al., *Intracellular targeting and homotetramer formation of a truncated inositol 1,4,5-trisphosphate receptor-green fluorescent protein chimera in Xenopus laevis oocytes: evidence for the involvement of the transmembrane spanning domain in endoplasmic reticulum targeting and homotetramer complex formation.* Biochem J, 1997. **323 (Pt 1)**: p. 273-80.

146. Mignery, G.A. and T.C. Sudhof, *The ligand binding site and transduction mechanism in the inositol-1,4,5-triphosphate receptor.* EMBO J, 1990. **9**(12): p. 3893-8.

147. Mignery, G.A., P.A. Johnston, and T.C. Sudhof, *Mechanism of Ca2+ inhibition of inositol 1,4,5-trisphosphate (InsP3) binding to the cerebellar InsP3 receptor.* J Biol Chem, 1992. **267**(11): p. 7450-5.

148. Suematsu, E., et al., *Inositol 1,4,5-trisphosphate releases Ca2+ from intracellular store sites in skinned single cells of porcine coronary artery.* Biochem Biophys Res Commun, 1984. **120**(2): p. 481-5.

149. Iino, M., *Biphasic Ca2+ dependence of inositol 1,4,5-trisphosphate-induced Ca release in smooth muscle cells of the guinea pig taenia caeci.* J Gen Physiol, 1990. **95**(6): p. 1103-22.

150. Bezprozvanny, I., J. Watras, and B.E. Ehrlich, *Bell-shaped calcium-response curves of Ins(1,4,5)P3- and calcium-gated channels from endoplasmic reticulum of cerebellum.* Nature, 1991. **351**(6329): p. 751-4.

151. Berridge, M.J. and R.F. Irvine, *Inositol trisphosphate, a novel second messenger in cellular signal transduction.* Nature, 1984. **312**(5992): p. 315-21.

152. Mak, D.O., S. McBride, and J.K. Foskett, *Inositol 1,4,5-trisphosphate [correction of tris-phosphate] activation of inositol trisphosphate [correction of tris-phosphate] receptor Ca2+ channel by ligand tuning of Ca2+ inhibition.* Proc Natl Acad Sci U S A, 1998. **95**(26): p. 15821-5.

153. Vanderheyden, V., et al., *Regulation of inositol 1,4,5-trisphosphate-induced Ca2+ release by reversible phosphorylation and dephosphorylation.* Biochim Biophys Acta, 2009. **1793**(6): p. 959-70.

154. DeSouza, N., et al., *Protein kinase A and two phosphatases are components of the inositol 1,4,5-trisphosphate receptor macromolecular signaling complex.* J Biol Chem, 2002. **277**(42): p. 39397-400.

155. Soulsby, M.D., et al., *The contribution of serine residues 1588 and 1755 to phosphorylation of the type I inositol 1,4,5-trisphosphate receptor by PKA and PKG.* FEBS Lett, 2004. **557**(1-3): p. 181-4.

156. Sienaert, I., et al., *Localization and function of a calmodulin-apocalmodulin-binding domain in the N-terminal part of the type 1 inositol 1,4,5-trisphosphate receptor.* Biochem J, 2002. **365**(Pt 1): p. 269-77.

157. Kang, S.S., et al., *Caffeine-mediated inhibition of calcium release channel inositol 1,4,5-trisphosphate receptor subtype 3 blocks glioblastoma invasion and extends survival.* Cancer Res, 2010. **70**(3): p. 1173-83.

158. Bansaghi, S., et al., *Isoform- and species-specific control of inositol 1,4,5-trisphosphate (IP3) receptors by reactive oxygen species.* J Biol Chem, 2014. **289**(12): p. 8170-81.

159. Lu, J.P., et al., *RNF170 protein, an endoplasmic reticulum membrane ubiquitin ligase, mediates inositol 1,4,5-trisphosphate receptor ubiquitination and degradation.* J Biol Chem, 2011. **286**(27): p. 24426-33.

160. Chen, J., et al., *The role of Src in colon cancer and its therapeutic implications.* Clin Colorectal Cancer, 2014. **13**(1): p. 5-13.

161. Mikoshiba, K., *The IP3 receptor/Ca2+ channel and its cellular function.* Biochem Soc Symp, 2007(74): p. 9-22.

162. Mendes, C.C., et al., *The type III inositol 1,4,5-trisphosphate receptor preferentially transmits apoptotic Ca2+ signals into mitochondria.* J Biol Chem, 2005. **280**(49): p. 40892-900.

163. Schreiner, S.J., A.P. Schiavone, and T.E. Smithgall, *Activation of STAT3 by the Src family kinase Hck requires a functional SH3 domain.* J Biol Chem, 2002. **277**(47): p. 45680-7.

164. Roderick, H.L. and S.J. Cook, *Ca2+ signalling checkpoints in cancer: remodelling Ca2+ for cancer cell proliferation and survival.* Nat Rev Cancer, 2008. **8**(5): p. 361-75.

165. Sigal, C.T., et al., *Amino-terminal basic residues of Src mediate membrane binding through electrostatic interaction with acidic phospholipids.* Proc Natl Acad Sci U S A, 1994. **91**(25): p. 12253-7.

166. Patwardhan, P. and M.D. Resh, *Myristoylation and membrane binding regulate c-Src stability and kinase activity.* Mol Cell Biol, 2010. **30**(17): p. 4094-107.

167. Courtneidge, S.A., A.D. Levinson, and J.M. Bishop, *The protein encoded by the transforming gene of avian sarcoma virus (pp60src) and a homologous protein in normal cells (pp60proto-src) are associated with the plasma membrane.* Proc Natl Acad Sci U S A, 1980. **77**(7): p. 3783-7.

168. Rizzuto, R., et al., *Close contacts with the endoplasmic reticulum as determinants of mitochondrial Ca2+ responses.* Science, 1998. **280**(5370): p. 1763-6.

169. Marchi, S., et al., *Oncogenic and oncosuppressive signal transduction at mitochondria-associated endoplasmic reticulum membranes.* Mol Cell Oncol, 2014. **1**(2): p. e956469.

170. Raturi, A. and T. Simmen, *Where the endoplasmic reticulum and the mitochondrion tie the knot: the mitochondria-associated membrane (MAM).* Biochim Biophys Acta, 2013. **1833**(1): p. 213-24.

171. Niklinska, B.B., et al., *Tyrosine kinase-regulated and inositol phosphate-independent Ca2+ elevation and mobilization in T cells.* J Biol Chem, 1992. **267**(10): p. 7154-9.

172. Jayaraman, T., et al., *Regulation of the inositol 1,4,5-trisphosphate receptor by tyrosine phosphorylation.* Science, 1996. **272**(5267): p. 1492-4.

173. Cui, J., et al., *Regulation of the type 1 inositol 1,4,5-trisphosphate receptor by phosphorylation at tyrosine 353.* J Biol Chem, 2004. **279**(16): p. 16311-6.

174. Harr, M.W., et al., *Glucocorticoid-mediated inhibition of Lck modulates the pattern of T cell receptor-induced calcium signals by down-regulating inositol 1,4,5-trisphosphate receptors.* J Biol Chem, 2009. **284**(46): p. 31860-71.

175. Jayaraman, T., et al., *The inositol 1,4,5-trisphosphate receptor is essential for T-cell receptor signaling.* Proc Natl Acad Sci U S A, 1995. **92**(13): p. 6007-11.

176. Olszowy, M.W., et al., *Comparison of p56lck and p59fyn protein expression in thymocyte subsets, peripheral T cells, NK cells, and lymphoid cell lines.* J Immunol, 1995. **155**(9): p. 4236-40.

177. Cooke, M.P., et al., *Regulation of T cell receptor signaling by a src family protein-tyrosine kinase (p59fyn).* Cell, 1991. **65**(2): p. 281-91.

178. Yokoyama, K., et al., *BANK regulates BCR-induced calcium mobilization by promoting tyrosine phosphorylation of IP(3) receptor.* EMBO J, 2002. **21**(1-2): p. 83-92.

179. Yuan, Z., et al., *Na/K-ATPase tethers phospholipase C and IP3 receptor into a calcium-regulatory complex.* Mol Biol Cell, 2005. **16**(9): p. 4034-45.

180. Wang, Q., et al., *Protein-tyrosine phosphatase-alpha and Src functionally link focal adhesions to the endoplasmic reticulum to mediate interleukin-1-induced Ca2+ signaling.* J Biol Chem, 2009. **284**(31): p. 20763-72.

181. Yaroslavskiy, B.B., et al., *Functional osteoclast attachment requires inositol-1,4,5-trisphosphate receptor-associated cGMP-dependent kinase substrate.* Lab Invest, 2010. **90**(10): p. 1533-42.

182. Colombo, S., et al., *N-myristoylation determines dual targeting of mammalian NADH-cytochrome b5 reductase to ER and mitochondrial outer membranes by a mechanism of kinetic partitioning.* J Cell Biol, 2005. **168**(5): p. 735-45.

183. Beauchamp, E., et al., *N-Myristoylation targets dihydroceramide Delta4-desaturase 1 to mitochondria: partial involvement in the apoptotic effect of myristic acid.* Biochimie, 2009. **91**(11-12): p. 1411-9.

184. Moriya, K., et al., *Protein N-myristoylation plays a critical role in the endoplasmic reticulum morphological change induced by overexpression of protein Lunapark, an integral membrane protein of the endoplasmic reticulum.* PLoS One, 2013. **8**(11): p. e78235.

185. Demetriadou, A., et al., *Mouse Stbd1 is N-myristoylated and affects ER-mitochondria association and mitochondrial morphology.* J Cell Sci, 2017. **130**(5): p. 903-915.

186. Pinton, P., et al., *Biosensors for the detection of calcium and pH.* Methods Cell Biol, 2007. **80**: p. 297-325.

187. Wieckowski, M.R., et al., *Isolation of mitochondria-associated membranes and mitochondria from animal tissues and cells.* Nat Protoc, 2009. **4**(11): p. 1582-90.